Looking at life through molecular vibrations

Biomedical applications of CARS spectro-microscopy

Looking at life through molecular vibrations

Biomedical applications of CARS spectro-microscopy

ACADEMISCH PROEFSCHRIFT

ter verkrijging van de graad van doctor
aan de Universiteit van Amsterdam
op gezag van de Rector Magnificus
prof. dr. D. C. van den Boom
ten overstaan van een door het college voor promoties
ingestelde commissie,
in het openbaar te verdedigen in de Agnietenkapel
op dinsdag 18 oktober 2012, te 14:00 uur

door

Gianluca Rago

geboren op 9 februari 1982
te Matera, Italië

Promotiecommissie

promotor:	prof. dr. M. Bonn
overige leden:	prof. dr. D. Bonn
	prof. dr. K.J. Hellingwerf
	prof. dr. A. Zumbusch
	dr. T. den Blaauwen
	dr. C. Otto
	dr. A. Volkmer

Faculteit der Natuurwetenschappen, Wiskunde en Informatica

ISBN 9789077209660

The work described in this thesis was performed at the FOM-*Institute for Atomic and Molecular Physics* (AMOLF), Science Park 104, 1098 SJ Amsterdam, The Netherlands. This work is part of the research programme of the *Stichting Fundamenteel Onderzoek der Materie* (FOM), which is financially supported by the *Nederlandse Organisatie voor Wetenschappelijk Onderzoek* (NWO).

Cover picture: Kwan Im Temple, Singapore

- Are you sure this is going to work?
- Nope...
(MacGyver)

Publications covered in this thesis

G. Rago, B. Bauer, F. Svedberg, L. Gunnarsson, M. B. Ericson, M. Bonn, and A. Enejder. Uptake of Gold Nanoparticles in Healthy and Tumor Cells Visualized by Nonlinear Optical Microscopy. *J. Phys. Chem. B 115(17)*, 5008 (2011).

J. P. R. Day, K. F. Domke, G. Rago, H. Kano, H. O. Hamaguchi, E. M. Vartiainen, and M. Bonn. Quantitative Coherent Anti-Stokes Raman Scattering (CARS) Microscopy. *J. Phys. Chem. B 115(24)*, 7713 (2011).

G. Rago, C. M. Langer, C. Brackman, J. P. R. Day, K. F. Domke, N. Raschzok, C. Schmidt, I. M. Sauer, A. Enejder, M. T. Mogl, and M. Bonn. CARS Microscopy for the Visualization of Micrometer-Sized Iron Oxide MRI Contrast Agents in Living Cells. *Biomed. Opt. Express 2(9)*, 2470 (2011).

G. Rago*, F. Marty*, G. Eijkel, K. Basler, E. Brunner, M. Bonn, and R. Heeren. Multimodal Hyper Spectral Label Free Molecular Imaging in Developmental Biology. *In preparation.*

G. Rago*, N. Billecke*, M. Bosma, S. Parekh, G. Eijkel, M. K. C. Hasselink and M. Bonn. CARS Imaging of Biological Components in Muscle Tissues. *In preparation.*

Other publications

M. H. F. Kox, K. F. Domke, J. P. R. Day, G. Rago, E. Stavirski, M. Bonn, and B. M. Weckhuysen. Label-Free Chemical Imaging of Catalytic Solids by Coherent Anti-Stokes Raman Scattering and Synchrotron-Based Infrared Microscopy. *Angew. Chem. 48(47)*, 8990 (2009).

M. Bonn, H. J. Bakker, G. Rago, F. Pouzy, J. R. Siekierzycka, A. M. Brouwer, and D. Bonn. Suppression of Proton Mobility by Hydrophobic Hydration. *J. Am. Chem. Soc. 131(47)*, 17070 (2009).

J. P. R. Day, G. Rago, K. F. Domke, K. P. Velikov, and M. Bonn. Label-Free Imaging of Lipophilic Bioactive Molecules during Lipid Digestion by Multiplex Coherent Anti-Stokes Raman Scattering Microspectroscopy. *J. Am. Chem. Soc. 132(24)*, 8433 (2010).

K. F. Domke, T. A. Riemer, G. Rago, A. N. Parvulescu, P. C. A. Bruijnincx, A. Enejder, B. M. Weckhuysen, and M. Bonn. Tracing Catalytic Conversion on Single Zeolite Crystals in 3D with Nonlinear Spectromicroscopy. *J. Am. Chem. Soc. 134(2)*, 1124 (2012).

K. F. Domke, J. P. R. Day, G. Rago, T. A. Riemer, M. H. F. Kox, B. M. Weckhuysen, and M. Bonn. Host-Guest Geometry in Pores of Zeolite ZSM-5 Spatially Resolved with Multiplex CARS Spectromicroscopy. *Angew. Chem. 51(6)*, 1343 (2012).

Contents

1 Introduction

1.1 Foreword: the light-matter interaction

Looking at, and seeing an object is, in more than one respect, determining the interaction between light and matter. An astronomer looking at planets and stars with his telescope is measuring the light that is emitted or reflected by the star or the planet, respectively. Similarly, when we take a picture or simply look at an object, we perform a complex measurement of the light that the object is reflecting, following absorption of specific components of the light spectrum that determine the colour of the object. Also when looking at the world of small objects, scientists use microscopes to measure the effect of a specific interaction between light and matter. The very word microscopy comes from the Greek words *mikrós*, that means "small", and *skopein*, "to look". Since the first microscopes appeared in Holland, Italy and England in the $17th$ century, the concept of microscopy has matured to embrace a variety of different approaches for looking at the world of small objects, but light microscopes still play a dominant role in the field.

Standard light microscopy techniques are based on the changes in amplitude or phase that are induced on the white light interacting with an object owing, primarily, to its local composition or density. While these differences originate from the variations in the spatial distribution of different molecules in a sample, the insight provided by most light microscopy techniques on the variations in sample composition are qualitative at best. Modern research in biological and material science on the other hand faces an increasing need for information that go beyond simple qualitative observation of a microscopic sample. The capability to selectively distinguish different chemical species and to determine their individual local concentrations are the key ingredients for new generation microscopy techniques allowing for quantitative measurements.

A number of quantitative approaches have been used as microscopic imaging techniques in biology [159], the primary alternative to white light microscopy being fluorescence microscopy. In confocal fluorescence microscopy the presence of a fluorescent dye molecule (fluorophore) can be identified with high spatial resolution. However, unless the sample is autofluorescent, this approach requires additional labels tagged to specific constituents of the sample. Hence, fluorescence microscopy generally requires the use of fluorescent labels. This is a potential drawback, as the introduction of fluorophores can affect the native behavior of the sample (see *e.g.* [151]). On the other hand, the use of these site-specific labels simplifies the visualization of complex systems, providing a response linearly dependent on the concentration for low concentrations [77].

Several microscopic imaging techniques allow instead to selectively distinguish the different compounds present in a sample by looking at molecular vibrations. All molecules inherently possess vibrations, and different functional groups vibrate at different, well-defined frequencies determined by effective masses and bond strengths. These two properties enable the use of molecular vibrations as intrinsic contrast agents for label-free, chemically specific, and potentially quantitative imaging methods.

1.2 VIBRATIONAL SPECTRO-MICROSCOPY

The history of microscopy techniques based on vibrational contrast dates back to the end of the 19th century when spectroscopy was developed along with quantum mechanics. Based on the revolutionary suggestion by Ludwig Boltzmann that the energy states of a physical system must be discrete, Max Planck postulated in 1900 the hypothesis that energy is radiated and absorbed in discrete amounts, *quanta*, as it was later confirmed by Einstein in his studies on the photoelectric effect. Nearly 25 years later Schroedinger derived the famous equation describing the time evolution of the quantum state of a system. Based on this equation the energies of the quantized vibrational states of molecules could be derived analytically, in fact providing the theoretical explanation to the pioneering work on vibrational spectroscopy performed at Cornell University. Here, in 1903, William Coblentz started to collect the spectra of infrared (IR) light absorbed by inorganic and organic substances [36]. The results of his work led to the belief that certain functional groups of molecules absorb only specific IR wavelengths. Over the following years it was shown how the chemical bonds of each functional group of a molecule are characterized by a set of vibrations of well-defined energies in the range between 400 and 4000 cm^{-1}, *i.e.* part of the IR region of the spectrum. These vibrational states could be studied indirectly through their interactions with light, providing a fingerprint of the molecule related both to the strength of its chemical bonds, the masses of the atoms involved and their geometric conformation.

The most important techniques of vibrational spectroscopy are IR absorption and Raman scattering, both involving the study of the interaction of electromagnetic radiation with matter, although differing in the mechanism of energy transfer between photons and molecules that leads to a transition between vibrational states. In IR spectroscopy the energy of the radiation matches the difference of the energy of two vibrational states, hence the incident photon is absorbed in the process while the resonant transition between the two energetic levels is promoted. Raman spectroscopy relies instead on a two-photon inelastic scattering event generated by radiation with much greater energy than the transition energy. In the scattering process the incoming photon exchanges energy with the molecule in an off-resonance condition mediated by the polarizability of the system. The measured vibrational bands are characterized for both techniques by their central frequency, intensity and band shape which are directly related to the energy, polar character or polarizability and environment of the

bonds respectively. Hence, both IR and Raman spectra contain specific and potentially quantitative information on the structure of the molecules and their environment. Based on these features the two techniques have the potential to be label-free quantitative microscopy tools. Incidentally, due to the long wavelength required for the experiments, the spatial resolution of IR microscopy is limited to 2.5 - 25 μm. Although commercial IR microscopes have been available for several decades, their use in life science has been limited to a handful of research topics where the resolution would not play a central role [134].

Spontaneous Raman spectro-microscopy circumvents some of the limitations of IR microscopy as visible or near-IR light is employed as the excitation source. Consequently, the lateral and depth resolutions are considerably better than those in IR microscopy, and may go down to 250 nm and 1 μm, respectively, for a confocal instrument. As mentioned in the previous paragraph, the inelastic scattering of light by molecules is at the base of the Raman effect discovered in 1928 [174]. The energy level diagrams of spontaneous Raman are depicted in Fig. 1.1. When a photon from the incident beam with frequency ω_1 interacts with the molecule, it induces a transition to a virtual state. From there three radiative relaxation pathways are possible, differing in the frequency of the emitted photon. The first and most common event is elastic or Rayleigh scattering (A) arising from a transition that starts and finishes at the same vibrational energy level, associated with an emitted photon of frequency $\omega_2 = \omega_1$. Alternatively and with lower probability of occurrence, inelastic scattering can take place, resulting in a shift to lower or higher frequency of the emitted photon. Stokes Raman photons (B) arise from a transition that starts at the ground vibrational state and finishes at an excited vibrational state characterized by frequency ω_ν. As a result the emitted photon is red-shifted to the frequency of $\omega_2 = \omega_1 - \omega_\nu$. Anti-Stokes Raman (C) arises instead from a transition from an excited vibrational state to the ground state. In this case the frequency of the emitted photon is blue-shifted to $\omega_2 = \omega_1 + \omega_\nu$. According to Boltzmann statistics regulating the distribution of the population of the energy states, most molecular vibrations are in their ground state at room temperature [112], effectively reducing the probability of occurrence of anti-Stokes scattering events. Also the Stokes Raman scattering is relatively improbable: typically only $\sim 10^{-7}$ of the incident photons are inelastically scattered.

The Raman scattering cross section of water is relatively low compared to organic molecules, which means that the technique is readily applicable to investigate biological matter. In fact Raman spectro-microscopy, *micro-Raman*, was first used in 1990 by Puppels *et al.* to study single cells, combining spontaneous Raman spectroscopy with confocal microscopy [169]. Micro-Raman has largely developed in the last two decades, and is regarded as the best vibrational spectroscopy-based technique for bioimaging, although the relatively long measurement times are still an obstacle for its application to cell dynamics research. Furthermore, in some cases the spontaneous Raman signal suffers from contamination from single-photon fluorescence.

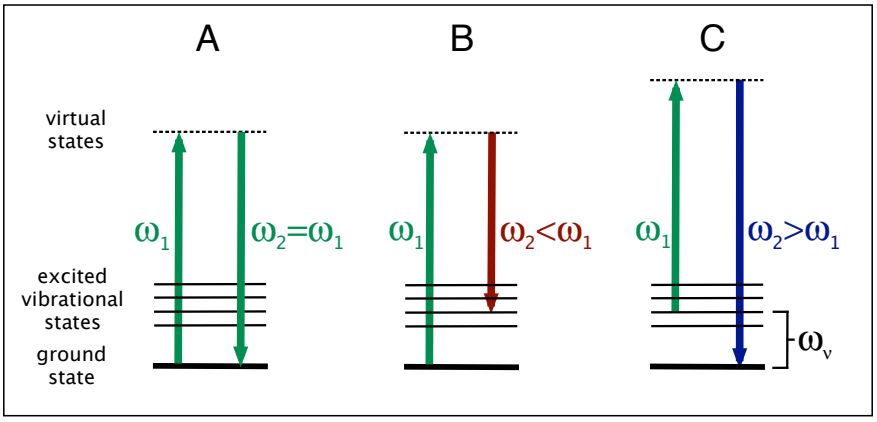

FIGURE 1.1. Molecular energy level diagram of the different scattering processes taking place when light interacts with a molecule. ω_1 and ω_1 represent the frequencies of the incoming and generated beams respectively. ω_ν is the frequency associate with the vibrational state with energy $h\omega_\nu$. (A) Rayleigh scattering, (B) Stokes Raman scattering, and (C) anti-Stokes Raman scattering.

1.3 Coherent anti-Stokes Raman Scattering

Coherent Raman techniques have been developed to circumvent the limitations of spontaneous Raman scattering, among which the Coherent anti-Stokes Raman Scattering (CARS). These techniques only begun developing in the second half of the 20th century thanks to the invention of lasers, light sources powerful enough to induce multi-photon processes. CARS was first observed in 1965 by Maker and Terhune at the scientific laboratories of Ford Motor Company [131], and it took almost thirty years before Duncan developed the first CARS microscope in 1982 [59]. The real breakthrough of the technique as a microscopy tool however arrived with the research of the Xie group at Harvard University [216], followed by several results including epi-detection geometry [205], polarization sensitive detection [26], and video-rate imaging [66].

CARS is a third order non-linear process involving the interaction of four photons with the sample. As shown in Fig. 1.2 (A), a pump photon of frequency ω_{pu}, a Stokes photon of frequency ω_S and a probe photon of frequency ω_{pr} interact with a molecule and generate an anti-Stokes photon of frequency $\omega_{AS} = \omega_{pu} - \omega_S + \omega_{pr}$. Most experiments actually use a degenerate configuration with the pump and the probe photon at the same frequency, so that the previous relationship for the frequency of the anti-Stokes photon is simplified to $\omega_{AS} = 2\omega_{pu} - \omega_S$. When the difference $\omega_{pu} - \omega_S$ matches the frequency of a vibrational resonance ω_ν of the molecule, the anti-Stokes process is resonantly enhanced. It is instructive to consider the CARS process as divided in two steps. The effect of the combined action of the pump and Stokes photons is to resonantly drive a molecular vibration, creating a polarization between the ground and

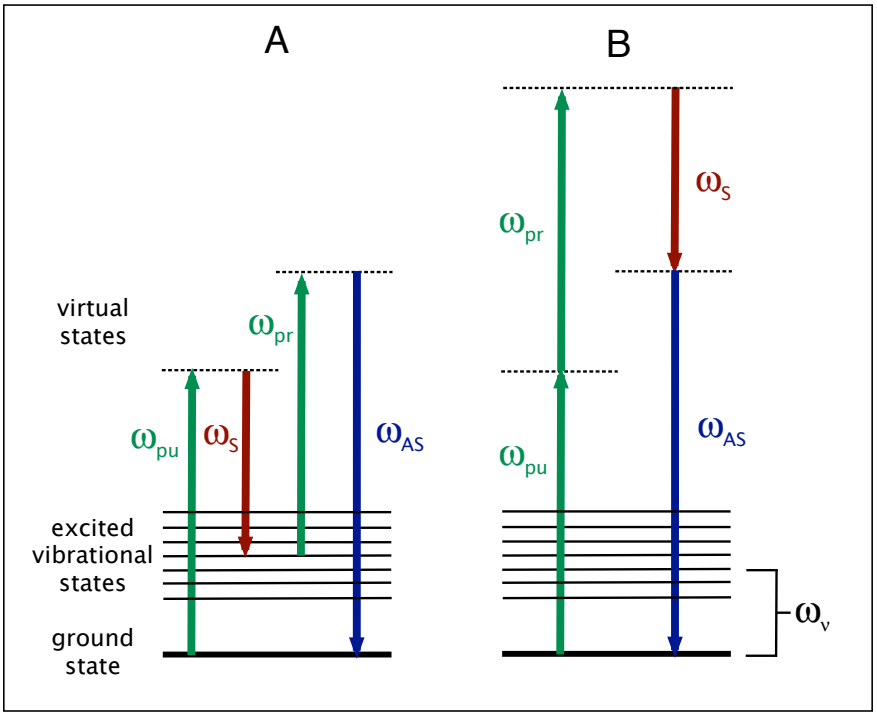

FIGURE 1.2. CARS energy level diagrams: (A) vibrationally resonant interaction, and (B) non-resonant electronic interaction. ω_{pu}, ω_S, ω_{pr}, and ω_{AS} represent the frequencies of the pump, Stokes, probe and anti-Stokes beams respectively, and ω_ν is the frequency associate with the vibrational state with energy $h\omega_\nu$. For the schemes shown here, $\omega_{pu} = \omega_{pr}$.

excited vibrational states. In the second part of the process, the probe photon upconverts the polarization to a virtual level, from where the system relaxes to the ground state while emitting the anti-Stokes photon.

The transitions involved in the CARS process are not spontaneous but driven by the incoming photons, causing the phase scattered light to be determined by that of the driving fields, *i.e.* the process is coherent and the phase of the CARS light must match that of the driving fields. An important consequence of the phase matching is the highly directional emission of the CARS signal, as constructive interference between the CARS-radiating dipoles is only achieved in a specific direction while destructive interference is observed in all the other directions. CARS response is over five orders of magnitude stronger relative to spontaneous Raman scattering, and the technique is not affected by the one-photon fluorescence background that was previously mentioned to affect the quality of the response of conventional Raman.

The key to the success of CARS as a microscopy tool relies in the use of

collinear excitation geometries, with the beams focused on the sample by a high numerical aperture microscope objective. In this configuration the phase matching conditions are intrinsically fulfilled, and the nonlinear interaction is confined to the tiny volume at the focus of the beams. This provides CARS microscopes with intrinsic sub-micron three dimensional resolution. Together with the chemical specificity and the linear dependency of the response on the concentration of chemical species, this prompts CARS as the ideal tool for label-free high resolution imaging of biological systems. Unfortunately, the concentration information is generally not immediately accessible from the raw CARS signal, which has limited the extent to which CARS microscopy has been used as a fully quantitative imaging technique. The major drawback of CARS compared to spontaneous Raman scattering is the presence of a non-resonant background signal of electronic origin. The non-resonant background arises from four wave mixing processes that do not involve any of the vibrational energy levels of the molecule, such as the one exemplified in the energy diagram of Fig. 1.2 (B). Far from electronic resonances, the non-resonant response is strictly real and frequency-invariant, and it depends solely upon the electronic properties of the material. The importance of the non-resonant background will be discussed in details in the next chapter, as well as possible approaches for retrieving the quantitative information of the CARS signal.

Over the years two complementary approaches to CARS microscopy have been developed, single frequency CARS and multiplex CARS (also referred to as broadband CARS). In single frequency CARS an individual vibrational resonance (such as the methylene symmetric stretching mode of lipids at ~ 2845 cm^{-1}) is addressed, and the CARS response at that frequency is imaged across the sample. Often, this vibrational contrast alone is sufficient to report on, for example, lipid storage and metabolism within a living cell [98] or the morphology of biological tissue for cancer screening [67]. Single frequency CARS is most suitable when images are sought that exhibit qualitative contrast based on vibrational differences in the sample, but the lack of spectral information limits its applicability as a quantitative imaging technique. In multiplex CARS a broad range of vibrational resonances are simultaneously addressed. Imaging is accordingly slower than single frequency CARS, but in return richer spectral information is acquired at each location within the sample, making the extraction of quantitative information considerably simpler than that for single frequency CARS microscopy.

Multiplex CARS microscopy is comparable to spontaneous Raman microscopy; in both techniques, a vibrational spectrum is acquired at each location in the image (hyperspectral imaging). As already mentioned, the nonlinear and coherent nature of CARS results in a signal enhancement of several orders of magnitude compared to that of Raman. It should also be noted that the CARS signal depends on the incident laser intensity in a nonlinear fashion, whereas in spontaneous Raman, a simple linear scaling applies. Hence, for samples that are susceptible to photodamage, micro-Raman may in some cases be more appropriate [43].

1.4 CARS AND BIOLOGY

Although most of the initial research performed with CARS dealt with combustion diagnostics, the drive for the development of CARS microscopy has mostly been the investigation of biological problems. Here, the potential of CARS imaging is expressed at its best. Physiological conditions are maintained in the experiments as exogenous labels are not added to the system, and multiple biological components can be monitored based solely on their chemical composition.

Most of the applications of CARS microscopy in life science of the last twenty years have been performed using the single frequency approach of the technique. The first example of biological application of CARS used the broad vibration of water centered at 3300 cm^{-1} to monitor its diffusion in live *Dictyostelium* cells [163]. Subsequently, researchers focused their attention on the symmetric stretch of CH_2 groups at 2845 cm^{-1}, due to the abundance of this molecular moiety in lipids. When monitoring this vibration, sufficient image contrast can be generated by variations in concentration of less than 10^6 CH_2 oscillators in the focal volume. This figure corresponds to roughly 10^5 lipid molecules, or alternatively sub-millimolar concentrations [123]. Such high sensitivity allows CARS microscopy to image even single phospholipid bilayers [165], impossible to detect with spontaneous Raman.

It is then not surprising that CARS microscopy has become a leading instrument for studying lipid biology in cells and tissues. Lipids are the major component of cell membranes [197], but they are also involved in several biological problems and the misfunctioning of their metabolic processes can lead to many debilitating diseases including diabetes and atherosclerosis [51]. It is in fact believed that lipid droplets (LDs) have a role that goes beyond the simple storing of fatty acids, and are actively involved in several biological processes [68]. Experimentally, the cellular processes involving lipid droplets can be monitored with CARS over extended periods with high frame rates, thanks to the absence of photobleaching. This allows for example to follow LDs dynamics in live cells [149], as well as to study the processes underlying LD formation [148]. Some of these applications of CARS to study lipids in cells are reviewed in [119].

A natural extension of cellular studies was the application of CARS to investigate lipids in *C. elegans* [98], as they are optically transparent and their metabolic pathways are comparable to those of humans [109]. One step further is the use of CARS to study tissues. Here the experimental conditions suffer from the non-trivial complication of the significant amount of light scattering as a consequence of the large variations of the refractive index in the different components of the tissue, and the absorption of light simply due to the thickness of the sample. Thanks to the implementation of smart focusing and detection approaches, excellent results have come from CARS studies of tissues, *e.g.* as reported in a recent review by Potma [166].

CARS biological studies largely benefit from the implementation of other nonlinear optical techniques on the same experimental platform. The pulsed

lasers used for CARS experiments simultaneously induce other effects such as 2-Photon Fluorescence (2PF), Second Harmonic Generation (SHG) and Third Harmonic Generation (THG). Hence, all these signals can be monitored simultaneously when additional detectors coupled with the appropriate spectral filters are included in the CARS setup. 2PF can be for example used for simultaneous visualization of fluorescently labeled proteins, whereas SHG can monitor collagen and other non-centrosymmetric molecular structures, while CARS continues to serve its main function of lipid monitoring. Several examples of the combination of CARS with other such techniques can be found in literature [15, 16, 75, 163]. Similarly, single frequency CARS can be combined with spontaneous Raman. The former providing fast imaging capabilities of an individual vibration, and the latter measuring the complete spectrum at a limited number of pixels of interest [190].

The aforementioned examples of CARS in biology have all been single-line implementations of CARS microscopy. Multiplex CARS has also been successfully used in biology. Compared to single frequency CARS, the amount of information contained in the hyperspectral images of multiplex CARS is considerably richer as multiple vibrations are addressed simultaneously. The longer acquisition times and the complexity of data interpretation have slowed down the diffusion of this approach. Nonetheless, multiplex CARS has provided important understanding of chemical features of biological processes otherwise impossible to access with other approaches. Initially, the Muller group was able study lipid aggregations in adipocytes determining the inhomogeneities in lipid composition within individual LDs [179]. More recently, the Hamaguchi group was able to distinguish individual cellular components based only on their vibrational signatures in the fingerprint region of the spectrum [152].

A complete overview of the applications of CARS microscopy present in literature goes beyond the aim of this thesis. The short overview presented in this paragraph is meant to give an insight of the large potential of the technique to help solving a variety of biological problems.

1.5 Thesis overview

This thesis covers the application of both single-line and multiplex approaches of CARS microscopy to selected biomedical problems. The results presented highlight the potential of vibrational microscopy as a quantitative analysis tool for life science research, capable to provide high resolution biological images without the requirement of exogenous labels.

- **Chapter 2** presents the theoretical aspects of the work discussed in this thesis. The theoretical foundation of the technique is outlined, starting from the derivation of the analytic form of the CARS response and the derivation of the imaginary part of the molecular susceptibility with the Maximum Entropy Method. The last part of the chapter deals with the basics of multivariate analysis methods such as Principal Component Analysis, used for data treatment.

- **Chapter 3** presents the experimental aspects of this research work. Here, the single frequency and broadband CARS setups used for the experiments are described.

- **Chapter 4** presents the single frequency CARS experiments aimed to monitor the efficient internalization of MRI contrast agents (micrometer-sized iron-oxide particles) in living cells.

- **Chapter 5** presents a study on the intracellular uptake of functionalized nanoparticles in healthy and tumor cells. The particles are visualized *in vivo* using the combination of single frequency CARS and Multi-photon Induced Luminescence.

- **Chapter 6** presents the investigation of the imaginal wing disc of *drosophila melanogaster* with broadband CARS. The aim of the study is to understand the local chemical differences underlying the appearance and maintenance of cell compartments during embryogenesis.

- **Chapter 7** presents the visualization of biological components (lipid droplets and mitochondria) in muscle tissues based on their chemical signatures. This information is retrieved by applying multivariate analysis methods to the broadband CARS hyperspectral images.

2 Theory

In this chapter the CARS response is derived analytically, and the properties that make the technique suitable as a quantitative microscopy imaging technique are described. At the end of the chapter, the basics of a multivariate analysis method for data treatment, Principal Components Analysis, are also presented.

2.1 CARS theory

When light interacts with matter, the electrons surrounding the nuclei respond by oscillating at the same frequency as the incoming field[a]. The field, in other words, induces a polarization in the sample. For relatively weak incident light fields, the induced displacement of the electrons is small and the induced polarization of the electrons is linearly proportional to the incoming field. The proportionality factor (determined by the properties of the sample) is the susceptibility χ. This simple proportionality may break down for stronger electric fields such as the ones produced by the pulsed laser beams used in CARS setups. In this case, the displacement of the electronic cloud caused by the interaction is no longer linear and higher order terms are necessary to describe the interaction.

Expressing the electromagnetic wave as a vector $\overrightarrow{E}$ with amplitude E, the general expression of the response of an optical material is described by the expansion of the induced polarization as a power series in the electric field strength:

$$\overrightarrow{P} = \chi^{(1)}\overrightarrow{E} + \chi^{(2)}\overrightarrow{E}\overrightarrow{E} + \chi^{(3)}\overrightarrow{E}\overrightarrow{E}\overrightarrow{E} + \dots \tag{2.1}$$

where the expansion coefficients $\chi^{(n)}$ are known as n-th order susceptibilities. Higher order susceptibilities are expected to grow progressively smaller so that the power series expansion converges to a finite polarization. The susceptibilities are expressed by tensors, relating the different field directions and frequencies to the direction and strengths of the induced polarization. In the regime of low intensity fields, only the first order term is important and is the basis for classical linear optics including normal Raman scattering. In the presence of an intense field, higher order terms are required to correctly describe the polarization in the medium. The magnitude of the third-order nonlinear susceptibility shown in the previous equation is a measure of the conversion efficiency of the specific

[a] The light sources used in CARS experiments have frequencies in the optical range between $10^{13} - 10^{17}$ Hz. Such frequencies are too high for the nuclei in the molecules to respond to the oscillations, hence the response of the material arises only from the induced oscillations of the electrons.

process involving the interaction of three incoming photons, *e.g.* in the CARS process the signal is emitted at the anti-Stokes frequency, $\omega_{AS} = 2\omega_{pu} - \omega_S$ [10]. The third order susceptibility $\chi^{(3)}$ involved in the CARS process is the sum of a frequency dependent resonant part, and a nearly frequency-independent non-resonant part:

$$\chi^{(3)}(\omega_{AS}) = \chi_R^{(3)} + \chi_{NR}^{(3)} \tag{2.2}$$

The resonant part $\chi_R^{(3)}$ contains the quantitative and chemically specific information about the sample in focus, as it reports on the spectral properties of spontaneous Raman vibrational resonances, as discussed below.

The magnitude of $\chi_R^{(3)}$, and hence the efficiency of the photon energy conversion of the CARS process, increases rapidly when the frequency difference between the pump and the Stokes beams is resonant with a vibrational transition ω_ν of a chemical moiety in the sample, *i.e.* when $\omega_{pu} - \omega_S = \omega_\nu$. Close to a Raman-active resonance, the resonant part of the susceptibility is given by [47]:

$$\chi_R^{(3)} = \frac{A_j}{\omega_\nu - (\omega_{pu} - \omega_S) - \imath\Gamma_j} \tag{2.3}$$

where A_j and Γ_j are the amplitude and line width of the j-th vibrational mode of frequency ω_ν. The detailed derivation, following the approach used by Boyd [14], of the analytic form of $\chi_R^{(3)}$ is reported in the Appendix in Paragraph 2.4.

By comparing the form of $\chi_R^{(3)}$ in Eq. (2.3) with the spontaneous Raman scattering line shape for a single vibration

$$I_{Raman}(\omega) \propto \frac{A_j\Gamma_j}{(\omega_\nu - \omega)^2 + \Gamma_j^2} \tag{2.4}$$

it is immediately evident that the line shape of Raman peaks can be obtained from the imaginary part of the third order molecular susceptibility

$$\mathrm{Im}(\chi_R^{(3)}) = \frac{A_j\Gamma_j}{(\omega_\nu - (\omega_{pu} - \omega_S))^2 + \Gamma_j^2} \tag{2.5}$$

Crucially, $\mathrm{Im}(\chi_R^{(3)})$ is chemically specific and depends linearly upon concentration [178] (cfr. Eq. (2.38) in appendix). Unfortunately, this information is not readily available from the data directly obtained in a CARS measurement as the detected signal, I_{AS}, depends on both the resonant and nonresonant terms of the susceptibility, according to

$$I_{AS} \propto |\chi^{(3)}|^2 = |\chi_R^{(3)} + \chi_{NR}^{(3)}|^2 = |\chi_R^{(3)}|^2 + 2\chi_{NR}^{(3)} Re\left[\chi_R^{(3)}\right] + |\chi_{NR}^{(3)}|^2 \tag{2.6}$$

The resonant and nonresonant term interfere via the middle of the three terms of Eq. (2.6), and the resonant term can therefore not be retrieved by a simple background correction. Due to this interference the quantitative data contained within $\chi_R^{(3)}$ is not directly accessible; the presence of the nonresonant

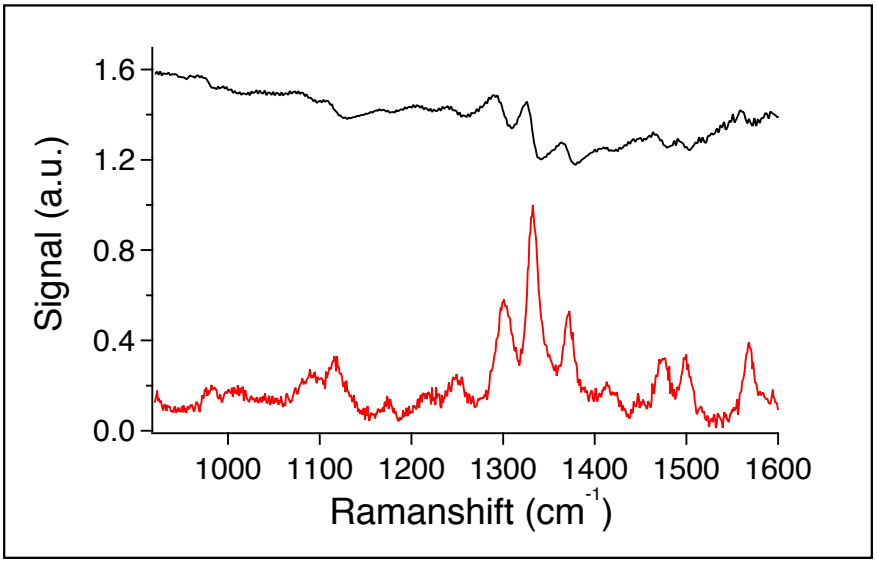

FIGURE 2.1. Comparison of (red) spontaneous Raman and (black) multiplex CARS spectra of an equimolar mixture of AMP/ADP/ATP in water at a total concentration of 500 mM. Total acquisition time for Raman and CARS data is 3 min and 800 ms respectively. Reproduced from reference [202].

contribution$\chi^{(3)}_{NR}$ to the overall susceptibility means that there is no simple, linear correlation between I_{AS} and concentration. This complexity is illustrated in Fig. 2.2, which shows the comparison of the spontaneous Raman and multiplex CARS spectra of the same sample, an equimolar mixture of AMP/ADP/ATP in aqueous solution at a total concentration of 500 mM [202]. The interference between the resonant and nonresonant terms results in dispersive, Fano-type lineshapes in the CARS spectrum in comparison to the Lorentzian-type lineshapes in the spontaneous Raman spectrum. Fig. 2.2 also highlights why, despite the additional complexity of its spectral response, CARS is sometime preferable to spontaneous Raman owing to its far higher response; in fact, the spectra in figure were acquired in 800 ms and 3 min for CARS and Raman respectively.

In order to extract the quantitative information from the anti-Stokes CARS intensity I_{AS} we have to be reminded of the comparison of Eq. (2.4) and Eq. (2.6), showing that the quantitative linearly dependent information is contained in the imaginary part of the susceptibility. The obvious implication is that, if we are able to extract $\mathrm{Im}(\chi^{(3)}_R)$ from I_{AS} we can eliminate the complicating influence of the nonresonant term, allowing CARS to be used as a quantitative microscopic imaging technique. In fact, additional benefits are obtained by retrieving the $\mathrm{Im}(\chi^{(3)}_R)$ response. As the $\mathrm{Im}(\chi^{(3)}_R)$ spectrum is directly comparable to the spontaneous Raman response of the material, reference can be made to correlation charts of known Raman bands. Second, it is eas-

ier to identify overlapping Lorentzian peaks in an $\mathrm{Im}(\chi_R^{(3)})$ spectrum than the overlapping Fano-type resonances occurring in an I_{AS} spectrum. Finally, linear analysis techniques and multivariate analysis methods can be used to aid spectral deconvolution for complex samples.

Several approaches have been developed to extract quantitative results from CARS data and to deal with the influence of the nonresonant response. A number of these methods aims to separate the resonant from the nonresonant contribution to the CARS intensity in order to access the imaginary part of the susceptibility. This separation can be done with experimental methods using intensity calibration [7, 215], limiting cases of strong or weak resonant scatterers [97, 123], and time gating [204], or with mathematical methods such as peak fitting procedures [177, 206]. Alternatively, we can note that the nonresonant response $\chi_{NR}^{(3)}$ is instantaneous and therefore purely real. Hence, in order to retrieve $\mathrm{Im}(\chi_R^{(3)})$ it is sufficient to extract the phase of the CARS field, θ, according to

$$\mathrm{Im}(\chi_R^{(3)}) = |\chi^{(3)}| \; sin \; \theta \propto \sqrt{I_{AS}} \; sin \; \theta \tag{2.7}$$

Using the nonresonant background rather than suppressing it, actually turns out to be an advantage when measuring the CARS signal relative to it. The heterodyne amplification of the resonant contribution through the nonresonant background in fact increases the sensitivity of the measurement [146].

2.2 Maximum Entropy Method

Eq. (2.7) states that the analytic form of $\mathrm{Im}(\chi_R^{(3)})$ can be obtained from the CARS signal intensity if the vibrational phase of the signal is known. Physically, the vibrational phase is the phase difference between the driving field, described by the superposition of the pump and the Stokes fields, and the induced motion of the dipoles in the sample. The nonresonant response has zero phase owing to its instantaneous nature, making the response real and positive. Instead, the resonant response has a nonzero vibrational phase whose magnitude will vary depending on the detuning frequency, $\omega_\nu - (\omega_{pu} - \omega_S)$, and the concentration of the sample. Very dilute samples ($\chi_R^{(3)} \ll \chi_{NR}^{(3)}$) will have a vibrational phase close to 0, whereas for highly concentrated samples, the phase shift can reach the limiting values of $\pm(\pi/2)$ radians.

The vibrational phase can be measured experimentally with interferometric approaches [35, 107, 108, 164], or extracted mathematically from the CARS signal intensity. The mathematical phase retrieval represents a classical problem of how to recover the phase of a complex function from its modulus. Although in the most general case there are an infinite number of solutions to the phase retrieval problem, in practical situations, there are constrains on the form of the solution [140]. These constraints reduce drastically the number of allowed solutions and, in the case of CARS spectra, typically result in a very good approximation of the real vibrational phase. Two well established

approaches to mathematical phase retrieval of CARS spectra are the time domain Kramers-Kronig (TD-KK) transform and the maximum entropy method (MEM). It should be noted that there is little difference in the effectiveness of each of the two phase retrieval methods and both of them allow for quantitative analysis of CARS data, as demonstrated *e.g.* in their comparison presented in reference [47]. In this thesis, the MEM approach was used to retrieve the phase of the CARS signal. The theory underlying the TD-KK approach can be found in literature [128], as well as examples of its applications [156, 192].

The MEM is based on concepts from information theory where the entropy, there also called Shannon entropy, measures the uncertainty associated with a random variable. C.E. Shannon stated that any additional knowledge to be gained relative to an incomplete information, or set of data, must be based on the probability distribution with the maximum entropy allowed by the constraint of the available information itself [184]. This is the typical condition we face when trying to extract the phase from the power spectrum, as the phase is defined as a function of the frequency in the spectral interval between 0 and ∞, to be derived from the power spectrum that is experimentally measured in a limited spectral interval, $[\omega_i, \omega_f]$. We describe here the MEM based on the method originally developed by Burg[b]. Consider the function $S(\omega_{AS})$ representing the CARS spectrum as obtained in a CARS experiment where the signal from the sample is divided by the signal from a reference sample containing no vibrational resonances in the measured frequency range. Using the normalized frequency, $\nu = (\omega_{AS} - \omega_i)/(\omega_f - \omega_i)$, we define $S(\nu)$ to restrict the calculations to the $[0, 1]$ dimensionless interval. $S(\nu)$ contains M data points and is directly proportional to the squared modulus of the susceptibility. $S(\nu)$ can be written as the Fourier transform of its autocorrelation functions $C(m)$:

$$S(\nu) = \sum_{m=-\infty}^{\infty} C(m) \exp(-i2\pi m\nu) \tag{2.8}$$

$$C(m) = \int_0^1 S(\nu) \exp(i2\pi m\nu) d\nu \tag{2.9}$$

Incidentally, as the power spectrum is measured in a limited interval, only the first $2M + 1$ autocorrelations are known[c], for $|m| \leq M$. Opposed to the conventional method for the determination of the power spectrum from a limited number of autocorrelations, where the value $C(m) = 0$ is assumed for $|m| \geq M$, in the MEM the missing autocorrelation functions are obtained by maximizing the entropy rate of the power spectrum defined as [201]:

$$h \propto \int_0^1 \log S(\nu) d\nu \tag{2.10}$$

Hence, the required ME power spectrum is the function $\widehat{S}(\nu)$, solution to the

[b] A complete treatment of the MEM theory can be found in references [200, 201]

[c] From Eq. (2.9), $C(-m) = C^*(m)$. Hence when $C(m)$ is known, $C(-m)$ is also known.

equation

$$\frac{\partial}{\partial C(m)} = \int_0^1 \log S(\nu) d\nu = 0, \ |m| \geq M \tag{2.11}$$

The MEM model for CARS power spectra is expressed as [96]:

$$\widehat{S}(\nu) = \frac{|\beta|^2}{|1 + \sum_{k=1}^{M} a_k \exp(-i2\pi k\nu)|^2} = \frac{|\beta|^2}{|A_M(\nu)|^2} \tag{2.12}$$

where the coefficients a_k and $|\beta|$ can be calculated from a set of linear Yule-Walker equations:

$$\begin{bmatrix} C_0 & C_1^* & \cdots & C_M^* \\ C_1 & C_0 & \cdots & C_{M-1}^* \\ \vdots & \vdots & \ddots & \vdots \\ C_M & C_{M-1} & \cdots & C_0 \end{bmatrix} \begin{bmatrix} 1 \\ a_1 \\ \vdots \\ a_M \end{bmatrix} = \begin{bmatrix} |\beta|^2 \\ 0 \\ \vdots \\ 0 \end{bmatrix} \tag{2.13}$$

$A_M(\nu)$ is a complex function whose argument $\psi = \arg\{A_M(\nu)\}$ takes the name of ME phase function. Introducing an error phase $\varphi(\nu) = \theta(\nu) - \psi(\nu)$, we can use Eq. (2.12) to retrieve the true phase of the susceptibility[d] [202]:

$$\chi_{nr} + \chi_r(\nu) = \sqrt{\widehat{S}(\nu)} \exp(i\theta(\nu)) \cong \frac{|\beta| \exp(i\theta(\nu))}{|A_M(\nu)|} = \frac{|\beta| \exp(i\theta(\nu) - i\psi(\nu))}{|A_M(\nu)| \exp(i\psi(\nu))} = \frac{|\beta| \exp(i\varphi(\nu))}{A_M^*(\nu)} \tag{2.14}$$

The retrieval of the phase is then reduced in the MEM to perform a background correction of the function $\psi(\nu)$. The ME phase in fact presents the same spectral features as the true phase $\theta(\nu)$, superimposed to a slowly varying background expressed by $\varphi(\nu)$. Using the constraint that $\theta(\nu) \approx 0$ far from vibrational resonances, MEM allows to estimate the true phase function allowing to retrieve the Raman-like spectrum hidden in the CARS data.

The MEM phase retrieval is exemplified in Fig. 2.2 for the CARS data obtained from the equimolar mixture of AMP/ADP/ATP. In panel (A) the calculated MEM phase $\psi(\nu)$ (solid line) containing the spectral features is presented together with the slowly varying background representing $\varphi(\nu)$ (dashed line). From the comparison in panel (B) of the retrieved $\mathrm{Im}(\chi_R^{(3)})$ (black line) and the corresponding Raman spectrum (red line) of the same solution it is clear that the MEM is capable of retrieving the exact same spectral features that define quantitatively the composition of the sample.

2.3 Principal Component Analysis

Retrieving the vibrational peaks from the raw data is unfortunately only the first challenge in data analysis of CARS images. In fact, when performing a spectro-microscopy CARS measurement one obtains a hyperspectral dataset as

[d] In typical CARS experiments, the resonant and non resonant terms are expressed in their normalized form as $\chi_{nr} = \chi^3_{NR}/\chi^3_{NR,ref}$ and $\chi_r(\nu) = \chi^3_R(\nu)/\chi^3_{NR,ref}$ respectively. The reference sample presents no vibrational resonances in the measured frequency interval.

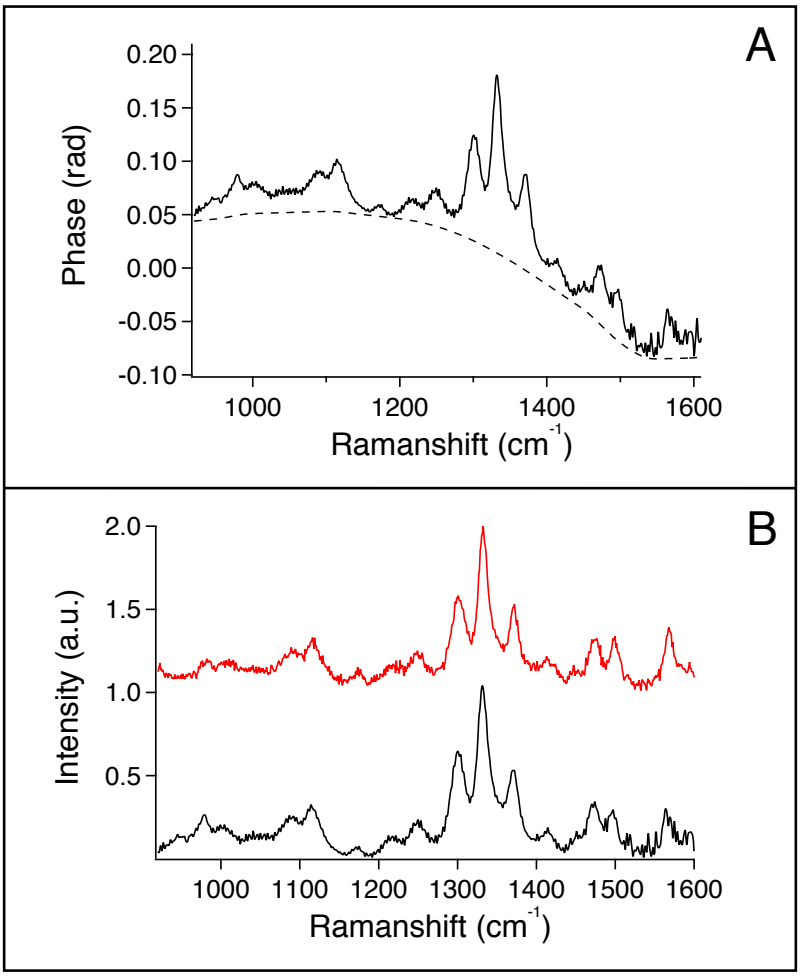

FIGURE 2.2. (A) Phase (solid line) retrieved with MEM from the multiplex CARS spectra of an equimolar mixture of AMP/ADP/ATP in water at a total concentration of 500 mM. The dashed line is the error phase providing the slowly varying background to the ME phase. (B) Comparison of the retrieved $\mathrm{Im}(\chi_R^{(3)})$ spectrum (black) and the independently measured spontaneous Raman (red) spectrum of the solution. Reproduced from reference [202].

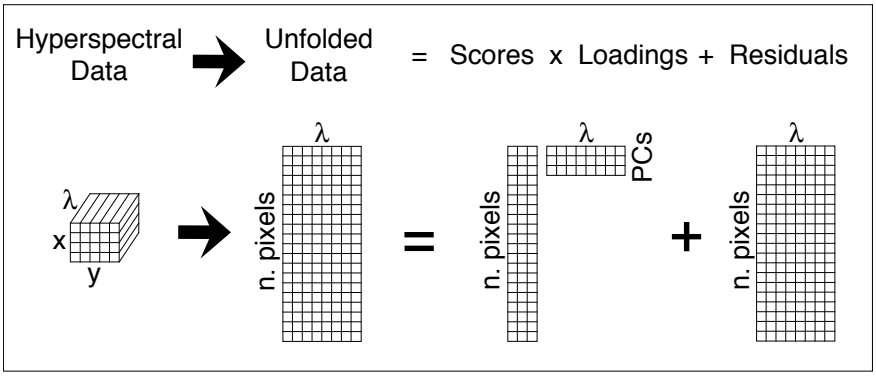

FIGURE 2.3. Representation of the mathematical procedure of Principal Component Analysis. In the first step the hyperspectral datacube is unfolded to be expressed as a two dimensional matrix where each row contains one of the point spectra. This matrix is processed with the PCA algorithm in order to be expressed as the product of two matrices, the *scores* and the *loadings*, summed to a *residuals* matrix. The mathematical procedure underlying this identity, and the physical meaning are discussed in details in the text

the output. The term hyperspectral refers to spatially resolved data with distinct spatial coordinates, and an entire vibrational spectrum collected for each of these three dimensional points. The simplest way to deconvolute overlapping spectral features from multicomponent mixtures occurs when the pure spectra of the individual components are known in advance. In this case, each spectrum in the hyperspectral image is treated as a linear combination of the pure spectra, and the resulting linear coefficients are proportional to the concentration of each component in that spectrum. Constraints to remove unphysical results such as negative concentrations can also be included [20]. As the spectra of the pure compounds in the sample are hardly ever available for biological samples, different mathematical approaches are required for the analysis of these large datasets [50]. In recent years methods of chemometrics are becoming useful tools in vibrational spectroscopy, both IR and Raman, due to their capability to detect small recurring differences in the spectra in presence of large random variance, in order to reveal the simplified structures often hidden in complex datasets [54]. This is particularly important in the analysis of CARS measurements of biological matter, as the chemical composition of the sample is inhomogeneous even on the lenght scale of a few nanometers, and the spectral features of different components are largely overlapping.

The chemometric method selected for the interpretation of the results of Chapter 6 and Chapter 7 is Principal Component Analysis (PCA). For a detailed treatment of the theory underlying the method we refer to general books on chemometrics, *e.g.* [1, 106]. Here only a basic treatment of PCA theory will be outlined.

PCA deals with the hyperspectral dataset using simple theorems and operations of linear algebra following a procedure exemplified in Fig. 2.3. The hyperspectral data (for simplicity illustrated here for the two dimensional case) is initially represented by an intensity matrix of dimensions (x, y, λ), where λ is the number of entries in each spectrum. This can be easily rewritten as an unfolded matrix S containing $n = x \times y$ rows. These rows contain the λ intensity data points of the individual spectra recorded at each spatial position. The spatial information will be retrieved at the end of the procedure. This procedure implies that the spatial correlation of the spectral information is not a factor taken into account in the analysis. Using linear algebra it is always possible to write the unfolded data matrix S as the product of two matrices, called here the *scores* and the *loadings* matrices with dimensions (n, k) and (k, λ) respectively[e], summed to the *residuals* matrix with the same dimensions as S. The physical meaning of this decomposition in PCA is intuitively equivalent to the spectral decomposition of a vector along the "most meaningful" set of basis vectors that describes the space. This near equivalence contains the implicit goal of PCA which is to find a new basis, linear combination of the original basis, best re-expressing the experimental dataset, filtering out the noise and revealing the hidden structure of the data. In other words, the aim of PCA is to find the matrix transformation that minimizes the redundancy and maximizes the signal in our dataset.

The first step of the analysis is to construct the covariance matrix C starting from the unfolded data matrix S as follows:

$$C = SS^T \tag{2.15}$$

C is a (λ, λ) matrix, in which each term $C_{u,v}$ is the product of the intensity values at wavelengths λ_u and λ_v summed over all spectra.

- The diagonal terms $C_{u,u}$ represent the *variance* of a particular wavelength λ_u. Hence, large values correspond to a relevant spectral feature.

- The off-diagonal terms $C_{u,v\neq u}$ represent the *covariance* of two wavelengths λ_u and λ_v. Here large values correspond to a high redundancy in the measurement.

In order to minimize redundancy and maximize the signal, one needs to manipulate the covariance matrix so that

- The off-diagonal terms should become zero, *i.e.* the modified covariance matrix should be diagonal.

- Each successive dimension in the modified covariance matrix should be rank-ordered according to variance.

[e]The value of k corresponds to the number of Principal Components needed to describe the dataset. This parameter is determined during the analysis according to the variance associated with each of the components.

In the language of linear algebra these requirements correspond to diagonalizing the correlation matrix by solving the equation

$$P^T C P = \Lambda \tag{2.16}$$

P is the eigenvector matrix, from which the Principal Components matrix, the *loadings* matrix Z, is calculated according to

$$Z = SP \tag{2.17}$$

The eigenvalues Λ provide the variance associated with each corresponding principal component.

The meaning of this mathematical procedure is to find a new basis of orthonormal vectors, the eigenvectors. The first eigenvector is aligned to the direction of larger variance; the second is aligned to the direction of larger variance in the $(\lambda-1)$-dimensional subspace orthogonal to the first eigenvector, and so on. Hence the Principal Components are the original spectra expressed along this rotated basis. The original unfolded data matrix S can hence be expressed in terms of the Principal Components as

$$S = \alpha Z \tag{2.18}$$

where α is the scores matrix

$$\alpha = P^T \tag{2.19}$$

The meaning of Eq. (2.18) is explained in Fig. 2.4. The rows of the loading matrix Z are the individual Principal Components ordered according to the associate variance. These functions are not actual spectra as they do not fulfill the non-negativity requirement of physical spectra, although the peaks express the most relevant chemical features found throughout the sample[f]. The scores matrix α determines how much each principal component contributes to the spectra from each spatial coordinate. Spectra associated with similar scores relative to a certain PC are likely to have a similar chemical composition, hence the scores values can be used as a criterion to group spectra. Each column of the scores matrix can be folded back to the original (x, y) form to provide a visualization of the spatial distribution of the contribution of the corresponding PC to the local spectra.[g]

Associated with PCA is another method used in this thesis in Chapter 7, the Hierarchical Cluster Analysis. HCA classifies the data according to the smaller

[f] Computational methods beyond the aim of this thesis are available for treating the loadings matrix in order to render it in a physically meaningful form. These methods have been proven to be reliable only for mixtures of a limited number of known chemical components, a condition that is clearly not fulfilled in the case of biological samples.

[g] As PCs are ordered according to the variance, Eq. (2.18) can also be written as $S = \alpha Z + R$ where the matrices α and Z only contain a number k of columns and rows respectively. This is equivalent to include in the matrix multiplication only the most meaningful PCs, and move in the residuals matrix R only the less meaningful information including the noise. This procedure is often called Singular Value Decomposition and is often used as a filter in measurements with large associated noise.

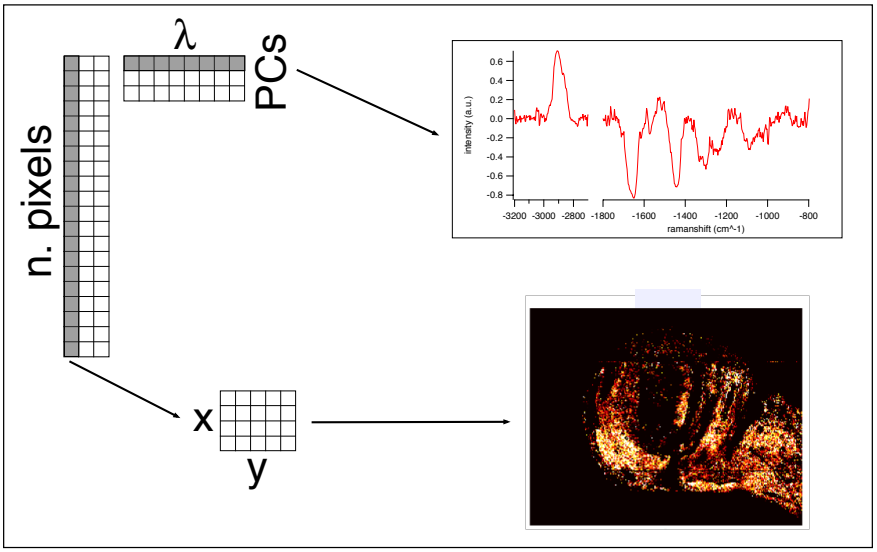

FIGURE 2.4. Representation of the final results of PCA analysis on hyperspectral data. On the left the original data are expressed as the product of the *scores* and the *loadings* matrices as explained in the text. Each individual row of the *loadings* contains a pseudo-spectrum representing one Principal Component. These spectra are ordered according to the associate variance and identify the most important chemical features present across the sample. The columns of the *scores* contain the information on how large is the contribution of the corresponding PC at each position in the sample. Hence the individual columns can be folded back to the (x, y) format of the original data and presented as a false-color map that highlights the spatial contribution of each of the PCs.

distance in the spectra as expressed by the correlation coefficients. Here the correlation matrix C' is calculated as

$$C' = S^T S \tag{2.20}$$

C' is a symmetric $(n \times n)$ matrix where off-diagonal terms $C_{i,j}$ contain the correlation between the i-th and j-th spectra summed over all the wavelengths of the spectrum. This matrix is searched for the term closest to unity, which identifies the most similar spectral coefficients, and the corresponding columns are merged reducing the dimensionality of the correlation matrix. The correlation coefficients are recalculated and the merging process is repeated while keeping track of the spectral entries being merged into the different clusters. Mean cluster spectra can be calculated, representing the chemical composition of all spectra in a specific cluster, and pseudo-maps of the system based on spectral similarities are obtained.

It is important to underline that since both PCA and HCA are non parametric methods, they require no external input that could influence the final

results. This non parametric nature also imposes some limitations to the methods, related primarily to its underlying assumptions:

- The new basis that redefines the data is orthonormal. If this assumption is fulfilled, linear algebra theorems apply to the problem.
- The most relevant chemical features are associated with large variance in the system. This is true only if the signal to noise ratio (SNR) in the measurement is large. In this case the PCs associated with large variance are physically relevant, while the PCs with lower variance contain primarily noise.

2.4 Appendix: derivation of the CARS susceptibility

We showed in Eq. (2.2) that the total third order susceptibility is the sum of a frequency dependent resonant part, and a nearly frequency-independent non-resonant part, where only the resonant part of the response contains the spectral properties of normal Raman transitions.

The analytic form of the resonant part of the susceptibility can be calculated both with a classical and quantum mechanical approach. Here, we follow the classical treatment for the calculation of $\chi_R^{(3)}$ [14]. In the following equations we use the harmonic oscillator approximation to describe the potential of the vibrational states. The initial assumption in this derivation is that we can treat the electric dipole induced in the molecule, *i.e.* the optical molecular polarizability α, as function of the bond stretching coordinate q. Using Placzeks development:

$$\alpha = \alpha_0 + \left(\frac{\partial \alpha}{\partial q}\right)_0 + \dots \tag{2.21}$$

where the first term is the polarizability of a molecule in which the internuclear distance is held fixed at its equilibrium value. The force produced on the oscillator by an external field due to this polarizability is then expressed as[h]:

$$F = \frac{1}{2}\left(\frac{\partial \alpha}{\partial q}\right)_0 E^2 \tag{2.22}$$

giving the following equation of motion for the damped harmonic oscillator (where Γ is the damping constant, ω_ν is the resonant frequency of the oscillator):

$$\ddot{q} + \Gamma \dot{q} + \omega_\nu^2 q = \frac{1}{2m}\left(\frac{\partial \alpha}{\partial q}\right)_0 E^2 \tag{2.23}$$

[h] Molecular vibrations are driven coherently in the presence of a field $\tilde{E}(z,t)$. The dipole moment induced by the field in a molecule located at z is given by $\tilde{p}(z,t) = \alpha \tilde{E}(z,t)$. Associated to the oscillation of the dipole moment is the energy $W = (1/2)\langle \tilde{p}(z,t) \cdot \tilde{E}(z,t)\rangle = (1/2)\alpha \langle \tilde{E}^2(z,t)\rangle$, where the average is taken over time. The force applied by the field on the vibrational degree of freedom is then expressed as $\tilde{F} = dW/dq = (1/2)(\partial\alpha/\partial q)_0 \langle \tilde{E}^2(z,t)\rangle$

With the assumption that all incoming radiation fields are propagating along the same direction, the field vector can be expressed as a scalar, and we can express the electric field in complex notation as:

$$E_i(\omega_i) = \frac{1}{2}\left[\xi_i e^{\imath(k_i z - \omega_i t)} + c.c.\right] \tag{2.24}$$

where ξ_i is the amplitude, $k_i = \omega_i n_i/c$ the momentum vector, and c.c. the complex conjugate. The field applied in the CARS process is the sum of two fields: $E = E_{pu} + E_S$, which implies that the coordinate q is driven not only at ω_{pu} and ω_S, but also at the beating frequency $\omega_\nu = (\omega_{pu} - \omega_S)$ where the equation of motion will have another solution. Specifically, we represent the optical field of the CARS process as:

$$E = \frac{1}{2}\left[\xi_{pu} e^{\imath(k_{pu} z - \omega_{pu} t)} + \xi_S e^{\imath(k_S z - \omega_S t)} + c.c.\right] \tag{2.25}$$

We can substitute this expression for the field into Eq. (2.23), and introduce a trial solution. The trial solution is expressed, using the Rotating Wave Approximation [72], in the form

$$\tilde{q} = q(\omega_{pu} - \omega_S) e^{\imath((k_{pu} - k_S)z - (\omega_{pu} - \omega_S)t)} + c.c. \tag{2.26}$$

We obtain the equation of motion in the form

$$-(\omega_{pu} - \omega_S)^2 q(\omega_{pu} - \omega_S) - \imath(\omega_{pu} - \omega_S)\Gamma q(\omega_{pu} - \omega_S) + \omega_\nu^2 q(\omega_{pu} - \omega_S) = \frac{1}{2m}\left(\frac{\partial \alpha}{\partial q}\right)_0 \xi_{pu}\xi_S^* \tag{2.27}$$

leading to the solution

$$q(\omega_{pu} - \omega_S) = \frac{(1/2m)[\partial\alpha/\partial q]_0 \xi_{pu}\xi_S^*}{\omega_\nu^2 - (\omega_{pu} - \omega_S)^2 - \imath(\omega_{pu} - \omega_S)\Gamma} \tag{2.28}$$

Writing the nonlinear part of the polarization as[i]

$$\begin{aligned}\tilde{P}(z,t) = \quad & N\left(\frac{\partial \alpha}{\partial q}\right)_0 \left[q(\omega_{pu} - \omega_S) e^{\imath((k_{pu} - k_S)z - (\omega_{pu} - \omega_S)t)} + c.c.\right] \\ & \left[\xi_{pu} e^{\imath(k_{pu} z - \omega_{pu} t)} + \xi_S e^{\imath(k_S z - \omega_S t)} + c.c.\right]\end{aligned} \tag{2.29}$$

we note that this expression contains several different frequencies components. The Stokes polarization is the part that oscillates at frequency ω_S [14]:

$$\tilde{P}_S^{NL}(z,t) = P(\omega_S) e^{\imath\omega_S t} + c.c. \tag{2.30}$$

with a complex amplitude that can be expressed using Eq. (2.28) as

$$\begin{aligned}P(\omega_S) = \quad & N\left(\frac{\partial \alpha}{\partial q}\right)_0 q^*(\omega_{pu} - \omega_S)\xi_{pu} e^{\imath k_S z} = \\ & \frac{(N/2m)[\partial\alpha/\partial q]_0 |\xi_{pu}|^2 \xi_S^*}{\omega_\nu^2 - (\omega_{pu} - \omega_S)^2 - \imath(\omega_{pu} - \omega_S)\Gamma} e^{\imath k_S z}\end{aligned} \tag{2.31}$$

[i]The polarization is expressed as $\tilde{P}(z,t) = N\tilde{p}(z,t) = N\tilde{\alpha}(z,t)\tilde{E}(z,t) = N[\alpha_0 + (\partial\alpha/\partial q)_0 \tilde{q}(z,t)]\tilde{E}(z,t)$

By comparing this result with the general expression of the polarization given by

$$P(\omega_S) = \chi_R^{(3)}(\omega_S)|\xi_{pu}|^2\xi_S^* e^{\imath k_S z} \tag{2.32}$$

We obtain the expression for the Raman susceptibility

$$\chi_R^{(3)}(\omega_S) = \frac{(N/2m)[\partial\alpha/\partial q]_0}{\omega_\nu^2 - (\omega_{pu} - \omega_S)^2 - \imath(\omega_{pu} - \omega_S)\Gamma} \tag{2.33}$$

We now look at the differential cross section of a molecule exposed to electromagnetic radiation according to the electromagnetic scattering theory:

$$\frac{\partial\sigma}{\partial\Omega} = (\alpha')^2 \left(\frac{\omega}{c}\right)^4 \tag{2.34}$$

where for the Raman Stokes frequency $(\alpha')^2 = (\partial\alpha/\partial q)^2\langle q^2\rangle$. We use the result $\langle q^2\rangle = \hbar/2m\omega_\nu$ valid for a harmonic oscillator. Hence

$$\frac{\partial\sigma}{\partial\Omega} = \frac{\hbar}{2m\omega_\nu}\left(\frac{\partial\alpha}{\partial q}\right)^2\left(\frac{\omega_S}{c}\right)^4 \tag{2.35}$$

We can then invert this relationship and express the susceptibility as a function of the Raman differential cross section[j]:

$$\chi_R^{(3)}(\omega_S) = \frac{Nc^4}{\hbar\omega_S^4}\left(\frac{\partial\sigma}{\partial\Omega}\right)\frac{\omega_\nu\Delta_j}{\omega_\nu^2 - (\omega_{pu} - \omega_S)^2 - \imath(\omega_{pu} - \omega_S)\Gamma_j} \tag{2.36}$$

Close to a Raman-active resonance, where $\omega_{pu} - \omega_S \simeq \omega_\nu$, the susceptibility can be approximated by:

$$\chi_R^{(3)}(\omega_S) = \frac{Nc^4}{\hbar\omega_S^4\omega_\nu}\left(\frac{\partial\sigma}{\partial\Omega}\right)_j\frac{\omega_\nu\Delta_j}{\omega_\nu - (\omega_{pu} - \omega_S) - \imath\Gamma_j} = \frac{A_j}{\omega_\nu - (\omega_{pu} - \omega_S) - \imath\Gamma_j} \tag{2.37}$$

where

$$A_j = \frac{N\Delta_j c^4}{2\hbar\omega_S^4}\left(\frac{\partial\sigma}{\partial\Omega}\right)_j \tag{2.38}$$

[j] We have introduced here the difference in probability of finding the molecule in the ground or excited j-th state using the Schroedinger representation where a0 and aj represent the amplitudes of the two states: $\Delta_j = a_0 a_0^* - a_1 a_1^*$ [130]. Multiplied by the molecular density N, this represents the population difference density between the two states.

3 Experimental methods

In this chapter we outline the experimental methods used in the thesis. For CARS experiments two different setups were employed, a single frequency and a broaband CARS microscope. The single frequency CARS setup was used for the research projects outlined in *Chapter 4*, *Chapter 5*, and *Chapter 6*. This setup allows for simultaneous measurements with other non linear optical techniques which were also used in this thesis, such as Multi-photon Induced Luminescence (*Chapter 5*) and 2-Photon Fluorescence (*Chapter 6*). Broadband CARS was used for the projects in *Chapter 6* and *Chapter 7*.

Transmission Electron Microscopy was used for the project in *Chapter 5* to validate the results on the uptake of gold nanoparticles in cells. Finally, standard fluorescence was used as a complementary technique for the study in *Chapter 7*, using a commercial Olympus IX70 inverted microscope.

3.1 Single frequency CARS

The single frequency CARS microscopy setup consists of a picosecond pulsed laser system generating two synchronized beams collinearly aligned into an inverted microscope (Eclipse TE-2000, Nikon, Tokyo, Japan) via a beam scanning unit (C1, Nikon). A fraction of the fundamental output of a Nd:Van laser (Picotrain, HighQ Lasers GmbH, Hohenems, Austria) at 1064 nm is directly coupled into the microscope serving as the Stokes beam in the CARS process, while its frequency-doubled output (532 nm) is used to synchronously pump an Optical Parametric Oscillator (Emerald OPO, APE GmbH, Berlin, Germany). The tuneable output is provided by the OPO, set to 817 nm in this work to form a beating excitation field with the Stokes beam at the frequency 2845 cm^1 corresponding to the resonant vibration of the CH_2 group in the acyl chain of lipids, so that CARS images predominantly organelles with high lipid content. The laser beams were focused on the sample by an oil immersion objective (Plan Fluor 40x, NA 1.30, Nikon), resulting in a power of 10 mW for each of the beams at the sample position. The CARS signal was collected by an aspherical lens (NA 0.68) in the forward direction and detected by a single-photon counting photomultiplier tube (PMC-100, Hamamatsu) connected to a time-correlated single-photon counting unit (SPCM-830, Becker and Hickl). Bandpass filters (650/50 nm, Chroma Technologies, USA) in front of the detector suppressed the radiation at the laser wavelengths and preferentially transmitted the CARS signal generated at 663 nm. A detailed outline of the setup has been given by Enejder *et al.* [64]. The setup is schematically shown in Fig. 3.1

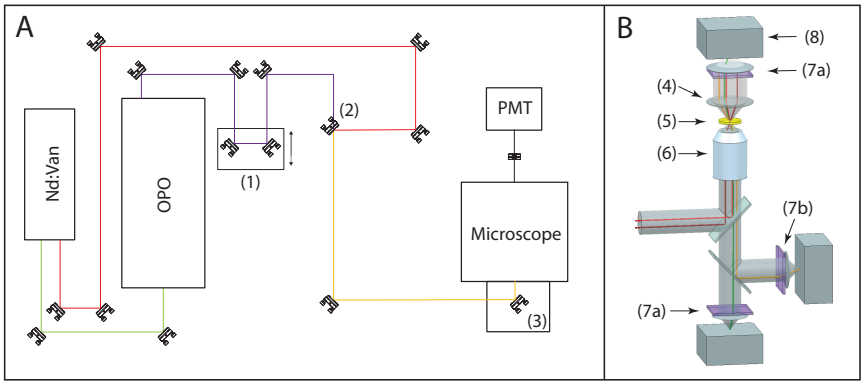

FIGURE 3.1. (A) Schematic representation of the single line CARS setup. The excitation beams (817 and 1064 nm, respectively) from the laser system are coupled through a dichroic mirror into the microscope by a mirror scanner. The spectrally filtered response is collected using photomultiplier tubes (PMTs) either in forward or backward direction. (1) Rail for timing adjustment;; (2) dichroic mirror; (3) resonant scanning mirrors used for fast modulation of the spatial pointing of the beams. (B) Schematic view of the optical path inside the microscope. (4) condenser; (5) sample; (6) objective; (7*a*) CARS band pass filters, *e.g.* 625 - 675 nm; (7*b*) band pass filters for the detection at different wavelength for *e.g.* two photons fluorescence or second harmonic generation; (8) PMT.

3.2 BROADBAND CARS SETUP

The broadband CARS setup is based on a dual-output laser source (Leukos-CARS, Leukos) providing the pump and the Stokes beams. The source is a passively Q-switched $1064 - nm$ microchip laser, delivering $< 1 - ns$ pulses at 32 kHz repetition rate and 300 mW average power. The laser beam is equally divided into two parts with a beam splitter. One part is sent through a band-pass filter ($FL1064 - 10$, Thorlabs) and used directly as the pump beam. The other part is introduced into a photonic crystal fiber that creates supercontinuum emission from 420 to 2400 nm at the fiber output, with > 100 μW nm^{-1} spectral power density from 1.05 μm to 1.6 μm. The supercontinuum is coupled out of the fiber with a reflective collimator ($RC04APC - P01$, Thorlabs) and passed through 700 nm ($FEL0700$, Thorlabs) and 880 nm ($LP02 - 830RS - 25$, Semrock) longpass filters. The Stokes and pump beams are overlapped at a dichroic mirror ($LP02 - 1064RU - 25$, Semrock) and introduced into a modified inverted microscope (Eclipse Ti-U, Nikon). The pump and Stokes pulses are tightly focused onto the sample with a near IR objective (PE IR Plan Apo $100X$, NA 0.75, Seiwa). The sample is mounted on nested stepper-motor driven (Microstage, Mad City Labs) and piezo driven stages (Nano-PDQ 375 HS, Mad City Labs) that together provide 25 mm travel range with < 1 μm resolution. The CARS signal generated by the sample is collected in the forward direc-

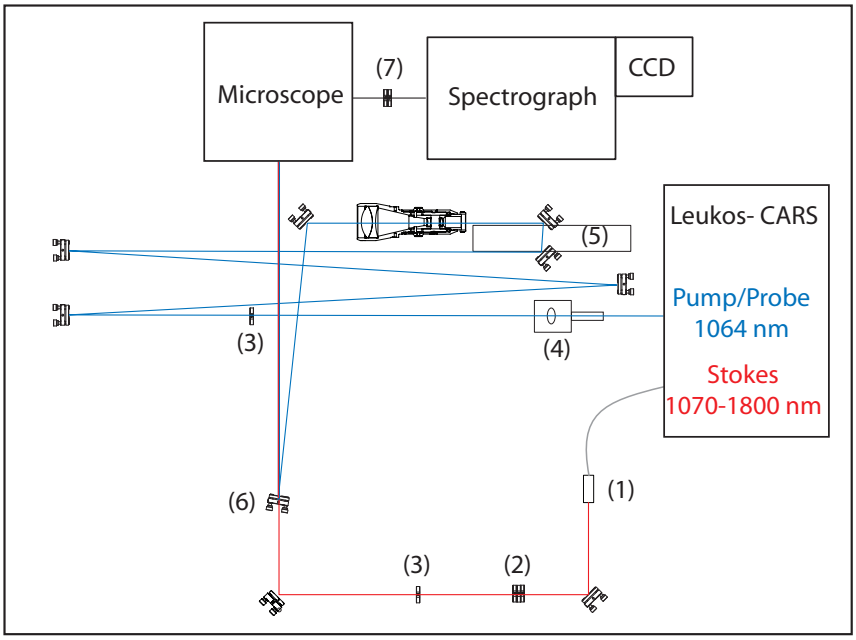

FIGURE 3.2. Schematic representation of the broadband CARS setup. (1) reflective collimator; (2) 880 and 700 nm long pass filters; (3) mounts for N.D. filters; (4) 250 mm lens used to collimate the pump/probe output; (5) Rail for ns timing adjustment; (6) dichroic mirror and 1064 nm notch filter; (7) 1064 nm notch and 1000 nm short pass filters

tion by another objective ($M-20X$, NA 0.4, Newport) and sent through notch ($NF03-532/1064E-25$, Semrock) and short-pass filters ($FES1000$, Thorlabs) to remove the pump and Stokes beams. The filtered CARS beam is dispersed by a spectrometer (Shamrock $303i$, 300 lines mm^1, 1000 nm blaze, Andor) and detected on a deep-depletion CCD (Newton $DU920P-BR-DD$, Andor). The schematics of the broadband setup are outlined in Fig. 3.2.

This setup allows to acquire CARS spectra with spectral resolution of $8-15$ cm^{-1} depending on the grating used. The acquisition time can be as short as 2 ms, although typical experiments on biological samples were performed with acquisition times between 100 ms and 1 s. The optimized spatial resolution of the system is less than 1 μm in plane and about 2 μm axially.

3.3 TRANSMISSION ELECTRON MICROSCOPE

In order to validate the results on the uptake of gold nanoparticles in cells, transmission electron microscopy was used. The sections of the cells were collected on copper grids and contrasted with uranyl acetate and lead citrate before exami-

nation in a Zeiss 912AB electron microscope (Carl Zeiss SMT AG, Oberkochen, Germany) equipped with a LaB6 electron source operated at at 120 kV. Images were collected using a MegaView III CCD camera (Olympus SIS, Mnster, Germany).

4 Visualization of MRI contrast agents in living cells

Micrometer-sized iron oxide particles (MPIOs) attract increasing interest as contrast agents for cellular tracking by clinical Magnetic Resonance Imaging (MRI). Successful cellular uptake of the MPIOs is the crucial prerequisite for determining the outcome of cell transplantation by MRI. Despite the great potential of MPIOs for *in vivo* imaging of MPIO-labeled cells, little is known about the intracellular localization of these particles following uptake due to the lack of techniques with the ability to monitor the particle uptake *in vivo* at single-cell level. Here, we show that single frequency CARS microscopy enables non-invasive, label-free imaging of MPIOs in living cells with sub-micron resolution in three dimensions. CARS allows simultaneous visualization of the cell framework and the MPIOs, where the particles can be readily distinguished from other cellular components of comparable dimensions, allowing accurate determination of their location inside the cell.

4.1 Introduction

Cell transplantation using *e.g.* stem cells, progenitor cells and adult cell lines constitutes a promising approach for treatment of several human diseases [115, 138], and has already been tested for clinical treatment of cardiovascular, neurological, and metabolic disorders [53, 70, 90, 115, 137]. The advantages compared to whole organ transplantation are many: the treatment is less invasive, cryopreserved cells can be used, and it provides the possibility that an organ from a single donor can be used for treatment of multiple patients [52, 71, 110]. To understand- and ultimately improve - cell transplantation schemes, knowledge has to be gained regarding the fate of cells following transplantation: monitoring cell transplantation is crucial for the success of the therapy. As a result, substantial effort has been devoted to the development of techniques to image individual cells in live organisms. Such imaging allows the detection of the early stages of cell homing, tracking cell migration, and the visualization of complications such as microembolization of transplanted cells [23, 141, 170, 172].

The outcome of cell transplantation in clinical trials has been investigated

via biopsies from the target organ, using visualization by radioisotope imaging [11]. This approach has serious limitations, however: it is associated with a risk for the patient due to the invasive procedure and constrained by the fact that only a limited part of the organ can be investigated, and only at limited numbers of moments in time. Alternatively, optical labels have been tested in the visualization with Near Infrared Fluorescence (NIRF) Optical Imaging of the development of transplanted cells *in vivo* in a preclinical rat-model [114]. A major drawback of this method is that NIRF-dyes are only detectable up to a tissue thickness of about 2 to 3 cm *in vivo* [121] and that the NIRF-dye must present antigen specificity. The discovery of immunospecific NMR contrast agents [176] has enabled magnetic resonance imaging (MRI) as a suitable tool for non-invasive tracking of transplanted labeled cells. The technique was first employed for imaging single cells *in vitro* [56,187] and has since been extended to cells *in vivo* [5, 185]. MRI is currently the most common imaging technique for tracking *in vivo* labeled cells owing to its high resolution, and enhanced tissue contrast [89]. This technology further benefits from its widespread availability in clinical environments. The progress of the technique *in vivo* relies primarily on the choice of cell labels that are easily internalized by cells and can be readily visualized by MRI. However, to date it has remained challenging to fully elucidate the cellular uptake mechanism of these particles. In this study, we present a combination of resonant and non-resonant single frequency CARS microscopy as a useful tool for the visualization of MRI labels in living cells.

Paramagnetic Gadolinium (Gd) chelates are commonly used as T_1 contrast agents, although their low permeability through the cell membrane requires high concentrations combined with long incubation times for efficient internalization, and the detectability of labeled cells was found to be insufficient for clinical applications [40]. Gd-based metalloporphyrins, *e.g.* gadophrin-2 [46], and amphiphilic chelates, *e.g.* Gadofluorine M [99], are readily internalized by cells, but high concentrations are still required for MRI detection. Perfluorocarbons have also been investigated as cell labels [191] with the advantage that ^{19}F MRI provides background-free imaging of the cells. Regrettably, they exhibited inadequate signal intensity levels. Superparamagnetic iron oxide (SPIO) nanoparticles have successfully been used as T_2 and T_2* contrast agents and exhibit higher contrast compared to normal paramagnetic particles [100, 160]. SPIOs possess very high molar relaxivity, giving rise to contrast that well exceeds the physical dimensions of the particles *in vitro*. In addition, their magnetic properties can be tailored by modifying the particle size and aspect ratio [129]. These particles are negative contrast agents, appearing as pronounced hypointense regions in MR images. The major drawback of nanometer-sized SPIOs as labels is that a significant number of particles is required within a voxel for efficient detection. Thus, the dilution of the label as a result of cell division inevitably reduces the local concentration below the detection limit after a few cell division cycles [187]. SPIOs have primarily been used for detecting single cells *in vitro* [143] (for a general review on primary human hepatocytes see [127]), but also *in vivo* by clinical MR equipment [49]. Clinical MRI was found to be limited by the relatively low field strength and resolution compared to what

was shown in experimental studies [135]. The conclusion from these efforts is that larger particles creating a greater magnetic moment within the cells would be desirable for efficient detection of labeled cells under clinical conditions. Labeling with micrometer-sized iron oxide particles (MPIO) with higher magnetic relaxation compared to SPIOs constitutes a promising approach towards optimized imaging capabilities. It has been shown that MPIOs exhibit increased relaxation compared to nanometer-sized particles with the same total iron content per unit sample volume [101]. MPIOs can be easily internalized by several types of cells and allow for labeling capacity up to hundreds of picograms of iron per cell without affecting cellular viability [186]. For instance, primary human hepatocytes can be labeled with MPIOs without negative effects on cellular integrity or metabolic activity [175]. MPIOs have been used for MR imaging of cells both *in vitro* [101, 187] and *in vivo* [185], and it has been shown that even a single MPIO can be detected by MRI at a resolution of 100 μm [186]. Single particle sensitivity implies that MRI detection is not compromised by cell division due to dilution of the label.

Efficient uptake of the label is a crucial step for cell tracking, and an understanding of the underlying mechanisms is crucial for optimizing the labeling process. Also, unambiguous determination of the average number of MPIOs taken up per cell is crucial to evaluate MRI results and adapt the labeling protocol. Much research is expected to be dedicated to structural and functional modifications of the particles in order to achieve both better MRI contrast and specific cellular uptake. Any imaging technique that would support these studies must fulfill quite stringent requirements. The technique must firstly be non-invasive in order not to affect the viability of the cells, and label-free in order to study the interaction between the cell and the MPIOs under realistic and biologically relevant conditions: all invasive forms of sample preparation such as staining and sectioning are undesirable; finally, it must offer sub-cellular resolution, three-dimensional imaging capabilities and contrast from both MPIOs and cells. The ability of present technology to monitor intracellular localization of MPIO is still rudimentary due to the difficulties of co-localizing the particles with cellular components without the use of labels. Conventional brightfield microscopy based on light transmission is the fastest and least invasive approach for visualizing the particles *in vitro* [175,186], but unfortunately provides neither chemical selectivity nor sufficient axial resolution. In this technique, MPIOs are identified from their shape, with the risk of false positive identifications from large lipid droplets or other circular organelles in the cell. Due to the limited axial resolution, it is challenging to retrieve information on the localization of the particles relative to intracellular features from this approach. Knowledge of the location of particles is especially important relative to the cytoplasmic membrane; brightfield microscopy is not able to differentiate between a microparticle sitting outside the cell from one that has been internalized but still located in proximity to the membrane. Multi-channel confocal and two-photon fluorescence microscopies provide a viable alternative, allowing for visualization of fluorescently labeled components of the cells and labeled particles [185]. For instance, one among many possible options is double staining for cytoplasmic

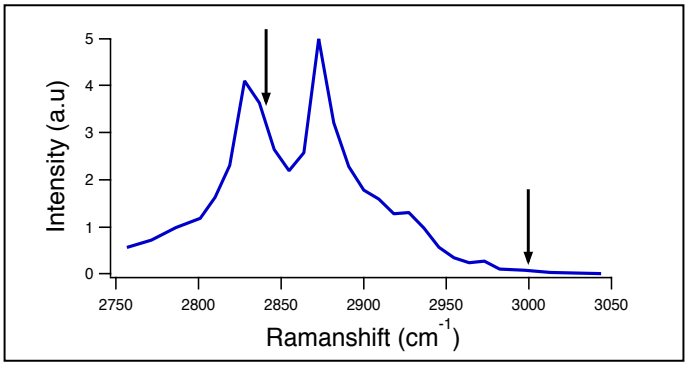

FIGURE 4.1. Normalized CARS spectrum of tripalmitin; The arrows at 2845 cm^{-1} and 3000 cm^{-1} indicate the typical response of biological matter at the frequencies used for on- and off-resonance CARS measurements.

proteins and nucleus, combined with additional staining of MPIOs [175]. While multi-channel fluorescence microscopy overcomes the spatial resolution issues of light microscopy [145], the approach is limited to the visualization of the particles relative to one or a few intracellular components, which in addition are studied under artificial conditions in the presence of multiple fluorescent marker molecules. In systems so critically dependent on local chemical and physical properties as the nano-bio interface, the presence of additional labels is undesirable as it can perturb the nature and dynamics of biological and physical interactions. Transmission electron microscopy (TEM) has also been used to visualize the uptake of MPIOs [181]. TEM has the ability to resolve both particles and cellular components on nanometer lengthscales. However, significant limitations of this approach may be noted, including the time-consuming and highly invasive sample preparation associated with potential artefacts [180]; cell fixation, resin embedding and slicing of the cells. This technique also precludes studies of the temporal characteristics of the particle internalization process.

As we will show here, the combination of resonant and non-resonant CARS microscopy represents a useful label-free approach to the visualization of MPIOs in living cells. The particles are readily distinguished from micrometer sized cellular features such as cytoplasmatic lipid bodies based on their high density of electrons. The approach is shown to provide accurate localization of the particles with respect with the cell body. The visualization of both particles and cells is achieved with CARS, as outlined in Chapter 1, high spatial resolution is ensured both laterally (300 nm) and axially (1 μm) with three-dimensional imaging capabilities [28]. We refer here to CARS as a special case of Four Wave Mixing (FWM) where three incident fields, two with degenerate frequency ω_{pu} (pump/probe beam), and a third with frequency ω_S (Stokes beam), interact through the third-order susceptibility of the probed material, generating a blue shifted fourth field at the anti-Stokes frequency $\omega_{AS} = 2\omega_{pu} - \omega_S$.

Keeping in mind the expression of the total molecular susceptibility of Eq. (2.2) as the sum of the resonant and non-resonant term, performing an on-resonance CARS microscopy measurement means tuning the energy difference of the exciting beams to match a vibrational resonance of a specific chemical present in the sample, *e.g.* the methylene stretch abundant in lipids. In the off-resonance measurement on the other hand, the beams are tuned away from all vibrational resonances, and the intensity of the response only depends on the magnitude of $\chi^{(3)}_{NR}$ and in turn on the electron density of the compound being illuminated. The bioorganic molecules of the cell and the inorganic oxide of the MPIOs can be visualized by tuning the frequency difference of the fields to be on- ($\omega_{pu} - \omega_S = 2845\ cm^{-1}$) and off-resonance ($\omega_{pu} - \omega_S = 3000\ cm^{-1}$) with the symmetric stretch vibration of the CH_2 groups. Fig. 4.1 shows the normalized CARS spectrum of tripalmitin as an example of the response of biological matter at the frequencies used for the on- and off-resonance measurement indicated in figure by arrows. On-resonant excitation yields an enhanced CARS signal from lipid-rich components of the cells [64], accompanied by a strong non-resonant electronic signal from the MPIOs due to the high electron density of the iron oxide. Off-resonant excitation provides a weak non-resonant signal from the cells, but the strong non-resonant electronic signal from the MPIOs remains. The difference in the magnitude of the non-resonant signals arises from the large difference of the electronic susceptibility of iron oxide (4×10^{-10} esu [95]) compared to that of biological matter (typically 10^{-13} esu [147]). It is important to underline that due to the large dimensions of MPIOs, the particles have the same physical properties of bulk iron oxide. Owing to the very small bandgap of this material (E_{gap}=0.14 eV, corresponding to a band edge absorption of 8.8 μm), the optical response in the visible and near-IR wavelength range is largely frequency independent. The results obtained here for our CARS setup with its specific combination of wavelengths should therefore be generally applicable to other CARS setups as well, as this wavelength range includes the excitation wavelengths of the beams normally employed in CARS experiments. As the contrast is derived from molecular properties, no additional staining of the sample is required for imaging [48, 98]. Additionally, the use of excitation beams in the near-infrared is particularly suitable for imaging biological samples as the absorption cross-section of water is low in this region [152].

CARS has previously been employed to visualize gold nanoparticles in cells [173], as well as wide bandgap semiconductor oxide nanoparticles in biological systems [142, 214]. In the latter works, the energy of bandgap absorption of a material is matched by the second harmonic of one of the excitation beams, resulting in a third term that contributes to the molecular susceptibility arising from two-photon electronic resonance in Eq. (2.2). The response of these particles is enhanced and gives rise to very high signals that allow to readily distinguish the particles from their environment [207]. The enhancement is nevertheless limited to the coupling of the two photons to the electronic states in the vicinity of the energy gap, where the effects of excitons are expected to be larger [25, 198]. This effect is negligible in magnetite as, contrary to other oxides, this material has a small bandgap of 0.14 eV. Two consecutive CARS

measurements, on -and off-resonance, are hence necessary to distinguish MPIOs from the biological components. This apparent drawback turns out to be an advantage as the overlay of on- and off-resonance CARS measurements of the same region provides unambiguous determination of the location of each MPIO within the cell, and intrinsically discriminates between them and micrometer-size lipid structures that may easily be confused in brightfield images of the cells.

4.2 Materials and methods

4.2.1 Micron-sized iron oxide particles

MPIOs were obtained from Microparticles GmbH (Berlin, Germany). The average diameter of each microparticle is 1.18 +/- 0.08 μm. Microspheres consist of a silica based matrix with homogeneously incorporated iron oxide nanoparticles (40 vol-%). A hydrophilic polymer layer surrounds the core to prevent leaching of iron species. Additionally streptavidin functionality was introduced at the surface of the particles via 1-ethyl-3-(3-dimethylaniminopropryl) carbodiimide (EDC)-coupling. The particles have a narrow size distribution, are superparamagnetic and show a very good colloidal stability in phosphate buffered saline (PBS) solution. The concentration of the particles in 1% w/v aqueous stock suspension was 7.088×10^9 particles per mL, resulting in an iron content of approximately 2.88 mg/mL. Subsamples from the stock solution were dissolved in PBS to a suspension concentration of 10^7 particles/mL and stored at 4^oC under sterile conditions until cell incubation.

4.2.2 Cell cultures and incubation with MPIOs

Cryopreserved HuH7 cells, from a well-differentiated human hepatoma cell line, were purchased from JCRB Cell Bank (Osaka, Japan). Cells were thawed in a water bath and cultured in 25 mm^2 culture flasks (Sarstedt, Nrnberg, Germany) using Dulbeccos minimal essential medium (Biochrom AG, Berlin, Germany), supplemented with 10% fetal bovine serum (FBS), 1% L- Alanyl- L- Glutamine (200mM), 1% sodium pyruvat (100mM) and 1% penicillin-streptomycin at 37^{o}C with 5% CO_2 atmosphere and 100% humidity. The cultures were passaged until a confluent layer was formed. Cells were washed with PBS and then released from the flask by incubating with 0,05% trypsin/0,02% EDTA for 4 min at 37^{o}C. Growth medium at 4^{o}C with 10% FBS was added to the cell suspension in order to stop the enzyme activity. A representative number of HuH7 cells were stained with Tryphan blue and counted in a hemocytometer. 100,000 living cells were seeded on sterile WillCo petri dishes (series GWSt-5030) with a 0.17 mm thick glass bottom and allowed to attach for 1 h at 37^{o}C in 5% CO_2. Cells were washed and fresh medium was supplied.

Particles were gently resuspended prior to incubation, and 1mL particle solution was added to 1 mL growth medium in the dish. The MPIO amounted to 100 beads per cell. The cells were incubated for 4h at 37^{o}C in 5% CO_2. As

controls, native cells were treated identically, but without particles. To remove free particles after incubation, the cells were extensively washed with PBS. The slides with the living cells were immediately transferred to the microscope for imaging. After the procedure it was visually confirmed that the cells were still intact. The time span between seeding the cells, particle incubation and CARS measurements lasted no longer than 48h.

4.2.3 On- and off- resonance CARS

The combination of on- and off- resonance CARS measurements was implemented on the experimental setup described in Paragraph 3.1 of this thesis. The output of the OPO was set either to 817 nm or 807 nm in order to form a beating excitation field with the Stokes beam at the frequencies of 2845 cm^{-1} and 3000 cm^{-1} respectively. The Raman shift of 2845 cm^{-1} corresponds to the symmetric stretch vibration of the CH_2 group in the acyl chain of lipids (on-resonance measurement), whereas the Raman shift of 3000 cm^{-1} corresponds to a spectral region where lipid structures present a low response (off-resonance measurement). This can be seen in the CARS spectrum in Fig. 4.1 collected from a tripalmitin crystal as an example of a typical saturated fatty acid compound, where the intensity of the response at the above frequencies is marked with arrows. Prior to the imaging measurements, we tested the optimal experimental conditions and found that this laser power combined with an imaging time of 20 s per image (256x256 pixels) provided optimal results in that both the cells and the particles are clearly visible in the images without compromising the viability of the cells.

Three-dimensional imaging was achieved by scanning a sequence of horizontal planes at different vertical positions by translating the objective with a motorized stage. Samples were first imaged in brightfield mode and the regions of interest, typically covering an area of $30 \times 30\ \mu m^2$ (256×256 pixels), were then measured by CARS, and eventually imaged at different vertical positions with 1 micron spacing. On-resonance and off-resonance images of the same region of the sample were collected consecutively by changing the wavelength of the OPO and allowing for ~ 1 minute stabilization of the laser system. The output of the OPO was optimized for the on-resonance measurement, and the same settings were kept in the off-resonance measurement resulting in a small loss of power. The total acquisition time for each layer was 20 s at each wavelength. The tripalmitin CARS spectrum of Fig. 4.1 was measured under similar experimental conditions as the cell studies, images were collected on a tripalmitin crystal with the OPO tuned to wavelengths in the range 802-823 nm, thus probing frequencies between 2750 and 3050 cm^{-1}. For each tripalmitin image a corresponding reference image of the sample cover glass was measured for CARS signal normalization, and the spectrum shows the average normalized crystal signal versus probed frequency.

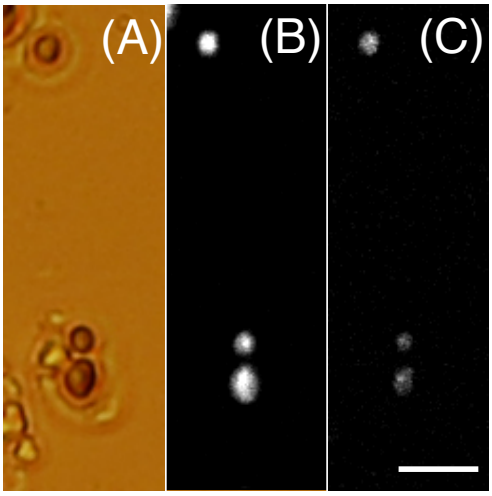

FIGURE 4.2. Brightfield microscopy (A), on resonance (B), and off resonance (C) CARS images of a 10×30 μm^2-sized region of dried solution of MPIOs. Scale bar 5 μm. The normalized intensity of the signal measured from MPIOs on- and off-resonance is identical within the variations that result from frequency tuning.

4.3 RESULTS AND DISCUSSION

4.3.1 IMAGING OF DRIED MPIO SOLUTION

To ascertain selective imaging of MPIOs in cells, on-resonance and off-resonance images were first collected on a reference sample of pure MPIOs. A droplet of solution containing 10^8 particles/mL of MPIOs was left to dry for one hour on a conventional microscope cover slip before imaging with both brightfield and CARS microscopy. Fig. 4.2 (A) shows a brightfield microscopy image of a region of the sample where three MPIOs can be identified. The same region was consecutively imaged with CARS, first with the pump and Stokes beams tuned to match the excitation energy of CH_2 bonds (on-resonance measurement), presented in Fig. 4.2 (B), and then with the beams tuned away from the resonance (off-resonance measurement), presented in Fig. 4.2 (C). Each of the three images covers an area of 10×30 μm^2.

By overlaying the on- and off-resonance CARS images in Fig. 4.2 (B) and (C), perfect colocalization of the features is obtained. Due to the lack of resonant signal together with a strong non-resonant contribution, the three particles are clearly visible in both CARS images, indicating that the optical contrast is not of vibrational origin but is related to a purely electronic response. Hence, for the measurements reported in Fig. 4.2 (B) and (C), one would expect the same signal strength. The decrease in signal intensity in off-resonance mode (Fig. 4.2 (C)) is not of physical origin but can be ascribed to the experimental procedure; the set-up is initially optimized for the on-resonance measurements.

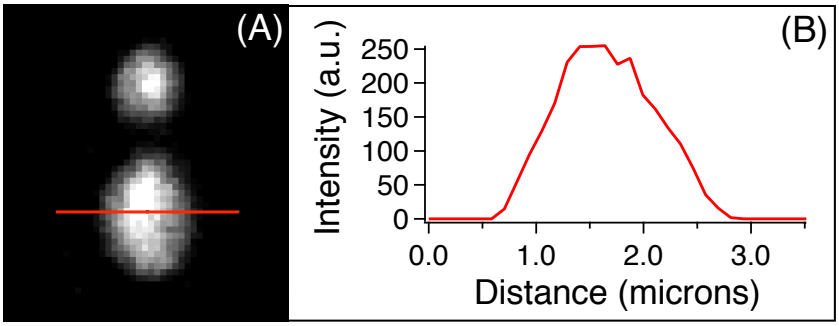

FIGURE 4.3. (A) Zoomed image of an area of interest of Fig. 4.2 containing two MPIOs. (B) Intensity profile of the CARS signal along the red line drawn in panel A across the diameter of one of the MPIOs. The profile is compatible with the response expected from a particle with 1.2 μm lateral dimension.

To minimize the time between the two consecutive measurements no additional optimization was performed after tuning the instrument to off-resonance excitation wavelength, resulting in a power loss in the output of the OPO. This can be confirmed by observing that also the reference signal measured from the glass cover slip is reduced accordingly between the two measurements. Within the signal fluctuation and variations resulting from frequency tuning, the signal intensities measured on- and off-resonance are identical after normalization by the reference response measured in glass.

We conclude from the CARS images presented in Fig. 4.2 that the contrast, or signal to background ratio, is in both cases (on- and off-resonance) large enough to enable precise identification of the particles. Since the dimensions of the particles are larger than the excitation wavelengths, detection of the CARS signal occurs here in forward direction. Extending this imaging approach to nanometer sized magnetite particles would instead be likely to benefit from epi-detection of the back-scattered signal, as backward collection geometry is preferable for the visualization of objects with lateral dimensions comparable to or smaller than the excitation wavelength [29]. The intensity profile taken along the diameter of any of the three round shapes fits well with the response expected from a 1.2 μm sized particle (Fig. 4.3).

4.3.2 IMAGING OF HUH7 CELLS IN ABSENCE OF MPIOS

Before interpreting the images of HuH7 cells incubated with the microparticles, the typical CARS response of these cells was characterized and compared with conventional brightfield microscopy. Fig. 4.4 (A) shows a brightfield microscopy image of a single cell. The cell is flat and spread over a large area, with peripheral terminals visible at its edge, giving rise to additional contact between the cell and the glass support. The nucleus is visible in the center of the image. Its irregular shape is typical for tumor cell lines. Cellular features have low

contrast, except for the many anonymous circular features with diameters of $\sim$ 1 μm that surround the nucleus. From this image it is clear that MPIOs will be difficult to distinguish from other intracellular features by conventional brightfield microscopy. The on-resonance CARS response of the same area (30×30 μm^2), imaged at an axial position ~ 2 μm above the glass surface is shown in Fig. 4.4 (B) . This image appears similar to the brightfield microscopy, but it is important to underline that the CARS image is not merely a map of density or light transmission variations, but contains local chemical information as the intensity of the response is correlated to the concentration of CH_2 bonds within the focal volume. The peripheral terminals are not as clearly visible in the CARS image, indicating that these are located at an axial position closer to the supporting glass. Several features with particularly high intensity appear, leading us to conclude that these are lipid bodies, known to exhibit large CARS signals in this frequency range. The number of droplets is significantly smaller than the number of micron-sized features in the brightfield image, which illustrates an important limitation of conventional microscopy; the brightfield image is a projection of the entire cell volume showing all cellular features irrespective of their chemical composition or axial position. The CARS image instead gives a chemically specific picture of the distribution of lipids within a 1-μm thick focal plane. These lipids are present both in dense lipid droplets and in the cytoplasm (see Fig. 4.4 (B)). The on-resonance CARS signal is particularly helpful to identify the outline of the cell and the nucleus. The nucleus can be identified in an indirect way as the round region in the center of the cell where the high intensity features indicating the presence of lipid-rich aggregates are not present. The nucleolus is barely visible, indicating that it is located at a different axial position (compare Fig. 4.5 (A)). These imaging capabilities of CARS microscopy are of particular importance in order to determine whether the MPIOs actually have entered the cells, and if so, to distinguish the particles from natural intracellular components of similar size. The off-resonance CARS image of the area is presented in Fig. 4.4 (C). The image appears as a negative of the on-resonance image, with intensities lower or similar to that of the medium surrounding the cell. The appearance of the lipid bodies as dark regions in Fig. 4.4 (C), *i.e.* giving a lower CARS signal off-resonance than both the water surrounding the cell and the aqueous solution inside the cell, can be traced to the relatively large signal from the water at the off-resonance frequency (3000 cm^{-1}) that arises from the flank of the broad OH stretch, and hence presents low but non-zero CARS response. In the lipid bodies, where no (or very little) water is present, the CARS response is truly off-resonance; in both water environments the tail of the water response gives rise to small, but finite signal. It is particularly remarkable how this effect makes the edges of cell and nucleus well defined and readily visible in comparison with the background. This negative-like response is useful as it still gives an indication on the localization of cellular components in the off-resonance measurements where primarily MPIOs are detected. It is important to note that the lipid bodies in the cytoplasm are likely to slightly change their position over time, but in most cases the time between different CARS images is short enough so that the lipid

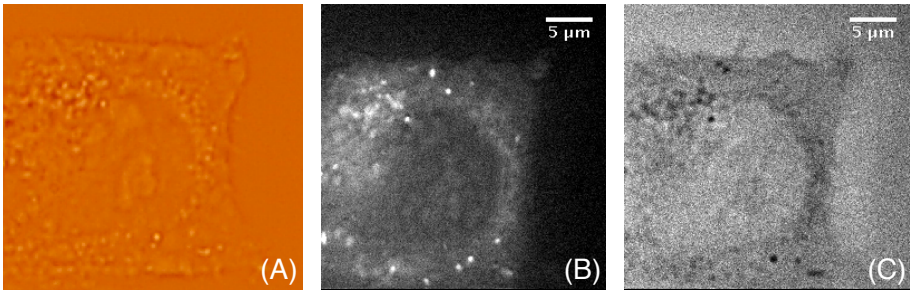

Figure 4.4. Brightfield microscopy (A), on-resonance CARS (B), and off-resonance CARS (C) images of a HuH7 cell in absence of MPIOs labels. Greyscale values vary from 3 to 60 in (B) and from 6 to 20 in (C).

bodies can be tracked in time.

4.3.3 Imaging of HuH7 cells incubated with MPIOs

The localization of MPIOs in cells was investigated after incubating the HuH7 cells with a 1 mL solution of iron oxide particles at a concentration of 10^7 particles/mL and 1 mL growth medium. The low concentration ensured that a limited number of particles were taken up by the cells. We note that the use of MPIO solutions with higher concentration imposes no additional complications to the imaging process. Fig. 4.5 (A) shows the on-resonance CARS image of a 30×30 μm^2 region depicting an isolated cell of elongated shape. The outside membrane of the cell is visible, as well as the contour of the nucleus. The image was collected from a focal plane near the center of the cell. The very large, circularly shaped nucleus can be identified by the lack of C-H signal, indicating lipids-rich aggregates are not present. The nucleus region presents uniform signal with intensity comparable to the surrounding aqueous growth medium. As shown previously in Ref. [148], the bright region inside the nucleus can be identified as the nucleolus, containing high densities of proteins and nucleic acids generating intense CARS signals. Several round features with a diameter of ~ 1 μm can be identified inside the cytoplasm. The challenge of our imaging approach is exemplified by this image; are we able to resolve which of the features in Fig. 4.5 (A) are MPIOs and distinguish them from lipid-rich cell components? The CARS response in Fig. 4.5 (B) shows that only one such feature also presents a high intensity also in the off-resonance image of the cell, indicating the presence of an iron oxide particle. All other cellular features appear in the negative-like fashion similar to that in Fig. 4.4 (C); the cell is still visible with negative contrast relative to the water background. In this case also the nucleolus is visible as a dark region in the center of the nucleus.

Visual inspection already reveals that the bright feature in the off-resonance image finds immediate correspondence in the on-resonance image. This observation is confirmed by the colour-coded overlay of the two images presented in

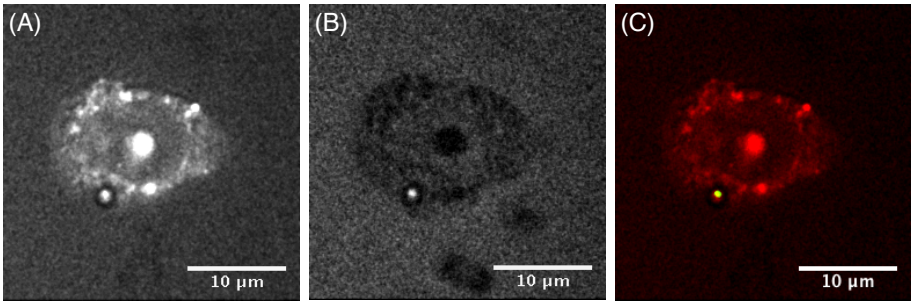

FIGURE 4.5. (A) on-resonance CARS and (B) off resonance CARS images of a HuH7 cell incubated with MPIOs solution. (C) is the overlay of the on- and off-resonance images where the former appears in red, and the background corrected off-resonance response appears in green. Greyscale values vary from 3 to 40 in (A) and from 3 to 25 in (B). The overlay image obtained from on- and off-resonance measurements allows for the identification of a single iron oxide particle in the lower part of the cell (green spot).

Fig. 4.5 (C), where the on- and off-resonance images were added after subtraction of the background in Fig. 4.5 (B), where the background is defined as the average value of the intensity of the signal collected from the medium surrounding the cell. The on-resonance image of the cell appears in red, superimposed with the MPIO signature obtained from the off-resonance image in green. The identification of the particle is here unambiguous despite the many morphologically similar lipid droplets present in the cell, and we have obtained a label-free and non-invasive fast image of the intracellular distribution of MPIOs. The particle has been internalized by the cell, and is located within the cytoplasm in the proximity of the cellular membrane in an axial plane that contains as well the nucleus and the nucleolus located $\sim 2\ \mu m$ above the surface of the glass support.

We can infer, a posteriori, that one feature of the MPIO allows a first-hand identification already in the on-resonance image, as the high intensity spot where the particle is located is surrounded by a dark halo. This effect is due to the large refractive index mismatch between the particle and the surrounding medium, resulting in a distortion of the beams foci that alters the CARS response at the interface [78]. This effect is instead not present in the brightfield images of cells incubated with MPIOs.

4.3.4 THREE-DIMENSIONAL INTRACELLULAR LOCALIZATION OF MPIOS

The optical sectioning capabilities of CARS are best exploited in three-dimensional images of the cell. Such 3D-images allow direct inspection of the spatial distribution of MPIOs within the cells. The brightfield microscopy

image shown in Fig. 4.6 (A) shows a projection of a cell with the nucleus located to the left and a collection of circular features are visible to the right in the cell, some of them presenting a diameter in the order of 1 μm. Again, it is not straightforward to distinguish MPIOs from lipid bodies in the image and from the optical image no information is available on the vertical position of the different structures relative to the upper and lower boundaries of the cell. In fact, inspection of Fig. 4.6 (A) does not allow one to conclude that particles have been internalized by the cell, rather than being located at the outside of the membrane. Fig. 4.6 (B-F) is a sequence of overlays of on-resonance (red) and off-resonance (green) CARS images of the cell taken at descending vertical positions separated by 1 μm. The full outline of the cell can be observed. In Fig. 4.6 (F) the interface between the cell and the underlying glass support is imaged. From Fig. 4.6 (C-D) we conclude that the nucleus as well as the collection of lipid droplets on the right side of the cell are both located in the mid-sections of the cell. The colocalization with the non-resonant image also allows the identification of the volume distribution of MPIOs, which is particularly important in order to determine whether the internalization process has been successful. Two particles can be observed, the leftmost of which located in the upper region of the cell (see Fig. 4.6 (B-D)) and the rightmost in the lower region of the cell closer to the glass substrate (see Fig. 4.6 (C-E)). Hence, from this three-dimensional CARS image we can conclude with certainty that two particles have been successfully internalized, appearing with a maximum signal at locations 2 μm (lower right particle, Fig. 4.6 (D)) and 3 μm (upper left particle, Fig. 4.6 (C)) above the glass support. The signature of the particles clearly extends beyond their physical dimensions, as the axial resolution is larger ($\sim$ 1 μm) than the lateral resolution ($\sim$ 300 nm). The slight discrepancy between the location of the MPIOs in the on- and off-resonance images is most likely due to a slight relocation of the particles between the two measurement series. We can rule out the possibility that the change in position is due to optical tweezing by noting that this effect is not present in the combination of single layer images where the time interval between consecutive measurements is shorter. The set of on/off resonance CARS images provides unambiguous insight into the presence and three dimensional distribution of single MPIOs, granting access to information that is otherwise impossible to obtain from the brightfield image in Fig. 4.6 (A).

These results demonstrate that CARS microscopy enables objective verification of the particle uptake in living cells. This is of particular interest, since the particles and lipid droplets present similar morphology under brightfield microscopy, making the evaluation of their uptake dependent on the experience of the investigator. Moreover, the access to the exact intracellular localization of incorporated particles enables investigations of the interactions between particles and cell organelles, paving the way for long-term toxicity studies of importance from a clinical perspective.

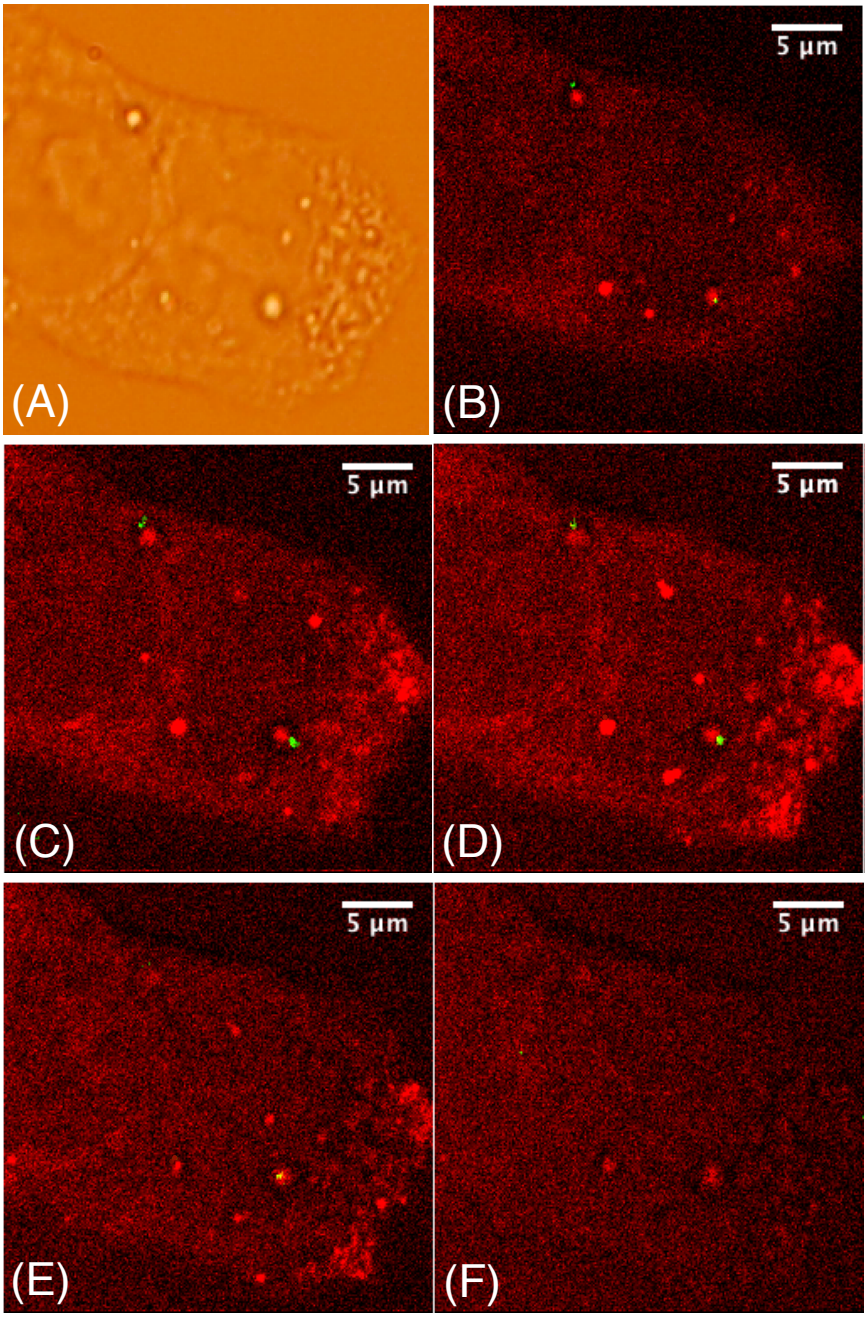

FIGURE 4.6. (A) Brightfield microscopy image of a HuH7 cell incubated with MPIOs. (B-F) Overlay of on-resonance (red) and off-resonance (green) CARS images of the same cell with descending axial position (separated by 1 μm). Two internalized iron oxide particles (green) can be idetified from the overlay images.

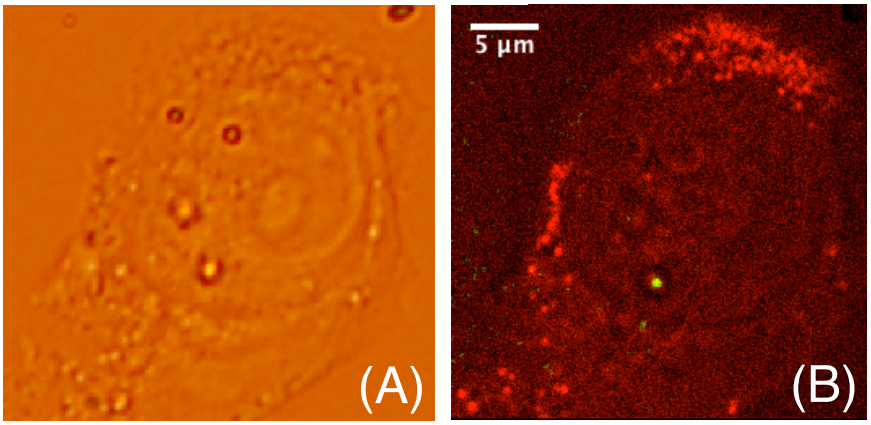

Figure 4.7. (A) Brightfield microscopy image of a HuH7 cell incubated with MPIOs. (B) Overlay of on-resonance (red) and off-resonance (green) CARS images of the same cell. One MPIO (green) appears to be located within the nucleus of the cell.

4.3.5 Outlook: nuclei penetration

One interesting feature of MPIOs labels and of functionalized particles used for cell penetration is their capability to penetrate nuclei. Engineering particles capable of penetrating the nuclei is challenging due to the lack in our knowledge of the different factors that regulate uptake in cell nuclei and the concomitant difficulty in formulating effective functional agents. Although the streptavidin functionalization used here was not designed specifically for transport into the nucleus, evidence of nuclear penetration was found in about 10 % of the cells imaged with the on-/off-resonance CARS approach.

Fig. 4.7 (A) shows the brightfield microscopy image of a HuH7 cell incubated with MPIOs. The nucleus of the cell is visible, although the identification of the edges is not straightforward. A large number of round intracellular features are also visible, several of them accumulating in the perinucleic region. Inside and close to the nucleus four large features are visible, potentially related to the presence of MPIOs. Fig. 4.7 (B) shows the overlay of the on-resonance (red) and off-resonance (green) CARS images of the same cell. Here the shape of the nucleus appears more clear and seems to occupy the majority of the volume of the cell. One single MPIO is visible in a location that appears to be inside the nucleus. The quality of this image is not sufficient to unambiguously claim that the MPIO has penetrated the nucleus, although it provides strong evidence that this could be the case. Additional measurements are required to confirm this result, especially volume views of other cells. This unexpected result is an encouraging example of the possibility of visualizing MPIOs with nuclei penetration capabilities with CARS, and certainly warrants follow up experiments.

4.4 CONCLUSIONS

We have shown that CARS microscopy is a suitable tool for intracellular visualization of micrometer-sized iron oxide particles and has the potential to become an important instrument for the development of tracers for cell tracking in clinical MRI. Compared to other techniques available for this purpose, CARS has the advantage of being a label-free non-invasive technique that gives sufficient contrast both for the visualization of the particles and the cellular environment without need of additional labels. As magnetite is a small bandgap semiconductor, the four-wave mixing response of the particle does not benefit from additional enhancement of two-photon electronic excitation when the excitation beams are tuned to match the lipid CH stretches used for achieving contrast from the cellular body, hence the particles are not unambiguously identifiable from the on-resonance image of the cell alone. However, as non-resonant CARS is almost frequency-invariant, MPIOs are easily distinguished in the off-resonance image of the system. Overlays of the on- and off-resonant measurements enable the visualization of the position of the particles in the cells with sub-micron accuracy. The immediate advantages of the use of CARS for this task are the chemical specificity that allows us to distinguish unambiguously the MPIOs from intracellular lipid-bodies of comparable dimensions, as well as the intrinsic three-dimensional imaging capabilities that allows us to identify the axial position of the particles in the cell with high precision. The issues that CARS microscopy is capable of addressing are fundamental questions that naturally arise in the development stages of engineered particles, where physical properties of the particles are modified and additional surface functionalizations are added, modifying the interaction between the particles and the cell at the molecular level. Besides quantitative assessment of the efficacy of the internalization, additional information on the exact intracellular position of the MPIOs in comparison with other cell components are readily available in three-dimensions. It is easy to imagine scenarios where this information is particularly relevant if, *e.g.* nucleus penetration is desirable. Preliminary results suggest that nuclear penetration is already taking place for the MPIOs used in this work, although the streptavidin functionalization was not specifically designed for this aim. Further measurements are required to confirm this claim. As an important outlook, we note that the CARS approach allows for following the kinetics of the particle uptake in real-time. Moreover, other subcellular components can be selectively visualized in CARS by probing molecular vibrations characteristic for *e.g.* mitochondria or nucleic acids [152], allowing the co-localization of the particles with other cell components with high specificity and without labeling. Also, CARS measurements can readily be combined with two-photon fluorescence (2PF) on most CARS setups. Hence, using markers for specific internalization processes and combining CARS and 2PF, information on the process responsible for the uptake of the particles can be obtained.

4.5 Appendix: THG visualization of MPIOs

Parallel to the combination of on- and off-resonance CARS outlined in section 4.3.1, another approach for the visualization of MPIOs was tested using Third Harmonic Generation (THG). THG is a non linear effect taking place when three photons from the excitation beam interact with the material, causing the emission of a fourth photon presenting three times the frequency of the incoming photons. Due to the symmetry of the interaction, when the medium at the focal point is homogeneous, the generated signal before and after the focal point interfere destructively, and the net THG response is zero. When instead inhomogeneities are present at the focal point, such as an interface between two different media, the third harmonic response becomes very strong [188]. THG microscopy can hence be used to obtain high resolution images of systems presenting sharp interfaces, as the case of visualizing MPIOs in cells [207]. THG can be easily implemented on a CARS setup as the two techniques share one of the excitation beams. We employed the 1064 nm pump beam to excite the third harmonic, while the other beam was kept blocked. The signal was detected around 350 nm after spectral filtering to avoid contaminations from direct illumination and other high order effects..

A droplet of solution containing 10^8 particles/mL of MPIOs was left to dry for one hour on a conventional microscope cover slip before imaging with THG. Fig. 4.8 (A) shows the brightfield microscopy image of a 20×20 μm region of the sample. Here, despite the poor resolution of the technique at this magnification, several MPIOs are visible as the round objects with a slight red dominance. Fig. 4.8 (B-L) shows the THG images obtained from eleven consecutive vertical positions of the same area, separated of 0.3 μm. Three round features corresponding to MPIOs are clearly visible in most of the layers, with maximum contrast in images F-H.

THG provides very clear images with high signal to background ratio of the particles. The axial resolution can be determined indirectly from Fig. 4.8, considering that each of the particles is visible with clarity in eight vertical layers, hence over a distance of 2.1 μm, compared to the physical size of the particles of ~ 1.2 μm. The resolution is clearly better in plane, as shown in Fig. 4.9 (A) where the profile intensity of the signal across the diameter of one of the particles (see panel) is displayed. Compared to the intensity profile of the CARS signal (Fig. 4.3), the THG signal presents steeper edges extending over ~ 0.5 μm and a central plateau of ~ 1 μm in length. Fig. 4.9 (B) presents a three dimensional rendering of the particles, reconstructed from the images in Fig. 4.8. The particles present a slightly elongated shape as originated by the different resolution in the planar and axial directions.

The visualization of the MPIOs with THG hence results very clear and provides unambiguous identification of the particles. Regretfully, this technique turns out to be inefficient for the visualization of MPIOs in living cells. When measuring the THG signal from the cells incubated with MPIOs, the signal collected in the background from the biomaterial becomes non negligible preventing the discrimination of the particles from their environment. This strong

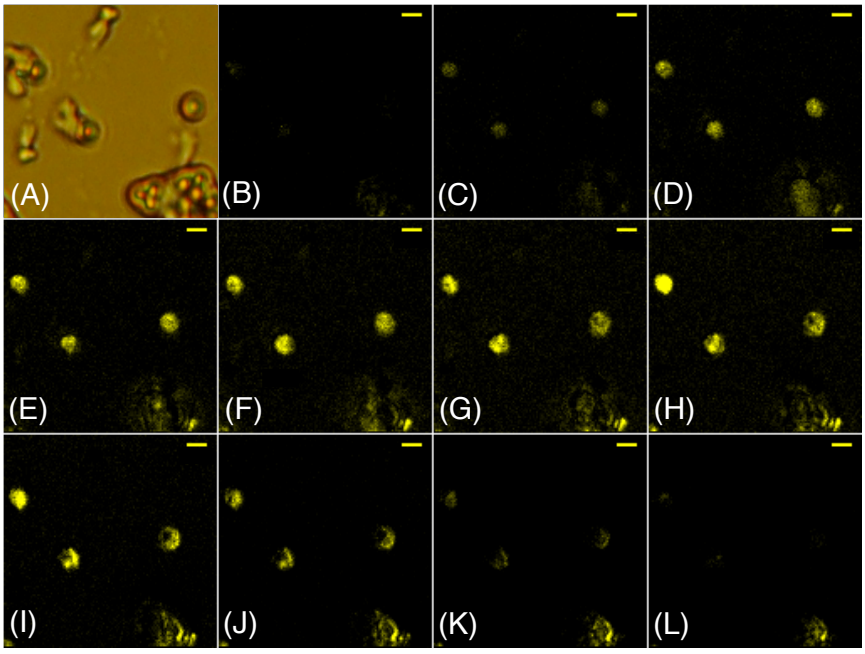

FIGURE 4.8. (A) 20×20 μm brightfield microscopy image of dried solution of MPIOs. (B-L) THG microscopy images of the corresponding area. The images refer to vertical planes separated by 0.3 μm. Scale bar 2 μm. Three MPIOs clearly appear in the THG images, with maximum contrast in layers F-H.

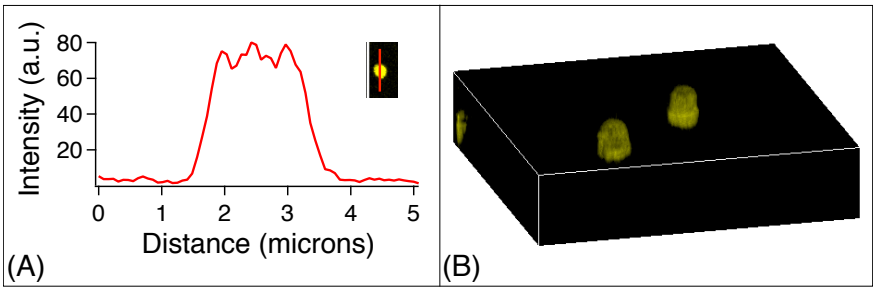

FIGURE 4.9. (A) Intensity profile of the THG signal along the red line drawn in the top right panel across the diameter of one of the MPIOs. The profile is compatible with the response expected from a particle with 1.2 μm lateral dimension. (B) three dimensional rendering of the THG response of the MPIOs. The image is reconstructed from the layers in figure Fig. 4.8.

and inhomogeneous background signal arises from the sharp interfaces between the different cell components, which are characterized by media with different composition [212].

In conclusion, THG microscopy is a suitable technique for the visualization of MPIOs, although it becomes inefficient for their localization in cells in vivo, due to the high background response produced by the cells.

5 Uptake of gold nanoparticles in living cells

Understanding the mechanism underlying the interactions between inorganic nanostructures and biological systems is crucial for several rapidly growing fields that rely on nano-bio interactions. In particular, the further development of cell-targeted drug delivery using metallic nanoparticles (NP) requires new tools for understanding the mechanisms triggered by the contact of NPs with membranes in different cells at the sub-cellular level. Here we present a novel concept of multi-modal microscopy, enabling three-dimensional imaging of the distribution of gold NPs in living, unlabeled cells. Our approach combines Multi-photon Induced Luminescence (MIL) with Coherent Anti-Stokes Raman Scattering (CARS) microscopy. Comparison with transmission electron microscopy (TEM) reveals *in vivo* sensitivity down to the single nanostructure. By monitoring the incorporation of NPs in healthy human epidermal keratinocytes and Squamous Carcinoma Cells (SCC), we address the feasibility of non-invasive delivery of NPs for therapeutic purposes. While neutralizing PEG-coating was confirmed to prevent NP integration in SCCs, an unexpectedly efficient integration of NPs into keratinocytes was observed. These results, independently validated using TEM, demonstrate the need for advanced surface modification protocols to obtain tumor selectivity for NP delivery. The CARS/MIL microscopy platform presented here is thus a promising tool for non-invasive study of the interaction between NPs and cells.

5.1 Introduction

Gold nanoparticles (AuNPs) have recently emerged as a compelling alternative for cell-targeted therapeutic delivery [81] and diagnosis [104]. In contrast to polymer and liposome-based vehicles, AuNPs can inherently be tracked using microscopy techniques without the involvement of bulky reporter molecules. Contrary to fluorophores, they emit a stable and intense optical photoluminescence signal without photo-bleaching or blinking effects. Moreover, the photoluminescence can be significantly enhanced through the coupling to localized surface plasmon modes of the AuNPs [65]. In addition, AuNPs are

biologically non-toxic [38], as opposed to *e.g.* carbon nanotubes [42] and quantum dots [94], which generally contain heavy metals. The near atomic-scale specificity with which AuNPs can be manufactured enables fine-tuning of their size and shape [32] for efficient integration into cells, further supported by tailored surface properties by attaching antibodies, peptides, oligonucleotides, oligosaccharides, and lipids [33, 85, 116, 122, 133, 157, 167, 183, 203]. By further functionalizing these constructs with enzymes [82], drugs, and transcription-regulating biomolecules (for recent reviews, see [81, 86]), AuNPs can serve as vehicles for cell-specific therapeutics, with the advantages of highly localized and controlled release of the active component along with reduced systemic dosing. Within this context, special attention has been given to selective targeting of tumor cells [55,61,63] and functionalization of AuNPs with anti-cancer drugs [2, 6, 22, 27, 84, 154, 158] for cancer treatment.

These application-oriented studies imply that functionalized AuNPs will enable important contributions to modern health care. In order to exploit the full potential of AuNPs, extensive efforts are now being invested to establish a fundamental understanding of the general mechanisms behind their transmembrane transport, cytoplasmic trafficking and intracellular processing. Present knowledge relies primarily on observations made by Transmission Electron Microscopy (TEM), frequently supported by Inductively Coupled Plasma Atomic Emission Spectroscopy (ICP-AES) [32]. While the latter technique provides the average AuNP population uptake at a given time without information on the intracellular localization, TEM has the ability to resolve both AuNPs and cellular features in the nanometer range. Although TEM therefore has contributed significantly to our understanding of AuNP-cell interaction, some significant limitations may be noted: the sample preparation procedure involving cell fixation, metal deposition, resin embedding and slicing of the cell is time-consuming and highly invasive, and has been previously associated with potential artefacts [180]. In addition, TEM measurements are performed on thin subsections of the cell (typically 80 nm in thickness), granting the technique high axial resolution with the downside that a study of the entire volume of a single cell requires the measurement of a large number of subsections.

An alternative strategy is to use optical microscopy. By coupling a fluorescent reporter molecule to the NPs, their uptake in living cells has been followed by fluorescence [189] and Raman [171] microscopy. However, some drawbacks of this approach may be noted: firstly, considering the decisive role of NP surface chemistry for the interaction process, it is not completely evident that the marker is not affecting the uptake process. Secondly, the risk exists that the reporter molecules decouple from the NPs throughout the integration process, and that an erroneous picture of the incorporation is obtained. In addition, long-term studies are not possible since fluorophores bleach, get quenched and induce phototoxic reactions.

In the light of these considerations, label-free imaging utilizing the intrinsic optical properties of AuNPs appears as an attractive alternative. For instance, their strong light diffraction renders AuNPs visible in dark-field microscopy [44,208], though merely as a two-dimensional projection and unrelated

to the cell morphology since no contrast is given by the low-diffractive cellular features. Thus, no true nanobio correlation can here be achieved. AuNPs are also intrinsically photoluminescent upon laser irradiation [209], though in general too weak for live cell imaging. By instead exciting the AuNPs through a multiphoton process using NIR light, the photoluminescence efficiency is significantly enhanced for particles in a broad dimensional range due to the coupling to the localized surface plasmon modes [8, 69]. Multi-photon Induced Luminescence (MIL) has indeed successfully been exploited for the visualization of gold nanorods in A431 skin cancer cells [60], generating a signal more than 4000 times brighter than that from intrinsic fluorophores, and of gold nanoparticles in endothelial cells [58]. However, again only the AuNPs were visualized, without being related to the biological context and limited to subsections of the cells. Incidentally, the laser sources required for exciting MIL are similar to the ones used in CARS, whose capabilities for the label-free visualization of live cells [76] have been previously discussed in this thesis.

By combining MIL and CARS, we are able to visualize the full three-dimensional distribution of AuNPs simultaneously within their cellular environment without any labelling. With the use of the NIR laser light used to generate CARS, the multi-photon luminescence process is simultaneously induced in the AuNPs, forming corresponding three-dimensional images of their distribution which can be colocalized with the lipid-rich cell membranes and organelles visualized in the CARS volume images. The combination of MIL and CARS is in principle a suitable mean for the visualization in cells of other plasmonic particles that exhibit large luminescence response, *e.g.* silver nanoparticles [111].

As a first important application, we study the integration and distribution of polyethylene glycol (PEG)-coated AuNPs in human Squamous Carcinoma Cells (SCC) (A431 skin cancer cell line) and healthy keratinocytes in order to address the feasibility of transdermal delivery of AuNP therapeutic and diagnostic agents in particular for cancer treatment, as only limited studies entail a comparison between tumor cells and normal cells. The observations reported here were confirmed with high-resolution TEM.

5.2 Materials and methods

5.2.1 Preparation of AuNPs

60-nm colloidal gold particles (BB International, Cardiff, UK) were coated with a monolayer of thiol-conjugated PEG, SH-PEG (MW 5000 g mol^{-1}, Sigma, St. Louis, MO), known to reduce nonspecific cell integration and to prevent AuNP aggregation. The commercial colloidal solution of AuNPs was centrifuged and the supernatant was removed. An aliquot of 1 ml of 0.15 μg/mL SH-PEG dissolved in Milli-Q water was added to the particle pellet and left to incubate over night for monolayer formation. After incubation, the colloidal solution was centrifuged and the supernatant was removed and replaced with $\sim$ 1 ml fresh Milli-Q water. The extinction coefficient of the PEG-coated AuNPs was

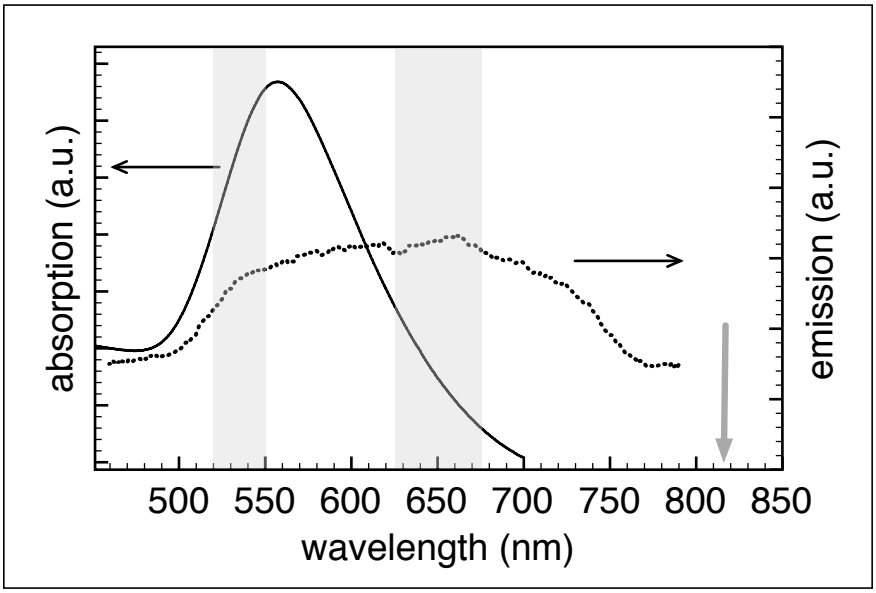

FIGURE 5.1. Absorption (filled line) and emission (dashed) spectra of a water solution of PEG-coated, 60 nm-sized AuNPs. While the maximum can be found at 560 nm, the light absorption is still significant in the multiphoton excitation region. The multiphoton induced photoluminescence emitted following excitation at 817 nm (grey arrow) shows a broad spectral character. The grey areas indicate the spectral regions used for MIL detection.

measured in a Cary 5000 UV-VIS spectrophotometer. The absorption maximum was centered at approximately 555 nm, with a full width at half maximum (FWHM) of $\sim$ 100 nm (Fig. 5.1). The corresponding emission spectrum, excited by the OPO output at 817 nm, was measured by a fiber-based spectrometer (AvaSpec 2048, Avantes, Eerbeek, The Netherlands) coupled to the microscope, resulting in a broad photoluminescence continuum ranging between 500 and 760 nm (Fig. 5.1), spectrally limited by collection optics and filters.

5.2.2 CELLS PREPARATION

Normal human epidermal keratinocytes (HEKs, Cascade Biologics, Portland, OR) were maintained in phenol red-free EpiLife keratinocyte medium (Cascade Biologics, Portland, OR) supplemented with 60 $/muM$ $CaCl_2$, gentamicin/amphotericin and 1% (v/v) human keratinocyte growth supplement (HKGS; Cascade Biologics) at 37^{o}C and in a 5% CO_2 incubator. Final concentrations of the components in the supplemented medium were: bovine pituitary extract, 0.2% v/v; bovine insulin, 5 mg/mL; hydrocortisone, 0.18 mg/mL; bovine transferrin, 5 mg/mL; human epidermal growth factor, 0.2 ng/mL; gentamicin, 10 μg/mL and amphotericin B, 0.25 μg/mL. The keratinocytes were

used for experiments in the fifth or sixth passage. Human squamous carcinoma cells (A431, HPA cultures, Salisbury, UK) were maintained in phenol red-free Eagless Minimum Essential Medium (EMEM, Invitrogen, Pailsey, UK), supplemented with 10% fetal bovine serum, 2 mM glutamine EMEM, 1% Non-Essential Amino Acids (NEAA) at 37^{o}C and in a 5% CO_2 incubator. Both cell lines were seeded on 35 mm diameter glass bottom dishes (P35G-1.5-14-C; MatTek, Ashland, MA, USA) at a density of 1 x 10^3 cells/cm^2. After three days, cells were incubated in growth medium with 10% (v/v) solution containing PEG-coated 60 nm gold nanoparticles (2.6×10^{10} particles/ml, corresponding to 43.1 pM) for 2, 6, and 10 hours, respectively. For the CARS/MIL microscopy, the incubation medium was removed, after which the cell layer was washed two times with 1 mL HEPES imaging buffer (140 mM NaCl, 20 mM HEPES, 5 mM KCl, 1mM $MgCl_2$, 0.06 mM $CaCl_2$, 10 mM D-Glucose) and then immersed in 2 mL imaging buffer. For TEM, the incubation medium was instead replaced overnight with a mixture of 2% paraformaldehyde, 2.5% glutaraldehyde, and 0.02% sodium azide in 0.05 M sodium cacodylate buffer, pH 7.2. Postfixation was performed for 2 h at 4^{o}C with 1% osmium tetroxide and 1% potassium ferrocyanate in 0.1 M cacodylate. After rinsing, the specimens were treated for 1 h with 0.5% uranyl acetate in water. Dehydration was performed in a graded series of ethanol followed by acetone and epoxy resin (Agar 100; Agar Scientific, Stansted, UK) infiltration. The plastic was cured by heat. After removal of the embedded cultures from the culture dishes, ultrathin sectioning was performed with a Leica EM UC7 ultramicrotome (Leica Microsystems, Vienna, Austria), parallel with and perpendicular to the culture surface. Diamond knives were used at a section thickness setting of 60 nm.

5.2.3 MIL microscopy

MIL microscopy is implemented on the setup used for CARS experiments described in part 3.1 of this thesis. In the same experimental configuration, *i.e.* on the same sample, in the same region within the sample, the MIL signal from the AuNPs was obtained by single-beam excitation using the OPO output (817 nm). In these experiments, the 1064 nm beam was blocked in order to exclude any contributions from CARS-generating objects. Following multi-photon absorption, the AuNPs emitted a photoluminescence detected in epi geometry (see Fig. 3.1 (B)). Its broadband character in the wavelength region characteristic for 60 nm sized AuNPs was ascertained by a dual-channel detection arrangement, consisting of two sets of bandpass filters (535/25 nm and 650/50 nm, Chroma Technologies, USA), each in front of a single-photon counting PMT connected to the SPCM-unit. By time-gating, the impact of autofluorescence from the biological environment on the instantaneous photoluminescence could be minimized. Three-dimensional imaging was achieved by scanning a sequence of horizontal planes at different vertical positions by translating the objective with a motorized stage. Rapidly switching between CARS and MIL microscopy mode was achieved by simply selecting appropriate combinations of excitation beams as illustrated in Fig. 3.1 (B), assuring that the CARS and MIL im-

ages were collected from the same region. In a future development, this can be achieved at single-pulse level by an acousto-optical pulse-selection unit, enabling simultaneously recorded CARS and MIL images. Samples were first imaged in brightfield white-light microscopy, and the areas of interest, typically covering $60 \times 60\ \mu m^2$ (256×256 pixels), were then imaged at different vertical positions with 1 micron spacing by CARS and MIL microscopy. The total acquisition time for each layer was 20 s for each of the techniques.

5.3 Results

5.3.1 CARS/MIL imaging of AuNPs in cells

To first establish the capability of combining CARS and MIL, a series of images of A431 squamous carcinoma cells (SCCs) incubated with AuNPs for six hours was collected. Fig. 5.2 (A) shows the forward-emitted CARS signal collected at the CH-stretch vibration at 2845 cm^{-1} obtained from a cluster of SCCs. As shown by the figure, CARS microscopy visualizes lipid-rich biological structures such as cell membranes and lipid-rich intracellular components, which here appear as high intensity regions in the cell cluster. The CARS images thereby provide the biological frame of reference for the nanobio interaction, so that the relative location of NPs within cells can be determined with the use of MIL. The corresponding photoluminescence images, shown in Fig. 5.2 (B) and (C), were recorded from the same sample by the dual-detector arrangement at 535/25 nm and 650/50 nm. Two features with lateral dimensions smaller than 1 μm located at the same positions in the sample can be observed in both the 535 nm and 650 nm images. This confirms that the emission from the features are of broad spectral character in a wavelength region typical for the photoluminescence of 60 nm sized AuNPs supported by the spectrum in Fig. 5.1. Time-resolved measurements further confirmed the photoluminescent origin of the emission from the two features in the MIL images. Fitting the time decay shown in Fig. 5.2 (D) with a single exponential function results in an ultrashort decay time shorter than 200 ps, characteristic for photoluminescence of gold nanostructures [199, 213]. The location of the AuNPs within the cells could be determined with high accuracy by overlaying the two images. Isolated AuNPs were represented as spots of average size of $\sim$ 300 nm in the x-y plane and $\sim 1\ \mu m$ in depth, which represents the point spread function of MIL. The resolution of CARS microscopy is reported to be comparable by others [28].

In order to investigate the sensitivity with which AuNPs can be visualized, a comparison was made with TEM images of the corresponding cellular system; SCCs incubated for six hours. A 60-nm thick vertical cut of the SCCs revealed individual AuNPs embedded in multivesicular compartments of the average size $\sim$ 300 nm, located in the vicinity of the nucleus, as exemplified in Fig. 5.3 (A). A high-resolution TEM image, as exemplified in Fig. 5.3 (B), further reveals the multivesicular nature of the compartment, suggesting that the AuNPs are mainly in the later stage of the endosomal degradation pathway [4] after six

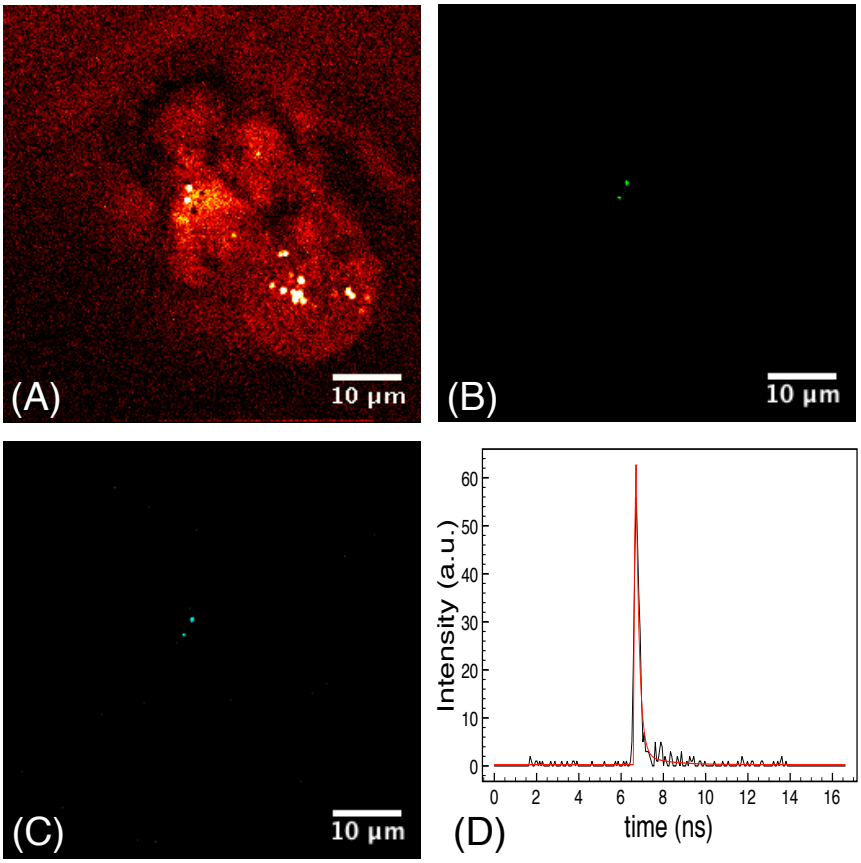

FIGURE 5.2. A set of CARS and MIL microscopy images of squamous carcinoma cells incubated with PEG-coated AuNPs for six hours. Images are a subset of three stacks, each covering a total volume of $60 \times 60 \times 30$ μm^3 ($256 \times 256 \times 30$ pixels) forming tomographic images of the cells and the distribution of the AuNPs. (A) The forward-emitted CARS signal collected at the CH-vibration 2845 cm^{-1}, visualizing organelles with high lipid content. (B-C) The epi-detected MIL signals collected in spectral regions around (B) 535 nm and (C) 650 nm at corresponding vertical position. (D) The time decay of the MIL signal collected at the location of one of the bright spots in the 535 nm MIL image, proving the short life time characteristic of photoluminescence and the limited contribution from fluorescence.

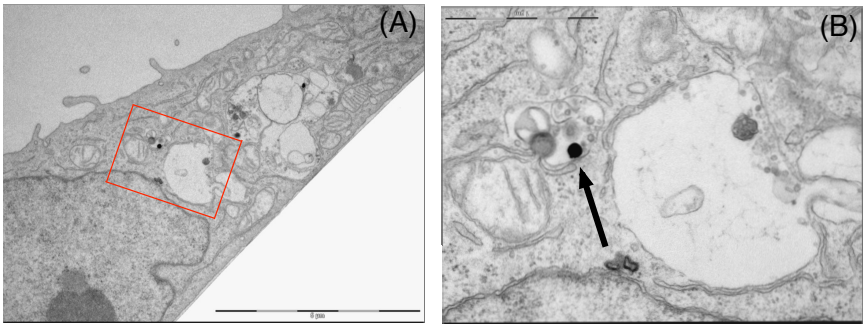

FIGURE 5.3. (a) TEM image of a vertical cut of a squamous carcinoma cell incubated with PEG-coated AuNPs for six hours. Scale bar 5 microns. (b) Enlargement of a perinucleic area containing a single AuNP in a multivesicular endosome. Scale bar 1 micron.

hours of incubation. No formation of AuNP clusters was observed in SCC slices, confirming that the features visualized in the MIL images indeed represent individual AuNPs.

5.3.2 UPTAKE IN SQUAMOUS CARCINOMA CELLS

The kinetics of the AuNP integration process were investigated by collecting CARS/MIL and TEM images after the incubation at two, six and ten hours, respectively. The full series of events for the SCCs is depicted in the overlay CARS/MIL images in Fig. 5.4, including corresponding orthogonal side views reconstructed from the stacks ($60 \times 60 \times 20$ μm^3 for Fig. 5.4 (A) and (B), $60 \times 60 \times 30$ μm^3 for Fig. 5.4 (C)). The images confirm the low uptake of AuNPs indicated in Fig. 5.3, both at shorter (two hours) and longer (ten hours) incubation times. Independent of the incubation time, two populations can be identified; the AuNPs are either localized at the cell membrane or in endosomes in the perinucleic region of the cell. In Fig. 5.4 (A) (two hours) a single AuNP can be observed in the horizontal plane (x-y projection) at the top of the image as well as in the side y-z projection localized in the vicinity of the outer cellular membrane, whereas the side x-z projection also show a AuNP in the perinucleic region. After two hours of incubation, three out of six of the SCCs that were investigated contained no AuNPs, and the other three contained either one or two AuNPs. Two to three AuNPs are visible in each of the projections in Fig. 5.4 (B) (six hours), again localized either at the cell membrane or in the cytoplasm, preferentially close to the nucleus. After six hours of incubation, two or three NP signatures were observed in four out of six cells. Finally, in Fig. 5.4 (C) (ten hours) one AuNP is visible in each of the projections, localized in the proximity to the nucleus. Here, between three and seven intracellular AuNPs could be observed in the SCCs investigated, From the entire set of CARS/MIL images of SCCs, it is evident that the number of isolated MIL emitters representing

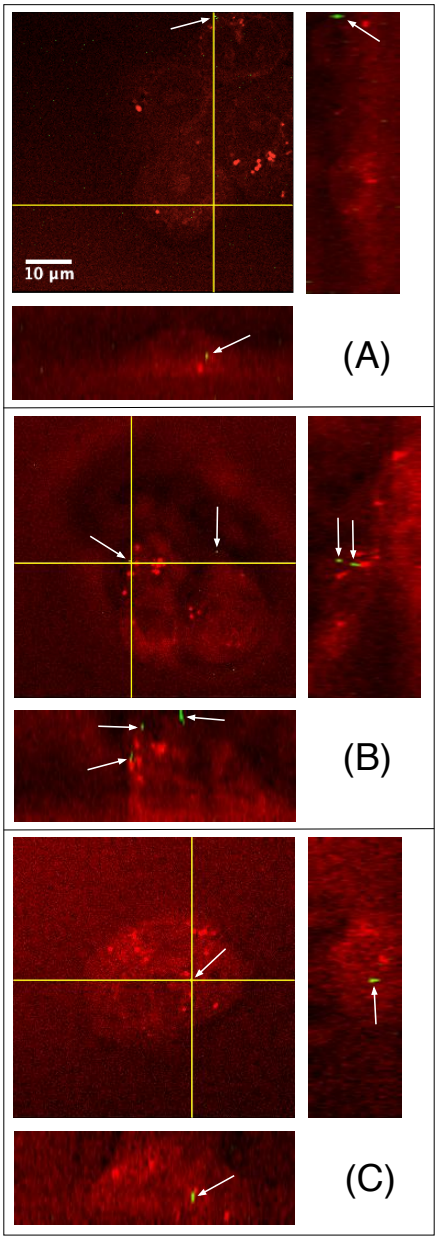

FIGURE 5.4. Overlay CARS (red) and MIL (green) images of SCCs with corresponding orthogonal side views collected after (A) 2 hours (B) 6 hours and (C) 10 hours incubation with PEG-coated AuNPs, respectively. The lines in the front views indicate the position of the orthogonal projections. Two isolated MIL signals attributed to luminescence from AuNPs can be distinguished in the cells in (A) after 2 hours of incubation, four in the cells in (B) and one intracellular spot in (C) after 10 hours of incubation, indicated by arrows.

AuNPs increases slightly with the incubation time, but remains in a range between one and seven. This figure includes the particles that were visible close to the outer cell membrane, thus, probably still membrane bound rather than internalized. The limited, and unspecific uptake of PEG-coated AuNPs was confirmed by TEM for all incubation times; careful inspection of all 60 nm thin slices (72 slices in total) revealed NPs in a single cell, here enclosed in multivesicular perinucleic 300 nm-sized endosomes. No particles were observed in the nucleus, irrespective of microscopy technique used.

5.3.3 Uptake in healthy epidermal keratinocytes

The interaction of the PEG-coated AuNPs with the human epidermal keratinocytes was found to be of a significantly different character, as illustrated by the CARS/MIL projections (horizontal planes and corresponding orthogonal side views) in Fig. 5.5. The corresponding TEM images confirm this scenario. As opposed to SCCs, NPs were readily located in the keratinocytes and observed in a majority of the 72 slices. Given the generally low probability to find NPs in such thin slices (60 nm), this observation indicates a significant uptake capability of the keratinocytes. In order to ascertain that the difference is not due to differences in PEG-coating, experiments were performed in duplicates. Already following 2 hours incubation, a few AuNPs (maximum six features per cell in a total of five cells) were observed in the CARS/MIL images of the keratinocytes (Fig. 5.5 (A)), primarily located in the vicinity of the cell membrane. The corresponding TEM images confirm this as exemplified in Fig. 5.5 (D); a single AuNP (see arrow) can be observed close to the cellular membrane. After an incubation time of 6h (Fig. 5.5 (B)), several tens of luminescent features with sub-micron lateral dimensions were found to be present inside the cell for all six cells investigated. The AuNPs were evenly distributed throughout the cytoplasmatic area, though without entering the nucleus. TEM images of corresponding cells (Fig. 5.5 (E)) confirm the presence of multiple isolated AuNPs internalized in endosomes of sizes varying between 300-800 nm distributed in the cytoplasm. CARS/MIL images of the keratinocytes incubated for 10 hours (Fig. 5.5 (C)) show a high density of AuNPs, especially in the perinucleic region. Even micrometer-sized clusters can be observed in the cytoplasm, characterized by an average count per pixel of approximately three times that recorded from the spots identified as single AuNPs. In this case MIL features have dimensions much larger than the diffraction limit, preventing an average quantification. The same behavior was found in all three cells investigated. The corresponding TEM images partly confirm this picture (Fig. 5.5 (F)): a large number of isolated AuNPs but also clusters of metallic structures can be found enclosed in single multivesicular entities close to the nucleus. However, these clusters were all of sub-micron size, *i.e.* smaller than observed in the MIL images. In Fig. 5.6, the full potential of CARS and MIL microscopy is illustrated by volume images of a HEK cell after six hours of incubation, obtained from the three-dimensional rendering of the cell. The three-dimensional distribution of AuNPs in the entire cell volume can be assessed, providing integrated information on density variations

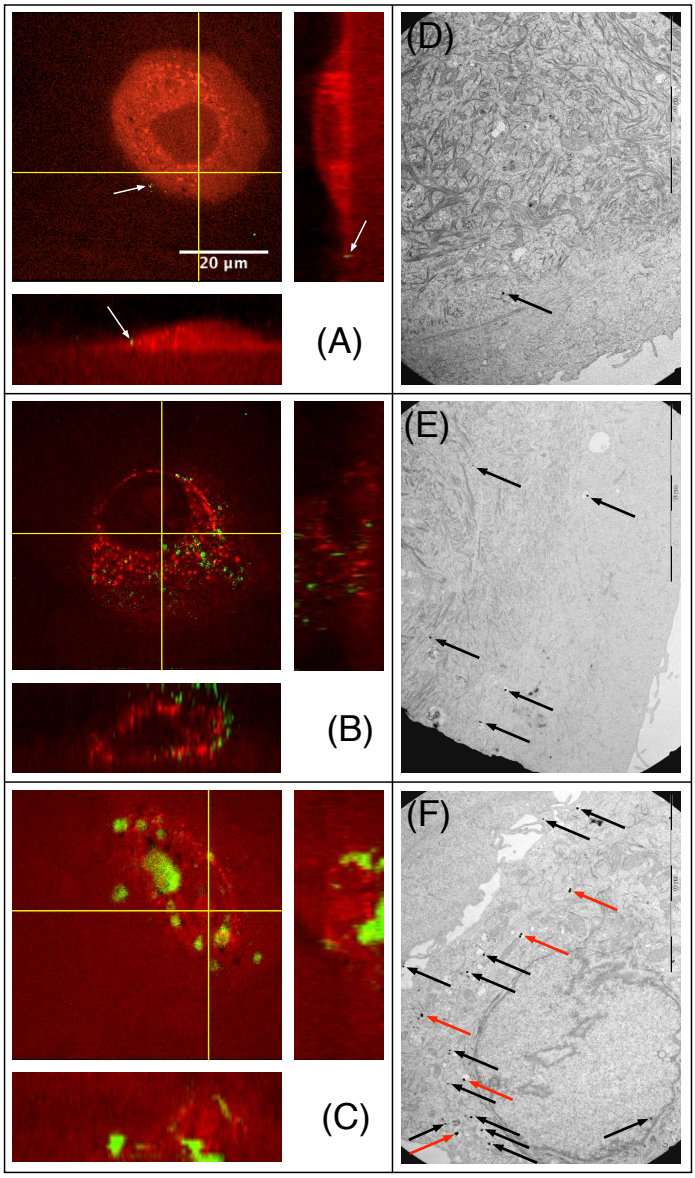

FIGURE 5.5. Overlay CARS (red) and MIL (green) images of human epithelial keratinocytes with corresponding orthogonal side views collected after (A) 2 hours (B) 6 hours and (C) 10 hours incubation with PEG-coated AuNPs, respectively. Three isolated MIL signals attributed to luminescence from AuNPs can be distinguished at the cell membrane in (A) after 2 hours of incubation (white arrows), multiple intracellular AuNPs in (B) after 6 hours and clusters of AuNPs in (C) after 10 hours (discussed in the text). (D-F) TEM images of cells incubated corresponding times (scale bar 5 microns). Black arrows indicate individual AuNPs. In (F), clusters of AuNPs can also be observed (red arrows).

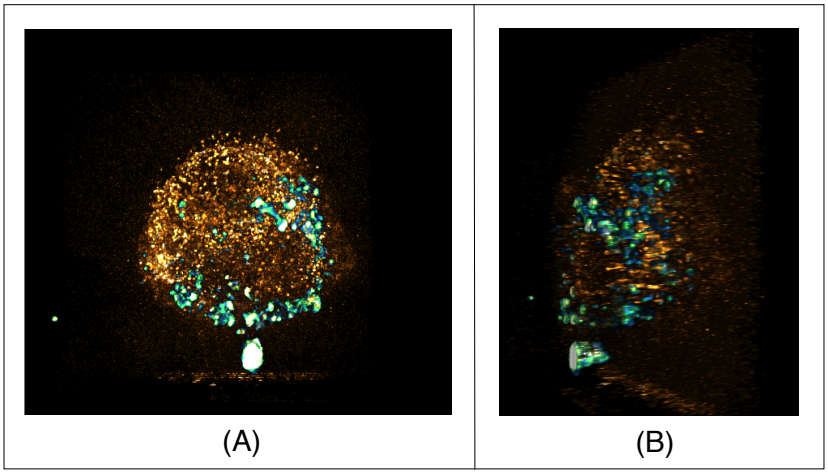

FIGURE 5.6. Three-dimensional CARS/MIL overlay images of HEK incubated with PEG- coated AuNPs for 6 hours. The images cover a volume of $60 \times 60 \times 20\ \mu m^3$.

throughout the cytoplasm and in the vicinity of important organelles, information difficult to retrieve by TEM. These tomographic CARS/MIL images show the high density of AuNPs evenly distributed throughout the cytoplasm of the keratinocytes.

5.4 DISCUSSION

The selectivity of the MIL-microscopy towards AuNPs is confirmed by the collection of two spectrally separated signals at 535 nm (bandwidth 25 nm) and 650 nm (bandwidth 50 nm), which show correlated response as expected from the broadband AuNP photoluminescence. In practice, no noteworthy differences were observed in any of the sets of MIL images in the two spectral regions selected for the collection, confirming the negligible contribution from fluorescent biologic components. This is expected, considering that autofluorescence originating from *e.g.* flavins, porphyrins and NAD(P)H is typically detected at wavelengths below 500 nm with a bandwidth of $\sim$ 50 nm [9]. Thus, in future studies, a single detection channel can be used for the localization of AuNPs using MIL imaging. Measurements of the time decay of the MIL-signal further confirm that the detected signal is of photoluminescent origin. In contrast to the typical nano-second long life-times of autofluorescent, biological components [196], the signal emitted exhibits significantly faster $\leq$ 200 ps decay as indicated in Fig. 5.2 (D). This ultrafast emission corresponds well to the characteristics of AuNP photoluminescence previously reported in the literature [199].

Sensitivity at single-particle level, explained by the plasmonic enhancement of the emitted photoluminescence, is proven by comparison with TEM mea-

surements (Fig. 5.3 and Fig. 5.5) where AuNPs are mostly found to be isolated within endosomes separated by more than 300 nm. Since the resolution of CARS/MIL microscopy is limited to 300 nm, it is impossible to distinguish from the size of the photoluminescence feature a single AuNP from that of a small cluster of AuNPs. Also, due to the broad character of the emission spectrum of AuNPs, the frequency shift of the emission induced by plasmonic coupling is not readily measurable in MIL. Estimation of the number of AuNPs present in a cluster with sub-resolution dimension is conceivable through intensity calibration of the collected signal, although a simple relationship is not to be expected. Collections of AuNPs can not be considered as independent scatterers due to the coupling of their plasmons, resulting in collective enhancement effect [83]. Thus, the establishment of a calibration routine requires the support of thorough theoretical analysis, beyond the scope of the present study. A consequence of this collective enhancement is also that large amounts of energy are locally dumped in the immediate vicinity of the AuNPs [62]. Moreover, the probe beams may act as an optical tweezer on large clusters of particles [93]. The particles are then moved while being scanned, which could explain that the AuNP clusters in Fig. 5.5 (C) appear significantly larger than what is observed in the corresponding TEM images. We have indeed observed that the use of lower excitation powers in the laser beams reduces the apparent cluster size in these cells.

One of the surprising results shown in this work is the marked difference in AuNPs uptake between healthy human keratinocytes and a squamous carcinoma cell line. The number of cells investigated prevents a statistical analysis of the uptake process, however identical behavior was found for all cells investigated for each cellular system, implying that our results are of general character. The non-specific uptake of AuNPs in the two cell lines may be of interest from the perspective of applying functionalized particles for selective drug delivery. Previously, a significantly reduced cellular uptake of AuNPs has been reported after coating the NPs with the neutral ligand PEG, for other cell lines [61, 126, 150]. The nonreactive surface of the PEG-coated NPs and possible steric hindrance has been suggested to prevent the establishment of active contact with the cell membrane, so that efficient endocytosis cannot take place. While a limited number of isolated AuNPs indeed was found in the SCCs irrespective of incubation time, a significant amount of particles was observed in the keratinocytes by CARS/MIL microscopy. The amount of cellular AuNPs was found to increase with exposure, and the AuNPs were found to be distributed over the entire cell volume. This was independently confirmed by high-resolution TEM of selected cell sections (Fig. 5.2 and Fig. 5.5). The limited uptake of PEG-coated AuNPs for SCC cells is in accordance with previous observations specifically for SCCs [44], as well as for other cell lines [61, 126, 150]. This raises the question why PEG-coated AuNPs are so readily incorporated in epithelial keratinocytes.

Three factors should be taken into account while attempting to explain the different uptake: changes of the surface properties of the AuNPs, difference in the electrostatic properties of the membrane of individual cell lines, and the influence of differences in the composition of the incubation medium on the

properties of the cell membrane. The possibility that the surface properties of the PEG-coated AuNPs change upon contact with the different cell culture media, as a result, for instance, of spontaneous functionalization by the adsorption of proteins from the medium [31,32], is unlikely due to the inert properties of the PEG-coating irrespective of which proteins are present in the medium [62, 211]. The possible differences in electrostatic charges of the cell membrane of the two different cell lines is equally unlikely to play a role in the uptake of particles that present neutral charged surface coating. More probable is instead that the different scenarios can be attributed to cell-specific chemical properties. The internalization of AuNPs is a process strongly affected by efficient contact with the cell membrane. The adhesion can be either of non-specific character, resulting in direct penetration of the NP through the membrane, or mediated by receptors that provide specific adhesion, inducing the formation of NP-carrying endocytic vesicles (for a review on the receptor-mediated internalization pathways see [37]). With the exception of a few examples [18, 31], details of AuNP internalization are still largely unknown. The presence in high concentrations of human epidermal growth factor (EGF) in the growth medium is known to up-regulate macropinocytosis [92]. In our experiments EGF was present at low concentration (0.2 ng/mL) in the growth medium employed for the keratinocytes but not for SCCs, and might still contribute to account for increased internalization through this pathway. This hypothesis is supported by the broad size-span of the endosomes found in keratinocytes as observed in the TEM images, also including larger sizes (400-800 nm) characteristic for macropinosomes compared to other endosomes [195]. Confirmation of this hypothesis is beyond the aims of this work and can be envisaged in follow-up studies where the concentration of EGF in the medium is varied, although the above observations point toward an issue widely underestimated in studies on particles internalization. While the nanobio research field spends large efforts on investigating how different properties of the NPs affect the efficiency with which they are incorporated in cells, this study highlights that the incorporation mechanism is as well highly dependent on the cell line used, and perhaps even on the details of the medium.

5.5 CONCLUSIONS

Systematic studies on the incorporation mechanisms of AuNPs in living mammalian cells are, at present, limited by the lack of non-invasive imaging techniques. For this purpose, we introduce the combination of CARS and MIL microscopy, offering visual access to the interaction of nanomaterials with living matter thanks to label-free imaging of biomolecules and single-NP sensitivity. Since no sample preparation is required, a more realistic picture of the three-dimensional distribution of intracellular AuNPs in relation to the components of the cell is provided with high spatial resolution (300 nm lateral and $\sim 2\ \mu m$ axial), beyond the capabilities of other existing technologies. As an outlook, other cellular components than the lipid-rich cell membrane and subcellular

organelles may specifically be targeted in the CARS-channel by probing molecular vibrations characteristic for *e.g.* mitochondria and nucleic acids [34, 168], opening up for colocalization of AuNPs with further organelles without labeling.

The observations reported in the current work have implications both for (i) fundamental studies of NP-uptake mechanism and (ii) for clinical applications of NPs. Our work highlights the need for detailed characterization of the incorporation mechanisms used by different cell models, as they appear to be cell specific, probably as a result of the individual composition of the cell membrane; in contrast to squamous carcinoma cells and precious studies on several other cell lines, PEG-coated AuNPs are readily incorporated in healthy human epithelial keratinocytes. Thus, it is difficult to draw any general conclusions from fundamental studies of uptake mechanisms involving a single cell model and it raises the need for detailed characterization of the composition of the cell membrane. The clinical consequence of this observation is that PEG-coating may not be sufficient to prevent an undesirable, general uptake of NPs in conjunction with transdermal delivery of NP-based therapeutic and diagnostic agents. This adds to the need for more sophisticated coatings in order to avoid the potentially toxic accumulation of NPs in healthy cells, toward safe and efficient transdermal delivery of drugs, gene-regulating therapeutics and diagnostic agents only targeting diseased cells. As a promising alternative, nanoparticles labeled with anti-Epidermal Growth Factor Receptor (anti-EGFR) have been recently demonstrated to selectively target tumor cells through specific binding [41]. With the ability of 3-dimensional imaging of the distribution of functionalized AuNPs in living cells at single-particle sensitivity and without the need for labeling or sectioning, our work illustrates that CARS/MIL microscopy has the potential to become an important instrument for the development of further functional coatings as well as within the nano-bio research field in general.

6 Imaging of cell compartments of the wing disc

A key question in developmental biology is the understanding of how the development of organs is regulated during growth. Evidence has been presented of a strong connection in embryogenesis between the appearance of boundaries between specific cell types and the proliferation of such cell clusters in the growth of a tissue. Despite extensive efforts to understand how the fate of cells is determined during organs growth, little is known on the role that development of compartment boundaries and variations in the chemical composition of cells from different compartments play in the proliferation process.

We present here the application of broadband CARS hyperspectral microscopy to study the local chemical composition of cells in the developing imaginal wing disc of *drosophila melanogaster* larvae. While the occurrence of compartmentalization of the wing disc into the anterior/posterior and the dorsal/ventral regions has been known for decades, insights into variations in the local chemical composition have been lacking. Here, the chemical information contained in the CARS spectra is evaluated using Principal Component Analysis (PCA), allowing us to directly visualize the occurrence of cell clusters in the developing wing that each exhibit common chemical features.

Our results demonstrate that CARS microscopy is a powerful label-free alternative to fluorescence-based assays routinely used in developmental biology for the visualization of known and unknown compartments in developing organs.

6.1 Introduction

The development of a multi-cellular organism is one of the most fascinating issues of biology. Perfectly controlled and highly complex mechanisms are required for embryogenesis, as cells not only have to proliferate and differentiate, but they also have to sort into function-specific tissues. Whereas for most proliferating tissues, cells can move freely and occupy any position, in some cases the cells and their descendants are forced to remain in restricted areas of the tissue, called compartments. Between adjacent compartments, boundaries are created,

associated with a cell-segregation mechanism preventing cells of the compartments to migrate from one to the other. The establishment and maintenance of these sharp borders, called compartment boundaries, between cell populations is a crucial step in ensuring that the position of the regulation centers remains unmodified during development. Such regulation centers, also named organizers, are responsible for the entire signaling pathways at the base of tissue growth [21]. Transcription factors activate the organizer cells at the edge of a compartment, promoting the production of long-range organizing molecules (morphogenes) that orchestrate further growth and patterning of the tissue. The functioning of compartment boundaries is described in detail in Paragraph 6.6.

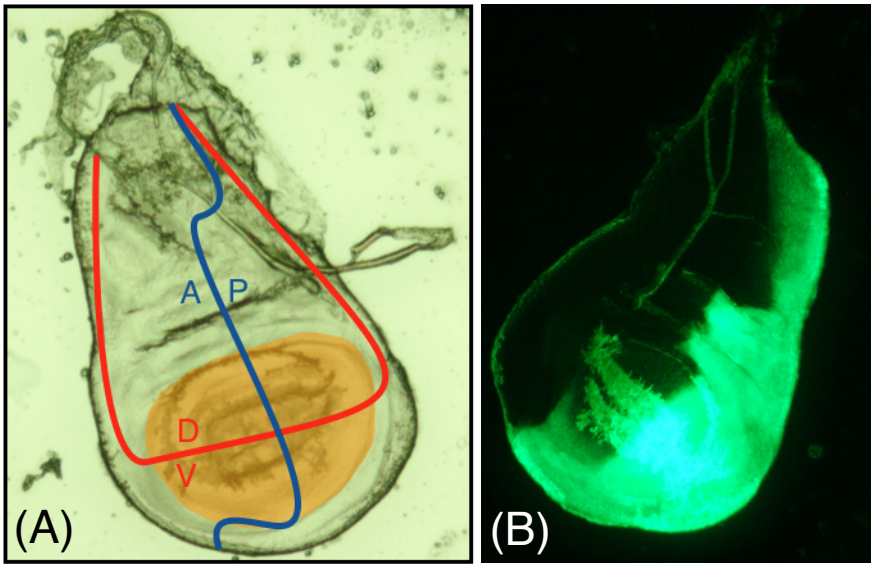

FIGURE 6.1. (A) Wing imaginal disc (brighfield microscopy image) of third instar larvae of *drosophila melanogaster*. The disc is divided into compartments determined by lineage restriction (classical compartment boundaries) and non-classical compartments. The main classical boundary follows the *decapentaplegic* (*dpp*) expression stripe and discriminates the anterior and posterior compartments (A/P, blue line). The second classical boundary develops along the *wingless* (*wg*) expression stripe separating the dorsal from the ventral cells (V/D, red). The separation between pouch (orange) and non-pouch region represents an example of non-classical compartment boundary. (B) Example of the visualization of the anterior/posterior compartment boundary in the wing disc by fluorescent marking. The fluorescence microscopy image refers to the wing disc of a *hh*Gal4-UAS-CD8-GFP fly. In this system the GFP is localized to the posterior compartment via the tagging to the Gal4 element that is controlled by the transcription factor *hedgehog* (see Paragraph 6.6).

Cell compartments have been known for decades to play an important role in the development of insects and invertebrates [79], but they are also found

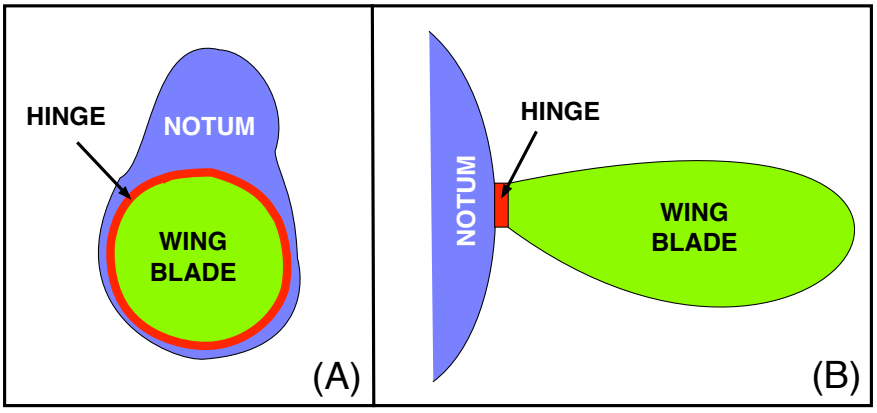

FIGURE 6.2. Schematic representation of the correspondence of compartments in the imaginal wing disc (A) and the wing of the adult organism (B). In the wing disc, the primordial wing blade (green) is localized at the intersection between the A/P and D/V boundaries in the middle of the disc. The non-classical hinge/notum boundary is represented by the red line. The remaining part of the disc (blue) is the notum. These compartments find their correspondence in the adult organism where the notum is integrated in the body of the fly, and the hinge creates the junction with the wing blade.

in vertebrates [117]. The *Drosophila melanogaster* is one of the best studied systems as it nicely exemplifies the role of compartments during development of the adult organism. The divisions between anterior/posterior and dorsal/ventral compartment boundaries appear in the early stages of the embryogenesis of the limbs of the drosophila. The adult tissues of the animal develop from clusters of undifferentiated cells, termed imaginal discs. The wing for example is derived from the wing imaginal disc by invagination of the embryonic epidermis along the intersection of the dorsal/ventral and anterior/posterior boundaries depicted in Fig. 6.1 (A). Like all other imaginal discs of the fly, the wing disc is made up of a columnar epithelium (disc proper) that grades into a squamous epithelium on the other side (peripodial membrane). The disc proper is the cell layer which differentiates into wing, hinge and notum (see Fig. 6.2) [74].

The division between the anterior and posterior compartments of the wing is the first to appear in the early stages of the growth, under the influence of the transcription factor *engrailed* which becomes selectively expressed in the posterior compartment. A more complex boundary perpendicular to the first is formed in the second larval instar, separating the prospective dorsal and ventral wing surfaces. The selector gene *apterous* expressed in the dorsal compartment is responsible for this further division of the imaginal disc [39]. Remarkably, at the end of the larval development the number of cells in the wing imaginal disc will be thousand-fold, but the activity and the position of these boundaries will be preserved during the growth and into the adulthood of the organism. Along-

side to compartments where cell segregation mechanisms are present, other non-classical boundaries also exist. The boundaries between the pouch and non-pouch areas and between hinge and notum are examples of borders that can be crossed by cells, consequently changing their fate.

Although the genes involved in the establishment of individual compartment boundaries have been known for decades, the phenomena underlying cell segregation are still largely unknown. Cell segregation might be based on variations in the strength of the cell adhesion in opposite compartments, as the result of variations in the activity of the signaling factor [80]. Yet, the identity of the specific molecules responsible for compartment formation and maintenance remains unknown.

The majority of the information relative to compartment boundaries has been obtained by marking groups of founder cells and following the position and shape of the descendent cells (clones). Clones of cells cannot cross the compartment boundary, but will instead remain physically restricted to either one of the two sides of the boundary, and form a straight line where they contact it. The marking procedure involves either genetic means such as somatic recombination, or the injection of intracellular dyes which persist through multiple rounds of cell division [73]. Fluorescent labeling of proteins with *e.g.* GFP (see Fig. 6.1 (B)), and the use of antibody staining has provided extensive information on the role of specific proteins in boundary formation [103]. The drawback of this approach is that the labeling procedure can lead to mislocalization or hindered functionality of the modified molecules, and it is only applicable to a limited range of molecular classes, mainly proteins and lipids [113]. Moreover, fluorescence tagging is only feasible when the target molecule is known, and therefore it is not suited for the screening of potential new candidate molecules. As compartment boundaries rarely follow morphological landmarks and they can only be visualized by lineage markers, it is conceivable that, even for well-studied systems such as the wing imaginal disc, not all boundaries have yet been identified.

In this chapter we present the application of broadband CARS to visualize cell compartments of the imaginal wing disc of *drosophila melanogaster* by determining the local chemical composition in the disc. In order to identify the characteristic chemical features of the system, PCA is used to analyze the CARS data. The application of multivariate statistical analysis to vibrational spectroscopy allows accounting for the small pixel-to-pixel spectral variations in hyperspectral datasets. This has provided a mean to distinguish between normal and diseased states in tissues and isolated cells [54], as well as to identify the individual components of cells [139] and functional units in mice meibomian glands [125]. Recently, PCA was used for processing CARS microscopy data to distinguish the biochemical components of a sample of completely unknown composition [161]. Nonlinear optical techniques have been used in the past to study drosophila. Two-photon fluorescence was used in combination with third harmonic generation to monitor the development of a whole embryo [193], and in combination with second harmonic generation to look at internal organs [124]. Single frequency CARS microscopy was used to obtain information on the struc-

ture of internal organs and fat body [30]. All these studies though, were focused on the study of the entire embryo and were not aimed to obtain information on cell compartments and their boundaries. Also, they did not attempt to retrieve the chemical composition of the system.

6.2 Materials and methods

6.2.1 Sample preparation

Wild type *yw* third instar larvae or genetically modified flies were used, all presenting the following genotype: *yw UAS-mCD8::GFP hsp-flp; hh-Gal4/TM6b* [162].

Wing imaginal discs were manually dissected and dehydrated in a 10xPBS solution (Sigma-Aldrich, Zwijndrecht NL) for 30 minutes. The discs were then mounted on conventional microscopy cover slides. Mounted discs were washed with MS grade water (Sigma-Aldrich, Zwijndrecht NL) three times to remove additional salts. For all CARS experiments, the discs were directly analyzed without further sample preparation.

Preliminary investigation of sample integrity was performed by visual inspection using a Leica DMRX microscope (Leica, Wetzlar, Germany). The microscope, equipped with an Osram HBO 50W/L2 short arc mercury lamp (Osram AG, Munchen, Germany), was also used to produce the fluorescence images of the wing discs.

6.2.2 CARS experimental procedures

Broadband CARS measurements were performed on the imaginal wing disc with the experimental setup described in Paragraph 3.2. The wing was initially visualized with standard brightfield imaging to allow for correct identification of the area of interest. The wing disc normally has dimensions of $\sim 300 \times 400\ \mu m^2$ in plane. The actual size of individual wing discs varies depending on the exact stage of growth of the animal at the time of dissection. CARS imaging was performed in three dimension by measuring adjacent tiles in the sample consecutively until the entire region of the sample was measured. Each individual tile has dimension of $75 \times 75 \times 26\ \mu m^3$ (corresponding to $76 \times 76 \times 14$ pixels). Acquisition time per voxel was set to 50 millisec in order to obtain good signal to noise ratio without compromising the integrity of the sample.

6.2.3 Data analysis

Raw CARS spectra were analyzed with the program *Igor Pro*. Pretreatment of the data with the MEM algorithm [202] retrieves the imaginary component of the third order susceptibility (see Paragraph 2.2), referred to as retrieved CARS spectra in this thesis. Advanced image treatment made use of the software ImageJ.

Prior to Principal Component Analysis, CARS spectra were exported from the analysis software as text files. Spatial binning of the data was necessary to increase the signal to noise ratio and to reduce computer memory requirements. The text data was converted to *Matlab/ChemomeTricks* data format using the in-house developed *CARS2Tricks* software. Individual CARS measurement tiles were stitched together using the in-house developed *StitchCARS* software. The *ChemomeTricks* software was then used to normalize the spectra and extract the principal components and associated scores maps.

6.3 RESULTS

6.3.1 HYPERSPECTRAL IMAGING OF THE WING DISC

Broadband CARS measurements were performed on the entire imaginal wing disc in three dimensions in order to obtain a hyperspectral image of the system. For each voxel within the disc, the retrieved CARS spectrum was obtained across the spectral region between -3200 and -900 cm^{-1}. The size of each voxel was independently measured to be $\sim 1 \times 1 \times 2\ \mu m^3$ determined by the intrinsic confocality of the technique with the employed experimental configuration.

The CARS response measured at an arbitrary position within the disc is presented in Fig. 6.3, where the spectral region between -2700 and -1800 cm^{-1} has been excluded as vibrations eventually present in this range produce an intensity below the detection limit. This spectral interval characterized by low response is often referred to as the silent region of the Raman spectrum of biological matter [17]. The integration time for this spectrum is 1 second.

Two regions of interest can be distinguished in the spectrum, the fingerprint and the C-H stretching region. The fingerprint region between -1800 and -900 cm^{-1} presents several overlapping peaks whose chemical nature has been extensively studied and the assignment can be found in literature [144]. Part of the vibrations in this region can be assigned to individual classes of molecules. The peaks between -1290 to -1400 cm^{-1} (CH bending and deformation), between -1400 to -1480 cm^{-1} (CH_2 scissoring and bending, CH_3 bending), and at -1650 cm^{-1} (C=C stretching) are assigned to lipids. The peaks at -1002 cm^{-1} (phenylalanine), between -1200 and -1300 cm^{-1} (amide III) and at -1650 cm^{-1} (amide I) are instead assigned to proteins. Finally, the peak between -1060 and -1095 cm^{-1} (PO_2^- stretching) is assigned to nucleic acids.

The C-H stretching region between -3150 and -2750 cm^{-1} contains overlapping vibrations arising from CH, CH_2, and CH_3 groups abundant in most biological species. Interestingly, although most of these peaks are indistinctive of the class of molecules, vibrations specific to lipids are found in the lower wavenumbers spectral region below -2875 cm^{-1} [144]. Also, peaks specific of amino acids have been assigned in the high wavenumbers region above -2930 cm^{-1} [102].

Owing to the large response obtained in the C-H stretching region, unspecific maps of the morphology of the wing disc can be obtained by integrating

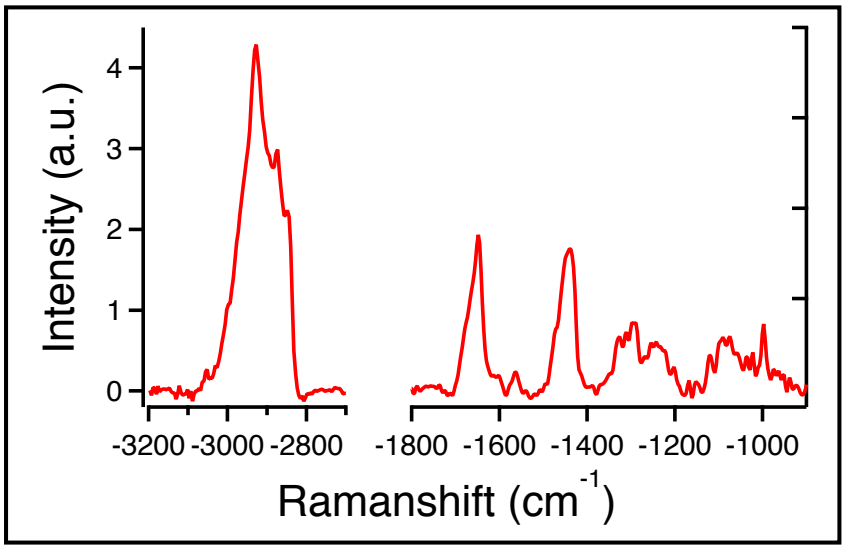

FIGURE 6.3. Retrieved CARS spectrum at an arbitrary position within the wing disc. The region of the spectrum at high wavenumbers (C-H stretching region) contains overlapping vibrations from the CH, CH_2, and CH_3 groups abundant both in lipids and proteins. The region at low wavenumbers (fingerprint region) contains a large number of peaks that have been assigned to specific vibrations of lipids, proteins and nucleic acids. The intermediate region of the spectrum is omitted due to the absence of vibrations specific to biological compounds.

the intensity of the retrieved CARS signal between -3020 and -2850 cm^{-1}. As already mentioned in the previous chapters, the intrinsic confocality of CARS provides vertical sectioning capabilities of the wing disc along the axial direction. Hence, individual layers across the sample can be imaged independently. Fig. 6.4 (A) and (B) show the morphology of two individual sections of the disc, recorded at distance of approximately 10 and 2 microns from the glass support respectively. The first layer (A), located further from the glass support, presents a largely inhomogeneous response highlighting the wiggly conformation of the columnar epithelium layer [57]. The Y-shaped trachea is clearly outlined in the right side of the image. Here, the low intensity of the signal is possibly due to the dilution of the nutrients contained in the trachea tube. The second layer (B) is located very close to the glass support, where a flattening of the disc is to be expected. The edges of the disc are clearly distinguishable, and the signal inside the disc is homogeneous, with dark areas visible in correspondence with the folds of the epithelium. Here the trachea is only barely visible, indicating that this component of the disc is not located in this optical layer.

Three dimensional rendering of the entire wing disc can be obtained by combining the optical sections. From the rendering view of the disc it can be concluded that the overall chemical integrity of the sample is well preserved and

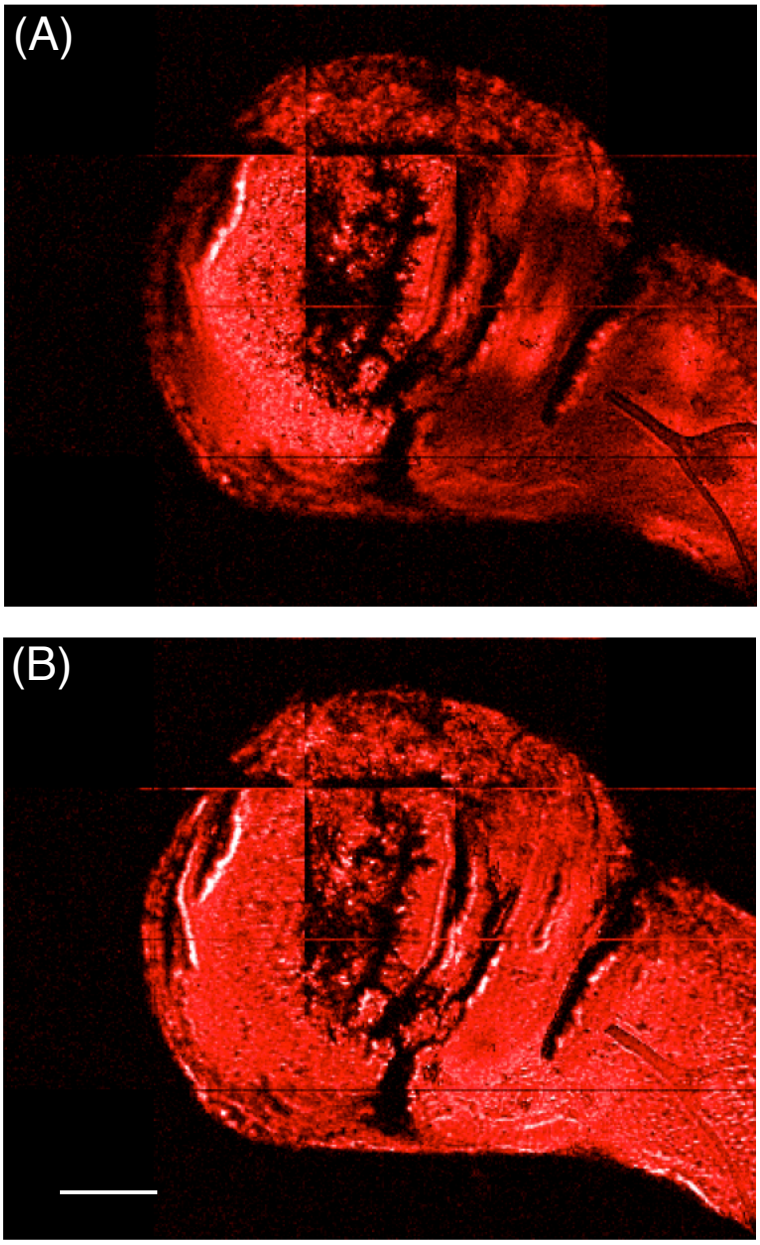

FIGURE 6.4. CARS images of individual layers of the wing disc. Layer (A) and (B) refer to an axial position of approximately 10 and 2 microns away from the glass support respectively. The intensity values in the image are obtained by integrating the CARS response in the C-H stretching region of the spectrum at each position in the sample. Scale bar: 50 microns

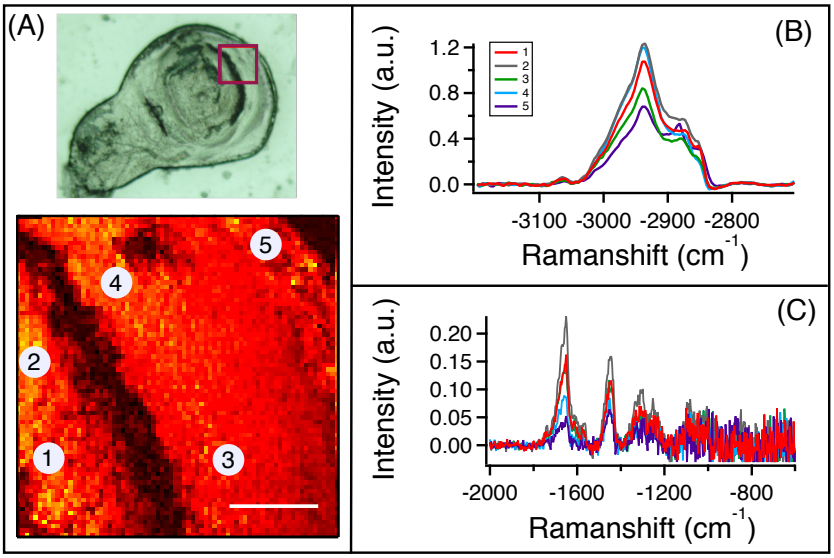

FIGURE 6.5. (A) CARS map of an area of the disc located in a region where the boundaries between hinge/notum and anterior/posterior compartments are expected to be visible, contoured by the purple square in the brightfield image at the top. Scale bar 20 microns. (B) C-H region and fingerprint region (C) of the spectra of the five points marked in the map in panel (A).

no significant topography is visible. Specifically, these overall intensity maps obtained do not show topographic features reminiscent of any of the compartment boundaries known to be present in the imaginal wing disc.

6.3.2 CHEMICAL DIFFERENCES IN THE CARS SPECTRA

Unspecific maps of the wing disc only make use of a small portion of the information contained in the CARS spectra of the system. In particular, the quantitative chemical information has so far been left practically unused. As an initial method to identify chemical differences at different locations within the disc, visual inspection of the spectra was employed. Fig. 6.5 (A) presents the map of the C-H CARS intensity of an area of $75 \times 75\ \mu m^2$ located in a region of the disc where the boundaries between the hinge/notum and the anterior/posterior compartments are expected to be visible (purple square in the brightfield image at the top of Fig. 6.5 (A)). The image refers to an optical layer located $\sim 8\ \mu m$ above the glass support. The CARS map resembles closely the features visible in the brightfield image, with a low intensity region cutting across the area in correspondence with a fold of the epithelium. The most intense response (yellow areas) is found in the inner part of the sample. The simple observation of the CARS map provides no elements allowing the identification of compartment

PC	EV	% Variance
1	64.82	15.73
2	26.71	6.482
3	14.04	3.408
4	12.61	3.061
5	6.247	1.516
6	5.458	1.324
7	4.997	1.212
8	4.150	1.007
9	3.680	0.893
10	3.290	0.798

TABLE I. Eigenvalues and variance percentage associated with the first ten principal components. The PCs are calculated from the hyperspectral dataset relative to an individual optical layer inside the wing disc.

boundaries, although the trend of the intensity of the signal vaguely reminds of the configuration expected for the notum/hinge division (cfr. Fig. 6.2). Five locations are marked on the map, and the corresponding spectra in the C-H and fingerprint region are shown in Fig. 6.5 (B) and (C) respectively. In the C-H region, the main differences in the spectra are the relative intensities of the three major peaks at $\sim$ -2930, $\sim$ -2880 and $\sim$ -2845 cm^{-1}. The spectra at position 1, 2, and 3 are qualitatively similar, although they differ in the intensity of the signal. The spectrum at position 4 differs from the others by the lower relative intensity of the two peaks at lower wavenumbers, whereas the spectrum of position 5 presents higher relative intensity of these peaks and a blueshift of the position of the -2880 cm^{-1} vibration.

In the fingerprint region of the spectrum, the reduced signal to noise ratio makes the identification of distinctive vibrational features more challenging. Again, we found a similar ratio ($\sim$ 1.3) of the peaks at -1650 and -1450 cm^{-1} for the spectra 1,2, and 3. This ratio becomes close to one for spectrum 4 and in the case of spectrum 5 the -1450 cm^{-1} peak becomes larger than the -1650 cm^{-1} peak.

Inspection of the spectra of Fig. 6.5 thus clearly indicates that the vibrational response of the wing disc varies with the position. On the other hand, even if quantitative parameters could be defined using peak fitting, the enormous amount of data points in the disc makes the visual inspection of the spectra an impractical approach to identify the chemical differences between cell compartments.

6.3.3 PCA OF THE WING DISC CARS DATA

The retrieved CARS signal from individual optical sections isolated from the three-dimensional dataset were investigated with Principal Component Analysis

to identify recurring features in the spectra. The eigenvalues and the associate percentage of variance for the first ten principal components (PCs) are listed in Table I.

The function associated to the first PC is presented in its statistically normalized form in Fig. 6.6 (A). Statistically normalized refers here to rescaling the intensity values at different frequencies in order to give to each frequency the same statistical weight. This component features a collection of a large number of peaks across the entire spectral window, with a broad peak centered at -2915 cm^{-1} with two shoulders at -2880 and -2850 cm^{-1} corresponding to undifferentiated CH stretches. Also the negative peaks in the fingerprint region at -1650 and -1450 cm^{-1} are insufficiently specific to relate the first component to a distinct molecular class. The non-normalized function representing the first PC is also shown in Fig. 6.6 (B) to provide an expression of the component directly comparable with the measured CARS spectra.

The scores maps and the false color map relative to the first PC are shown in Fig. 6.7. As described in Paragraph 2.3, the scores map quantify spatially the importance of the features present in the associate n^{th}-PC. At each position, the score value is in fact the coefficient of the development of the original spectrum along the n^{th} dimension of the PCs basis. Positive and negative score intensity values are generally represented in two separate maps. Interestingly, the scores maps in figure show a division indicative of the anterior/posterior differentiation, with the posterior compartment highlighted in the negative map and the anterior compartment highlighted in the positive map.

The function associated with the second PC is presented in its statistically normalized form in Fig. 6.8 (A). This function is characterized by a pronounced dispersive feature in the C-H region of the spectrum. The negative part of the feature extends from -3020 to -2920 cm^{-1}, whereas the positive part continues till -2830 cm^{-1}. The shape of the function hints to the possibility that the negative score points are associated to a larger presence of proteins features in the original spectra, whereas the positive points are more lipid related [102,144]. This explanation is supported by the presence of two positive peaks in the fingerprint region at -1430 and -1300 cm^{-1} assigned to the CH_2 bending and CH_2 deformation of lipids in tissues respectively [132]. The non-normalized form of the second PC is also presented in Fig. 6.8 (B).

The scores maps and false color maps relative to the second PC show a differentiation reminiscent of the hinge/notum compartments. Large positive scores value are visible in the central part of the disc, where the notum is located (cfr Fig. 6.2). The negative scores reach lower absolute values, and they are localized in the area corresponding to the hinge.

It is important to underline that PCA results, both in terms of score maps and principal components, were consistent for all the sections of the four wing discs independently investigated. Fig. 6.10 shows the first two components (blue) retrieved from the analysis of the measurement performed on the wing disc of another fly. The PCs obtained are compared with the results previously shown (red). Blue and red functions are compatible, and differ, at most, in their intensities. The score maps associated with the new measurement are

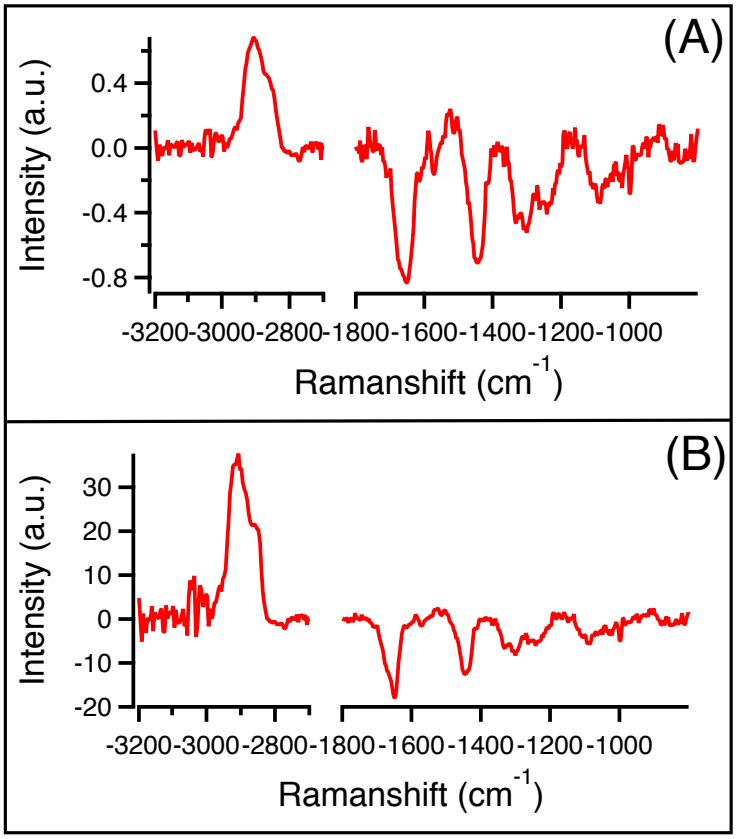

FIGURE 6.6. Statistically normalized (A) and non normalized (B) spectra of the first Principal Component retrieved from the analysis of the CARS hyperspectral image of the wing disc

also shown. Further spatial binning of the data prior to PCA analysis was also tested with compatible results. This excludes the influence of the spatial inhomogeneities over the micrometer lengthscale on the results obtained.

The results obtained for the third principal component, although not yet conclusive, should still be mentioned. The most interesting spectral features of the third PC are found in the C-H spectral region, shown in Fig. 6.11 (A) together with the score maps (B) and (C). The function has the same dispersive shape found for the second PC, with a negative peak from -3020 to -2920 cm^{-1}, followed by a positive part that continues till -2830 cm^{-1}. The scores maps on the other hand, do not resemble the hinge/notum compartments found for the second component. The signal instead is rather homogeneous both for the positive and negative map. Closer inspection of the data shows round features in the maps, with spatial correlation across consecutive layers. The third com-

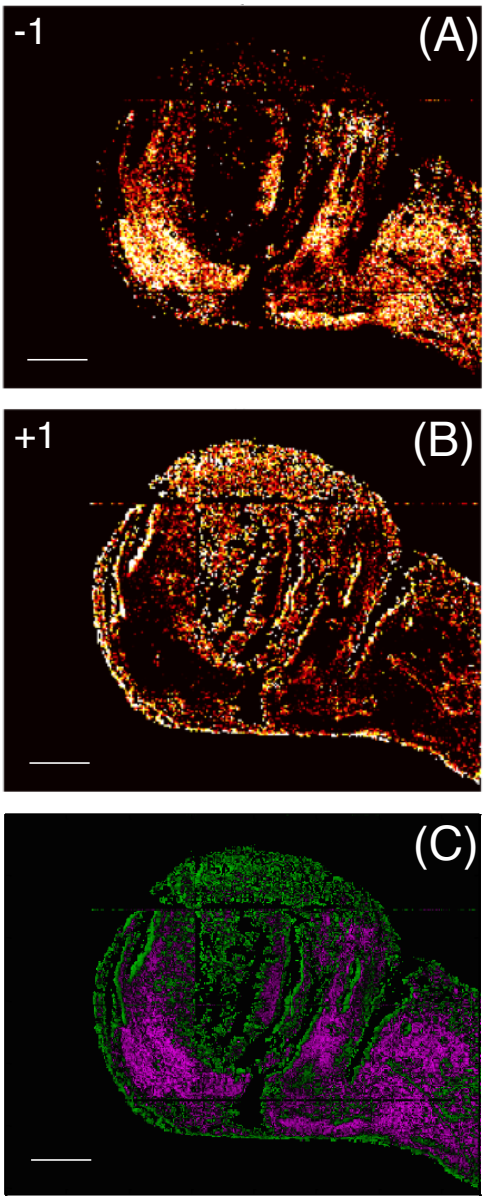

FIGURE 6.7. (A) negative, (B) positive, and (C) false color scores maps of the first Principal Component retrieved from the analysis of the CARS hyperspectral image. The scores maps show a division compatible with the anterior/posterior boundaries in the disc.

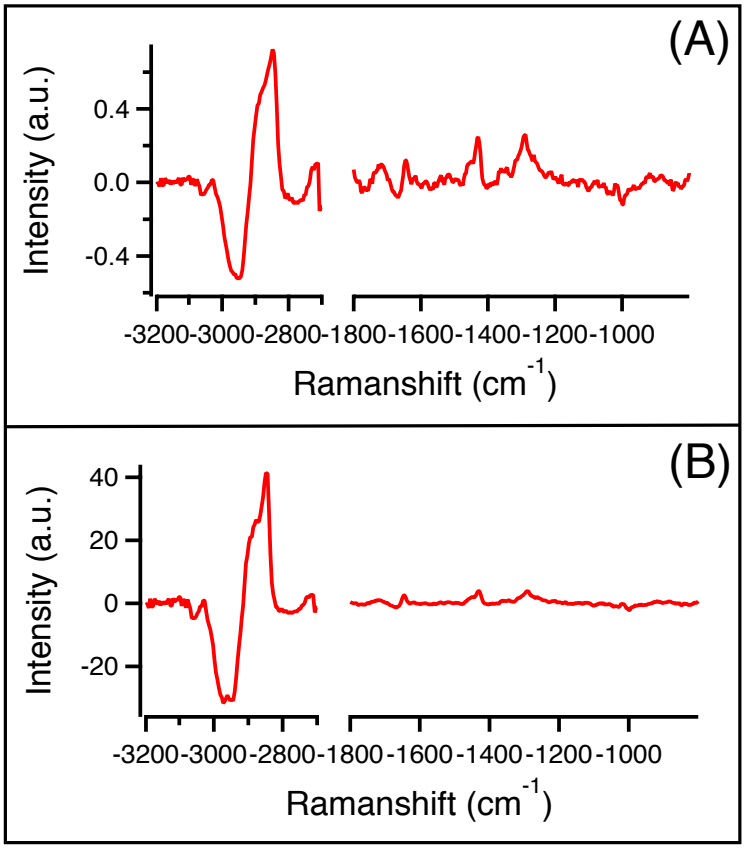

FIGURE 6.8. Statistically normalized (A) and non normalized (B) spectra of the second Principal Component retrieved from the analysis of the CARS hyperspectral image

ponent is therefore tentatively attributed to identify the outside membranes of the cells. In order to confirm this hypothesis, additional measurements with higher resolution would be required.

6.4 DISCUSSION

The unspecific maps of the wing disc obtained by visualizing the integrated signal in the C-H region of the spectrum at each position within the sample provide clear visualization of the morphology of the wing disc. Albeit accurate, the use of hyperspectral CARS images to address the morphology of the system is possibly a suboptimal choice. The main drawback of broadband CARS is the duration of the experiments required to obtain good signal to noise ratio across the entire spectral window measured. The imaging process of the entire wing

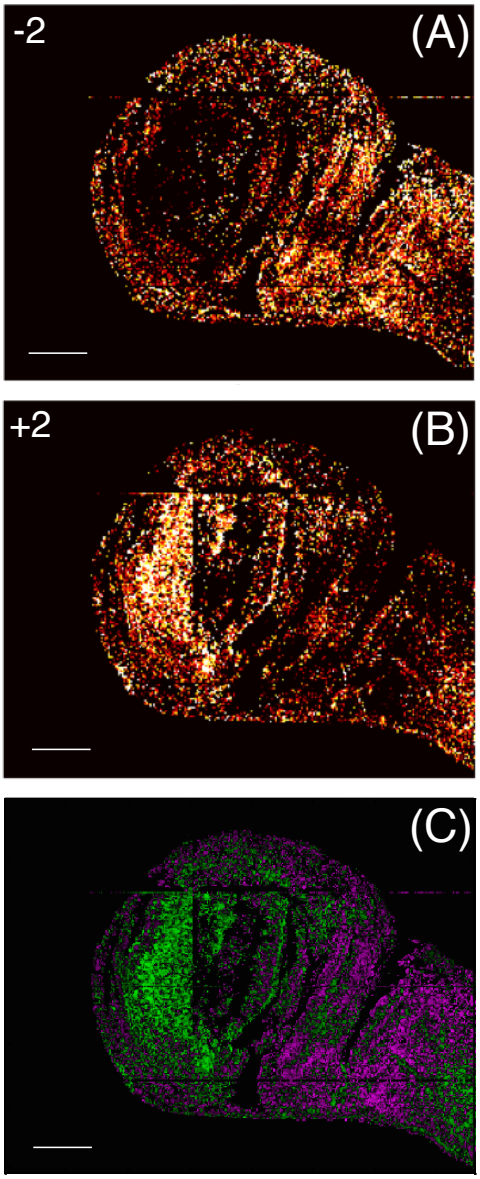

FIGURE 6.9. (A) negative, (B) positive, and (C) false color scores maps of the second Principal Component retrieved from the analysis of the CARS hyperspectral image. The scores maps show a division compatible with the hinge/notum boundaries in the disc.

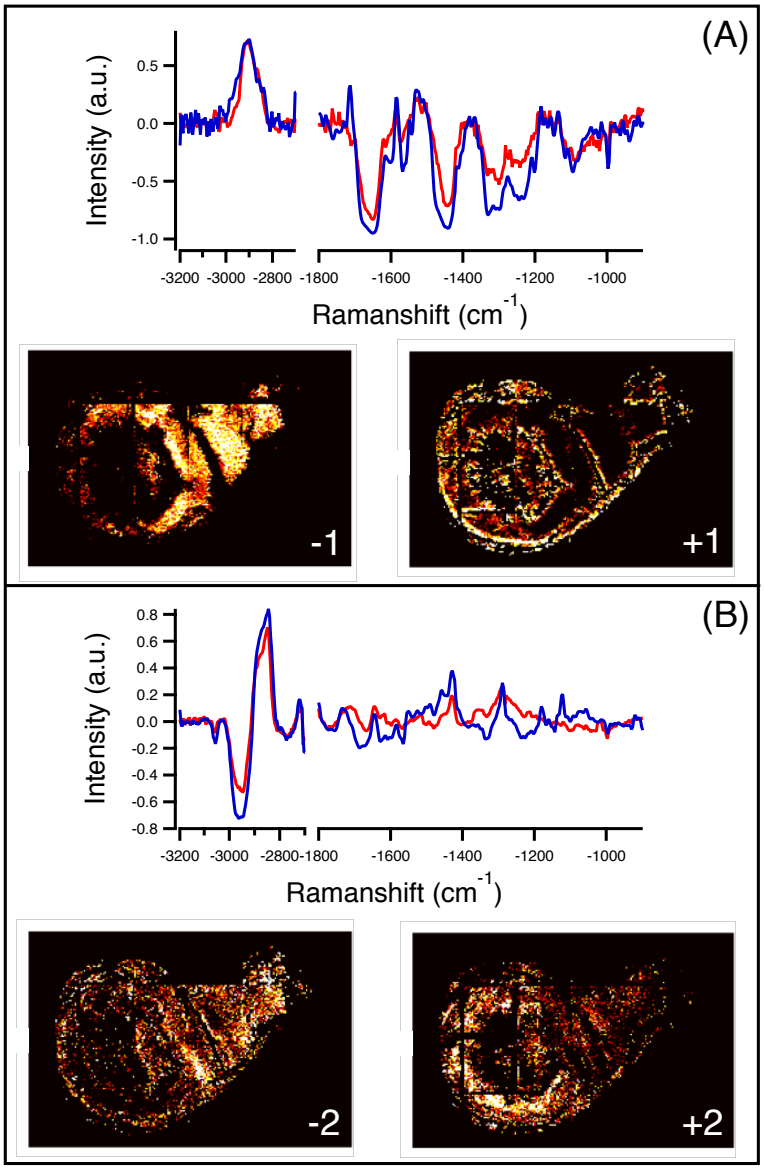

FIGURE 6.10. (A) and (B) functions of the first and second Principal Components respectively (red) calculated from an independent CARS measurement performed on the wing disc of a different fly, and the associated scores maps. In blue the functions of the components calculated for the first wing disc (Fig. 6.6 and Fig. 6.8).

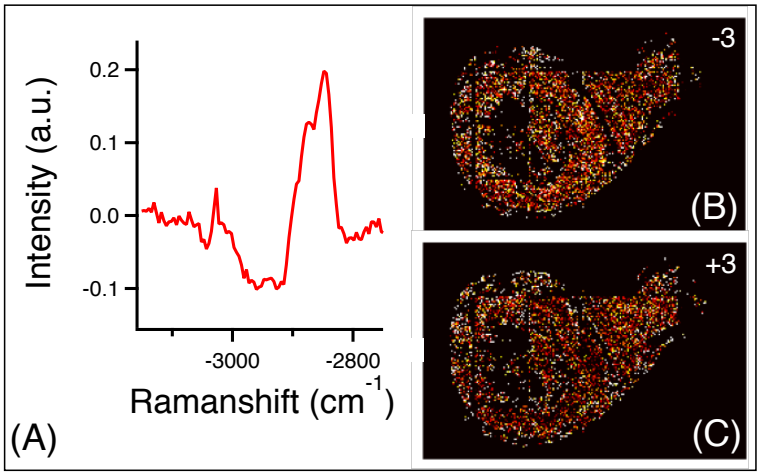

FIGURE 6.11. (A) C-H region of the spectrum of the third PC. A dispersive lineshape centred at $\sim$ -2920 cm^{-1} is present, similarly to the case of the first PC. (B) and (C) are the associated scores maps. Closer inspection reveals features reminiscent of the cell membranes.

disc in three dimensions can take as long as three to five days depending on the size of the disc. Such long measuring time becomes worthwhile only thanks to the chemical information contained in the vibrational spectra. For simple morphology studies, single frequency CARS experiments are instead recommended. As shown in the images presented in Paragraph 6.7, single frequency CARS can provide as well the maps of the concentration of CH moieties in the disc, with higher contrast and spectral resolution, and reduced measurement time compared to broadband CARS.

On the other hand, hyperspectral CARS microscopy provides direct access to the chemical composition of the compartments in developing organs. Retrieving and quantifying this information though is complicated primarily due to the large variations in the composition of the system on the length scale probed by CARS. The typical spectrum measured inside the disc presented in Fig. 6.3 contains the overlapped spectral signatures of several compounds, often belonging to different chemical classes, *e.g.* proteins, lipids, and nucleic acids. Direct deconvolution of the vibrational spectrum is non trivial even in the case of a limited number of known constituents, but becomes unfeasible in the case of biological tissues where the constituents are unknown. Visual inspection of the spectra at individual spatial position within the disc provides some basic knowledge on the chemical differences as shown in Fig. 6.5. In particular, the ratios between the amplitude of selected peaks could in principle provide local information on the degree of saturation of the organic compounds and the order of their arrangement [179]. This approach, that is very successful for the study of cells composition in vitro, produces less exciting results in the case of a

system like the wing disc of the drosophila. In fact, tissues are in general much more compact than cell cultures in vitro. As a result, it becomes very difficult to distinguish components such as lipid droplets or any other intracellular structure.

Moreover, the compartmentalization of the disc intrinsically induces another complication. If we simplify the functional divisions of the disc by assuming that only two compartment boundaries are present, *e.g.* the A/P and hinge/notum boundaries, and we also assume that complementary compartments are characterized by some chemical difference, we immediately notice that each cell of the disc must simultaneously belong to two compartments. Hence, if a given cell is for example part of the anterior compartment and of the ventral compartment, it will be characterized by the chemical signature of both.

In order to visualize individual compartment boundaries and access the underlying chemical differences, Principal Component Analysis provides the ideal approach for spectral decomposition. In PCA, the original spectra are projected along a new basis in the vibrational space calculated by the maximization of the variance contained in the CARS dataset (cfr Paragraph 2.3). This unsupervised approach is likely to serve the purpose of deconvoluting the chemical differences relative to non complementary compartments. This concept is more easily explained using the previous example where only two boundaries are present in the disc. In this case the successful application of PCA separates the chemical information underlying each of the two compartmentalization. The chemical features characterizing the A/P division are then entirely contained in one of the principal components. Specifically, in our experiments we found that the A/P division was expressed by the first PC as shown in Fig. 6.6 and Fig. 6.7. Along the spectral direction identified by the PC, the two compartments are associated to scores values of opposite sign, comparable to the on- and off-states of the underlying chemical feature. The hinge/notum division was instead identified along the second principal component, shown in Fig. 6.8 and Fig. 6.9.

Although these results were consistent in terms of spatial distribution and spectral signature of the compartments for all the investigated layers from several wing disc samples, only two compartmentalizations were found in the CARS data. PCA could not identify other spectral directions immediately related to known compartmentalizations of the disc. It is possible that the information relative to other compartments is also contained in the CARS data, although presenting lower variance, undetectable by PCA. Alternatively, the chemical differences in other complementary compartments might be beyond the detection capabilities of CARS. As the Raman contrast arises from vibrations of chemical bonds, molecules belonging to the same chemical class are hardly distinguishable, restricting in fact the capability of CARS to distinguish compartments associated with chemically macroscopic differences in composition.

The results presented in Table I show that part of the information contained in the CARS data is not efficiently detected by PCA. The first two PCs are characterized by the larger values of associated percentage of variance, although $\sim$ 70 % of the variance is still contained in the remaining components. All the first ten PCs express enough variance to be considered statistically significant,

although they were not found to be associated with recognizable compartmentalizations. It is hence possible that other information on cell boundaries is still contained in the other PCs.

As mentioned above, the first PC was found to identify the A/P division in the disc. The spectrum representing the component shows no vibrational features allowing the identification of the molecular classes intervening in the process. The scores maps in Fig. 6.7, outline clearly the two compartments. Comparison with fluorescent images of the posterior compartment (Fig. 6.1) shows a clear compatibility of the results. Direct comparison of the results is not possible as hyperspectral CARS experiments were unsuccessful on fluorescently marked wing discs, due to the partial absorption of the light from the dye. The presence of fluorescent markers in the sample is also likely to contaminate the CARS spectra, inducing possible artefacts in the results. Also, differences in the shape of the compartments can be explained by the intrinsic differences between the CARS and fluorescence measurement. Due to the intrinsic confocality, CARS measures the signal from optical sections within the disc, whereas the fluorescence system used in our experiments measures the response integrated over the entire thickness of the sample. The compartments found from the CARS data should be best compared with the results obtained with a confocal fluorescence microscope.

The hinge/notum compartment was instead identified by the second principal component. The spectrum of the component in Fig. 6.8 (A) features a dispersive line shape centered at -2920 cm^{-1}. The negative peak in the higher wavenumber region could be an indication of a large presence of proteins in the notum compartment visible in Fig. 6.8 (A). The positive peak in the lower wavenumber region could instead indicate a large presence of lipids in the hinge compartment, Fig. 6.8 (B). The lipidic origin of the positive features is also supported by the presence of the two peaks in the fingerprint region at -1430 and -1300 cm^{-1}. As already mentioned, these peaks have been assigned to the CH_2 bending and CH_2 deformation of lipids in tissues respectively [132].

An alternative explanation refers instead to the order of the molecules in the system. In fact, Raman measurements on lipid samples at varying temperatures have been used to demonstrate that the variation in the peak intensities of the -2850 cm^{-1} (CH_2 symmetric stretch), -2880 cm^{-1} (CH_2 asymmetric stretch), -2935 cm^{-1} (CH_3 symmetric stretch), and -2960 cm^{-1} (CH_3 asymmetric stretch) can be used as probes for investigating the conformational arrangement of lipids. In particular, an increase in the ratio of the intensities of the -2935 and -2850 cm^{-1} peaks reflects chain melting and an increment in trans-gauche isomerization in the system [24]. In our results, this would be reflected in a high level of local disorder associated with the negative features of the second principal component, hence in the notum compartment on the disc.

The same arguments also apply to the description of the third component. The scores maps presented in Fig. 6.11 contain features arguably representing the cell membranes. If this hypothesis were to be demonstrated, an explanation of the spectral features in terms of lipid order would be of great interest.

6.5 CONCLUSIONS

The establishment of compartment boundaries and maintenance during embryogenesis are very well studied phenomena. In *drosophila melanogaster* a multitude of compartments are described in literature [45, 103]. Although the signaling pathways regulating the growth of the tissue are often known, the chemical differences between complementary compartments are yet to be clarified. In order to overcome the limitation of the techniques currently available based on genetic markers, we have tested broadband CARS microscopy as a tool to investigate compartments in the wing disc of *drosophila melanogaster*, based on the chemical signature of the molecules present in the system. The intrinsic vibrations of molecules directly provide label free access to the composition of the systems. The interpretation of the CARS hyperspectral dataset using a multivariate analysis method (PCA) allowed identifying two independent compartmentalizations in the disc, the anterior/posterior and the hinge/notum compartments. The hinge/notum division was interpreted by a different composition in terms of lipids and proteins in the two regions. The A/P division instead, although clearly visible in the scores map, could not be interpreted in terms of chemical differences. Additional measurement with other chemically specific hyperspectral techniques such as secondary ion mass spectrometry (SIMS) could provide a complementary mean to help identifying the molecules involved in the formation and maintenance of compartment boundaries in developing organs.

6.6 APPENDIX I: COMPARTMENT BOUNDARIES

Although the establishment and maintenance of cell compartments and their boundaries during cell proliferation is a phenomenon that depends greatly on the chemical species involved in the specific process, the underlying biochemistry remains mostly unchanged. We will briefly introduce this process, using the anterior/posterior (A/P) division in the imaginal wing disc as typical example [118]. The structure of the typical compartment boundary is shown in figure Fig. 6.12. At the beginning of the compartmentalization, two groups of cells physically located in the vicinity of the appearing boundary line are selected in the embryo. The two groups will be forced by the patterning mechanism to differ in the expression of a *selector* gene, which in the case of A/P division is the gene *engrailed*. This gene is expressed by the posterior cells (selector gene on) and it is not expressed by the anterior cells (selector gene off). This is the only step of the process where an external mechanism is involved, as the state of the expression of the selector gene becomes a hereditary factor for the cells involved. The two initial groups of cells are consequently compartmentalized according to their capability to express the selector gene. An important ingredient for the success of boundary formation is the concurring cell segregation system that acts by sorting the two cell groups apart, in order to create a defined edge of the compartments (represented by the dashed line in figure) taking the name of

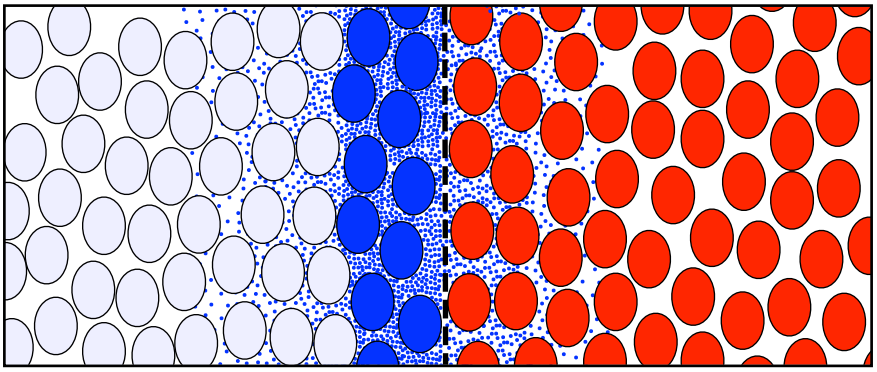

FIGURE 6.12. Representation of the organization of cells and signaling expression across a compartment boundary. A tissue is subdivided into two cell population that different in the expression of a selector gene. A cell segregation mechanism provides a sharp separation of the two different cell groups that identifies the compartment boundary (dashed line). The cells on the left (grey and blue) and on the right (red) of the line are characterized by the on and off state of expression of the selector gene with short signaling range. The selector gene activates the expression of a long range organizing molecule (morphogen, blue dots) in the cells of the opposite compartment located in the vicinity of the boundary (blue). As the morphogen diffuses in the tissue, it regulates the growth and patterning of both compartments.

compartment boundary. To the left and the right of the dashed line in Fig. 6.12 the cells belonging to the anterior and posterior compartments respectively are present.

In the following step, the cells in the posterior compartment (red cells in Fig. 6.12) begin to synthesize the short-range signaling molecule *hedgehog* (*hh*). This process is directed by the selector gene, that also makes the posterior cells immune to the interaction with the *hh* itself. On the contrary, the cells in the anterior compartment are prone to respond to the interaction with the *hh*. Incidentally, due to the short range of the signaling molecule, only the anterior cells close to the compartment boundary will be involved in the interaction (blue cells). These cells take the name of *organizer*.

Finally, the anterior cells reached by the *hh* will respond to the interaction by emitting a morphogen, a long range organizing molecule. The morphogen, *Decapentaplegic* (*DPP*) for the A/P division, diffuses away from the organizer cells giving rise to a graded distribution (blue dots). The growth and the patterning of the whole tissue are then regulated by the morphogen via the induced expression of target genes in a concentration-dependent manner.

A complete treatment of the development of compartment boundaries in developing organs can be found in [21].

6.7 APPENDIX II: SINGLE FREQUENCY CARS ART

In this paragraph, single frequency CARS microscopy images of the imaginal wing disc are shown. These measurements are not part of the study on the chemical composition of the system, but belong instead to a set of preliminary measurements aimed to produce high resolution, label free images of the shape and arrangement of the cells in the disc across compartment boundaries. Changes in the arrangement of the cells are in fact believed to be of relevance for elucidating the role of cell adhesion in pattern formation (cfr. Paragraph 6.1). Single frequency CARS tuned to match the -2845 cm^{-1} vibration of CH bonds allows for accurate visualization of the edges of the cells in the tissue, although at this stage it cannot be ruled out the possibility that other components of the tissue produce high contrast in the CARS images. Conclusive results obtained with this approach would require to be validated by the comparison with standard immunostaining measurements where cell membranes can be labeled with a fluorescent tag.

For these experiments, the sample preparation was the same as described in Paragraph 6.2.1, and the experimental setup is described in Paragraph 3.1. The images depict consecutive layers within the wing disc separated of 1 μm covering an area of 50×50 μm^2 (corresponding to 256×256 pixels). Acquisition time for each layer is 20 s, with signal intensity normalized by dividing the response by the non-resonant signal measured in the glass support. The panels in the image are numbered consecutively according to the vertical position, starting above the disc and moving toward the glass support.

Fig. 6.13 and Fig. 6.15 refer to two regions where the boundary of the notum/hinge is expected to be present. It should be noted how the contours of the cells, visible as high intensity lines, change in shape across the layers. We should remind here that, at this stage of the growth, the wing disc is composed of two layers of epithelium tissue only, the thick columnar epithelium and the thin peripodial membrane. The enlargements of the previous figures shown in Fig. 6.14 and Fig. 6.16 also highlight that the alignment and shape of the cells changes sharply in the images. We believe that these transition lines might colocalize with the compartment boundaries. The validation of this hypothesis is non-trivial as CARS measurements on the wing disc in presence of a fluorescent marker for a specific compartment are hindered by absorption effects of the signal due to the large concentration of the dye. CARS images then appear clear in the non-labeled compartment, but the intensity of the response drops considerably in the complementary compartment where the marker is present.

In Fig. 6.17 compartment boundaries are not expected to be present. The figure gives instead a clear representation of the three dimensional structure of the trachea inside the disc. High resolution images of the trachea *in vivo* are, at the top of our knowledge, not accessible with standard fluorescent techniques.

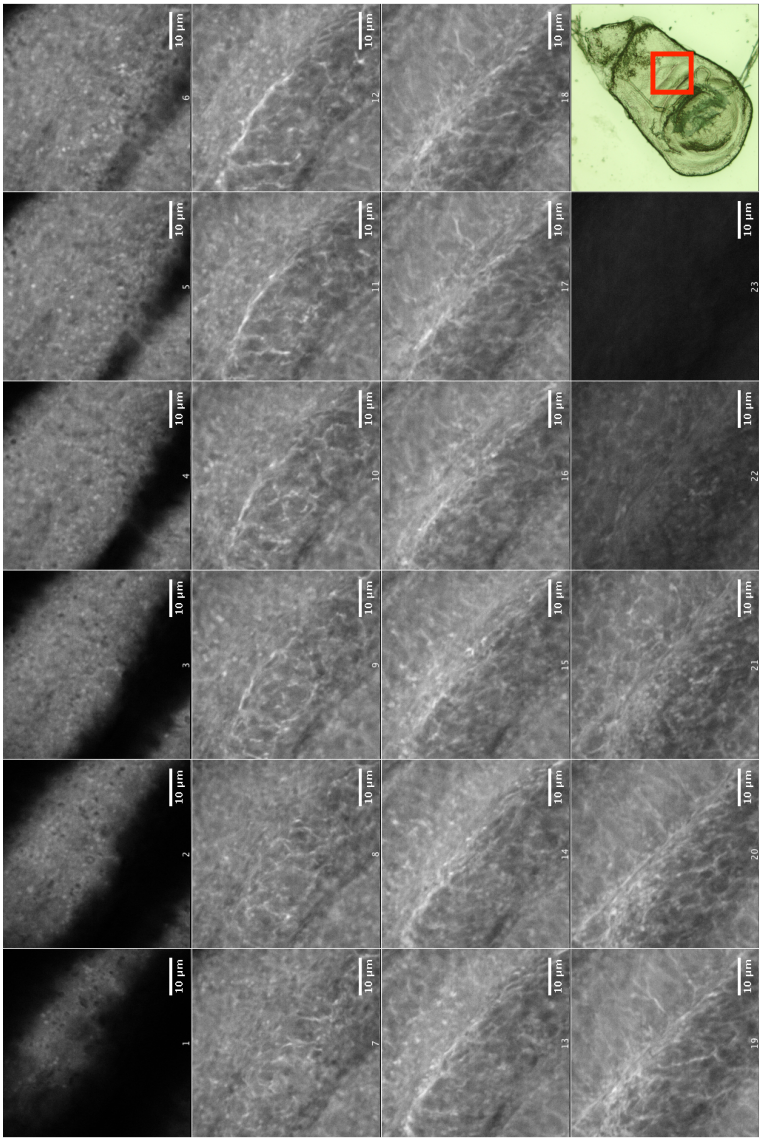

Figure 6.13.

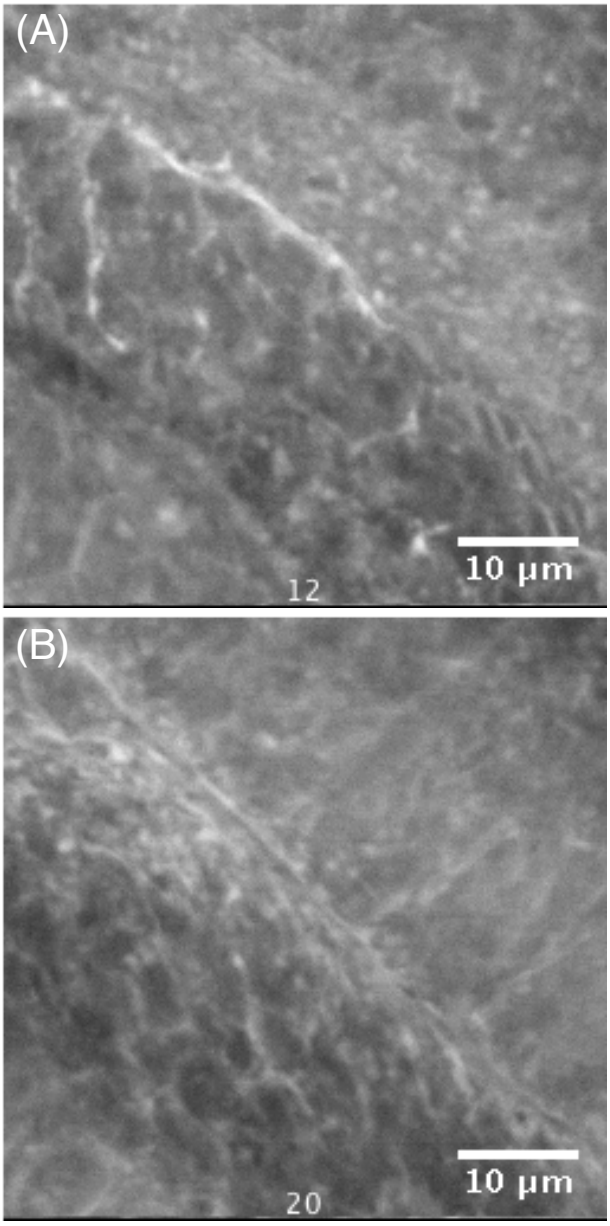

FIGURE 6.14.

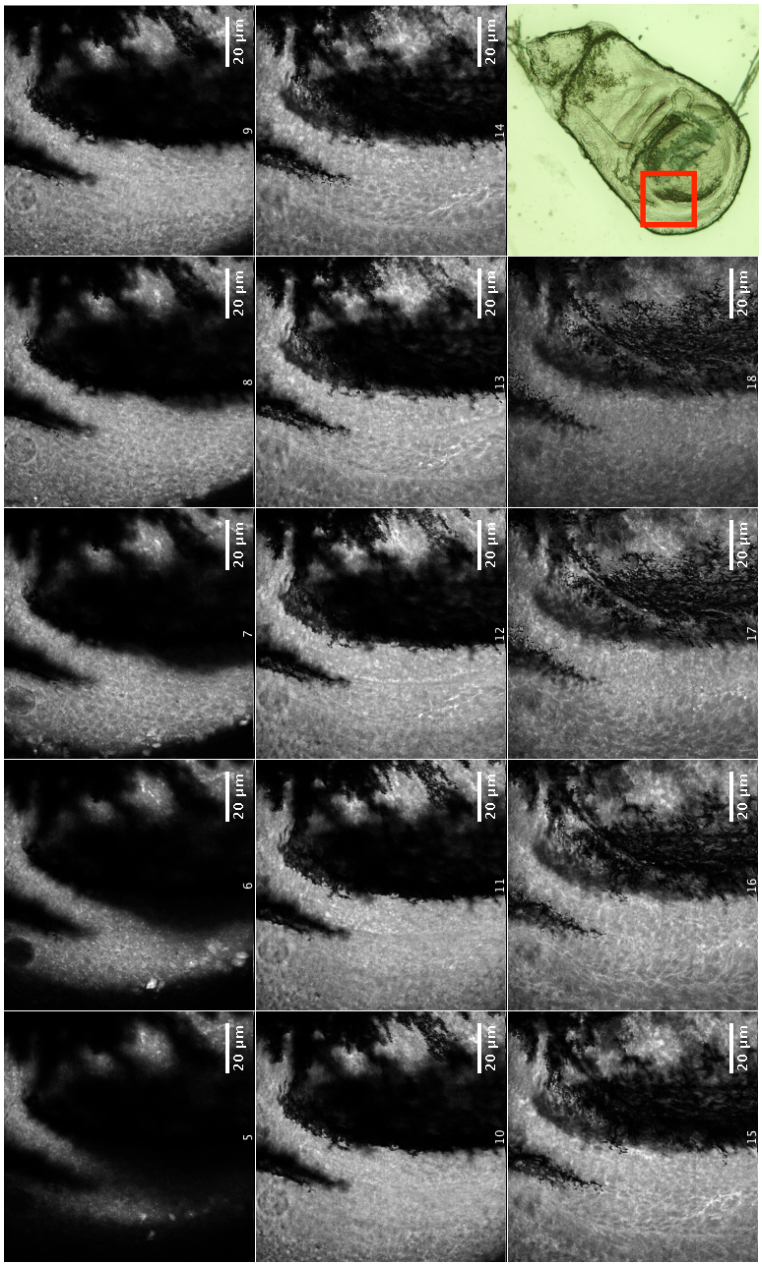
20 µm
5
20 µm
6
20 µm
7
20 µm
8
20 µm
9
20 µm
10
20 µm
11
20 µm
12
20 µm
13
20 µm
14
20 µm
15
20 µm
16
20 µm
17
20 µm
18

FIGURE 6.15.

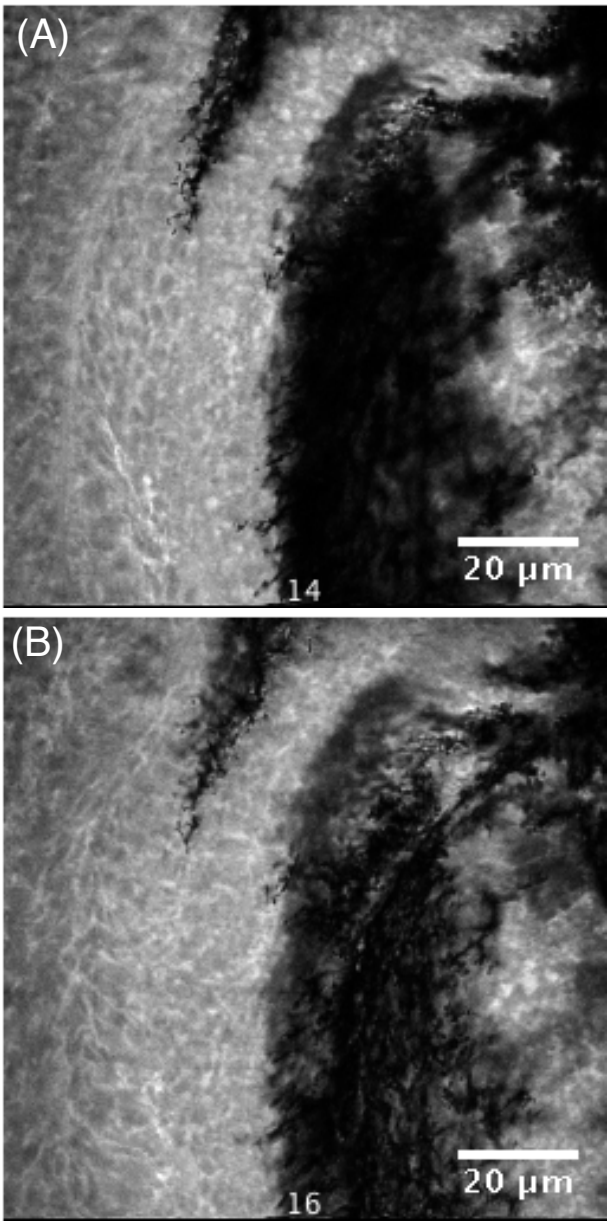

FIGURE 6.16.

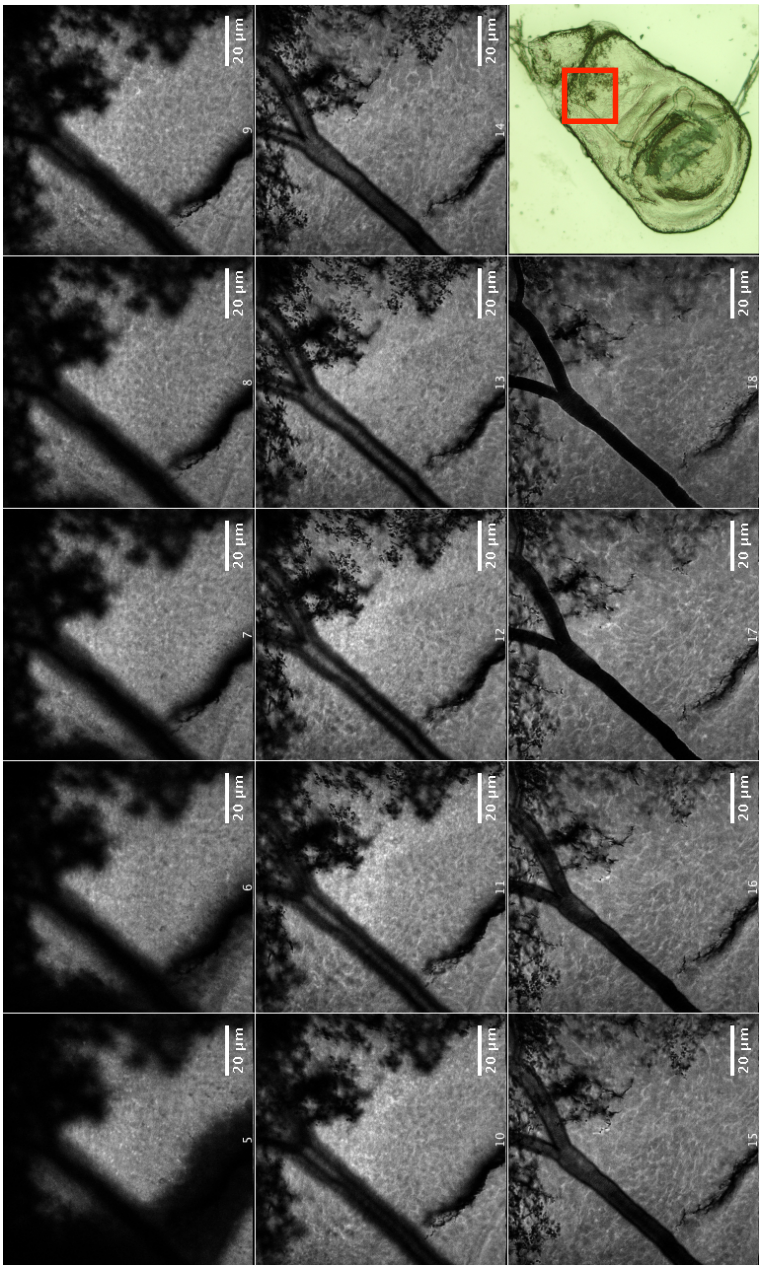
20 µm
9
20 µm
14
20 µm
8
20 µm
13
20 µm
18
20 µm
7
20 µm
12
20 µm
17
20 µm
6
20 µm
11
20 µm
16
20 µm
5
20 µm
10
20 µm
15

Figure 6.17.

7 Imaging of biological components in muscles

The accumulation of lipids in the body is one of the major factors determining the occurrence of health diseases such as type II diabetes. In particular, the ectopic storage of lipids in skeletal muscles is believed to be related to the regulation of insulin sensitivity. Despite extensive efforts to understand the chemical composition of lipid droplets in tissues, as well their dynamic processes, progress in the field has been hampered by the lack of an experimental technique able to provide simultaneously the visualization of the biological components of the tissue, and information on their chemical composition. We present here the application of CARS spectro-microscopy to study cells in tissues in which one protein is overexpressed, which is known to be important for lipid metabolism. These cells have high density of lipid droplets. Evaluation of the CARS data with multivariate analysis methods allows us the identification of lipid droplets and possibly mitochondria in the tissue, based solely on their vibrational response. Our preliminary results show that CARS spectro-microscopy can complement standard immunohistochemistry techniques to retrieve local chemical information on individual biological components of the muscles.

7.1 Introduction

Obesity[a] is one of the major health risks in western countries, with an increasing prevalence of 1.4 billion adults worldwide [153]. Among other health threats, such as cardiovascular diseases, type II diabetes is one of the best-described resulting pathologic outcomes of chronic obesity. Type II diabetes is defined as the general resistance of an organism to its own insulin. Insulin, whose role in the organism is to trigger the uptake of glucose into cells, will consequently be secreted at higher levels from the pancreas compensating for excess glucose in the blood stream. The manifestation of diabetes occurs when the pancreas is not capable of compensating for this excess of glucose, resulting in relative insulin deficiency and hyperglycaemia. Complications of type II diabetes include

[a]Obesity can be indicatively defined using the oversimplified body mass index (BMI). The index is calculated as the body mass in kg divided by the square of height in meters. Individuals with BMI values of 25 and higher are considered as overweight, 30 and higher as obese.

hypertonia, retinopathy, neuropathy, and nephropathy.

While the cause of type II diabetes is not entirely understood, strong evidence has been presented for imbalanced energy uptake and expenditure as the origin of the pathology (reviewed by Lee *et al.* [120]). One hypothesis sees lipid overflow as the major contributor to the onset of insulin resistance. Lipid overflow occurs when adipose tissue becomes incapable of storing lipids efficiently. Subsequently, lipids start to accumulate in other tissues of the organism: skeletal muscles, cardiac muscle or the liver. Among these, skeletal muscles take up the highest total amount of glucose via insulin signaling.

The accumulation of lipids in the skeletal muscles, also named intramyocellular lipids (abbreviated hereafter as IMCL), strongly correlates to large values of the body mass index (cfr. note *a*), and has been reported to impair insulin sensitivity in various *in vitro* and *in vivo* investigations [3, 88]. On the other hand, diet-induced reduction of IMCL has also been found to reduce insulin resistance [105]. Efforts to understand the impact of IMCL levels on insulin resistance are further complicated by the finding of the so called *athletes paradox*. Endurance trained athletes, who are highly insulin sensitive, show similar or even higher IMCL levels when compared to obese diabetics [87]. Furthermore, physical training improves insulin sensitivity in obese subjects, while at the same time elevating the IMCL level [136]. These apparently contradictory findings are currently explained by the occurrence of toxic lipid intermediates, which have been shown to decrease insulin sensitivity. Diacylglycerides (DAG) and ceramides in particular have been shown to interfere with insulin signaling. However, the exact mechanisms responsible for the correlation between IMCL level and insulin resistance remain to be clarified (reviewed by Bosma et al. [12]).

In order to understand ectopic lipid accumulation, the way lipids are stored has to be taken into account. Lipid droplets (LDs), the main site of neutral lipids storage in cells, are nowadays recognized as active organelles as opposed to mere oil droplets. LDs are composed of a phospholipid monolayer and a protein coating, enclosing a core of di- and triacylglycerides (DAGs, TAGs), cholesterolesters and free fatty acids. Proteins coating lipid droplets have been shown to be highly involved in lipid synthesis and lipolysis, thus presenting an important interface for lipid metabolism. The best-characterized group of LD coating proteins are the perilipins (PLIN1-5). Different members of this protein family are expressed differentially depending on the specific tissue. PLIN1 is primarily found in the adipose tissue, PLIN2 and PLIN5 are instead expressed in cardiac and skeletal muscles. Research in LD dynamics and interaction, while gaining momentum, is still a young field of study where several questions remain to be answered. For example, relatively little is known about the composition of LDs in cells, their size distribution and core protein content. Also, the biogenesis of LDs in mammalian cells is still to be clarified, with different studies proposing contradicting hypotheses regarding the mechanisms of LDs formation (reviewed by Suzuki *et al.* [194]).

The protein Perilipin 5 (PLIN5, sometimes referred to in literature as OXPAT) has been identified as one of the LD coating proteins predominantly ex-

pressed in tissues with high fat-oxidative capacity, such as the heart muscle, type I fibers of skeletal muscles and brown adipose tissue. While it largely localizes to LDs in these tissues, it can also be found in the cytosol of cells, and has recently been reported to be present in myocellular mitochondria [13]. The function of PLIN5 is partly still to be explained; overexpression *in vitro* leads to increased TAG storage and formation of larger LDs in the cytoplasm, while at the same time increasing fatty acid oxidation and mitochondrial mRNA levels [210]. When overexpressed locally *in vivo* by electroporation, PLIN5 induces formation of large LDs when compared to empty vector controls, as was observed by immunofluorescence and transmission electron microscopy. Interestingly, muscle tissue in which PLIN5 was overexpressed, showed increased oxidative capacity in the entire muscle homogenates, whereas isolated mitochondria from the same tissue did not show increased oxidative capacity when challenged with free fatty acid. Thus, PLIN5 seems to play a role in the LDs mitochondria interaction, making fatty acids available for mitochondrial β-oxidation.

The major bottleneck in the study of metabolic processes involving lipids in tissues is the lack of suitable techniques capable of simultaneously addressing the localization and the chemical composition of LDs and of the other biological components present in the samples. Thin (5-20 μm) sections of muscle tissue can be routinely investigated by immunohistochemistry approaches, the most employed of which is immunofluorescence. In this technique, specific components of the tissues such as membranes, nuclei, or specific proteins are labeled with an antibody chemically linked to a fluorescent molecule. Direct labeling is achieved when the antibody recognizes the target molecule and binds to it, and the fluorophore it carries can be detected by fluorescence microscopy. Indirect labeling is instead mediated by an unlabeled primary antibody that binds to the molecule of interest. Here, the secondary antibody, which carries the fluorophore, selectively recognizes the primary antibody and binds to it. For the analysis of LDs, usually lipophilic dyes such as Oil red O, Nile red or Bodipy are used. Using a confocal fluorescent microscope, labeled components within the tissue can be visualized with sub-micron resolution. Due to the characteristics of the technique, immunohistochemistry can be employed in the study of tissues only for the visualization of components for which a suitable labeling antibody is available, and only a limited number of structures can be imaged simultaneously. This is particularly problematic for the study of LDs, where information on the local lipid composition would be desirable. The application of immunhistochemistry in the study of biological tissues is reviewed by *e.g.* Brandtzaeg [19]. The chemical composition of the fatty acids in muscle tissues can instead be obtained by gas chromatography (GC), where the amount of individual chemical species present in the sample is quantified [182]. Hence, GC serves the purpose of identifying the composition of lipids in the investigated tissue section, although the information it provides is global. A satisfactory compromise to obtain the local distribution of chemicals in the tissue is the use of spatially resolved mass spectrometry techniques such as MALDI-Imaging Mass Spectrometry (MALDI-IMS). This technique enables the detection with high sensitivity (femto to attomolar) in a small region of the sample of molecules

in a large range of masses (from small molecules of $\sim$ 100 Da to large proteins, bigger than 300 kDa). Incidentally, the spatial resolution of the technique is limited to tens of micrometers, preventing direct access to the chemical composition on smaller length scales [91]. It is then clear that the understanding of the biological mechanisms involving lipids in muscles, such as the ectopic lipid accumulation, would benefit from the use of a technique capable of determining the local chemical composition of the tissue without the need of exogenous labels.

In this chapter we present the application of broadband CARS spectromicroscopy to study muscle tissues where the protein PLIN5 was selectively overexpressed. Using CARS in combination with multivariate analysis tools we were able to address the composition of the tissue on the micrometer scale and to distinguish the biological constituents based on their chemical signature, as confirmed by immunofluorescence imaging of the sample.

7.2 Materials and methods

7.2.1 Electroporation

A total of eighteen 8-week-old male Wistar rats were purchased from Charles River (Wilmington, Massachusetts, USA). Rats were housed individually on a 12:12 h lightdark cycle (light from 7:00 am to 7:00 pm), at room temperature (2122C) with ad libitum access to tap water. Rats were fed a high fat diet (45% energy from fat, D01060502, Research Diets, New Brunswick, NJ, USA) for the duration of the 3-week intervention. The Animal Care and Use Committee of Maastricht University approved the experiments (approval number 2010-036) and the study complied with the principles of laboratory animal care. During the experiments, all efforts were made to minimize suffering of the animals. Two weeks after the start of the diet, overexpression of Plin5 in either the right or left tibialis anterior (TA) muscle of the rat was accomplished by an in vivo DNA electrotransfer technique to obtain overexpression of mouse perilipin 5 in one leg; the contralateral TA served as a sham-electroporated internal control. Plin5 was electroporated randomly in the left or the right TA. DNA electroporation was performed under isoflurane anaesthesia. TA muscles were transcutaneously injected with either 150 g (2 g/l) pcDNA3.1-CMV-Plin5 or pcDNA3.1-empty vector in 0.9% sterile NaCl. Within 15 s after the last injection 5 electric pulses were applied by two stainless steel plate electrodes placed at the ventral and dorsal side of the leg. One high voltage pulse of 800 V/cm and four low voltage pulses of 80 V/cm at 1 Hz were generated by an ECM 830 electroporator (BTX, San Diego, CA, USA) as described previously (Bruce et al. 2007, 2009). Rats were sacrificed 8 days post electroporation. TA muscles were excised and rapidly frozen in melting isopentane for histology and protein isolations.

7.2.2 BODIPY STAINING AND IMMUNOFLUORESCENCE

Frozen TA muscles were transferred to a cryostat and cut transversally into serial sections (5 μm and 20 μm). After mounting on uncoated glass slides, sections were allowed to dry for 30 min at room temperature and then stored at -20C until processing. Five consecutive sections were cut from each sample of muscle tissue. The first section of 20 μm was used for CARS measurement, followed by four 5 μm sections, the first two of which were used for CARS and immunofluorescence respectively. The remaining two sections were kept for backup experiments.

One of the 5 μm sections from each sample was stained for lipid droplets, OXPAT expression, mitochondria localization as well as sarcolemmal cell borders in order to be investigated by immunofluorescence . All staining procedures were carried out at room temperature. Sections were fixed for 1h (4% PFA in 1xPBS, pH 7.4) and washed three times for 5 min in PBS prior to blocking for 1h in blocking buffer containing 2% BSA. The sections were then incubated with primary antibodies diluted in blocking buffer against OXPAT (dilution 1:20; GP31, Progen Biotechnik, Heidelberg, Germany), OXPHOS (dilution 1:20; MitoProfile, Abcam, Cambridge, UK) and Laminin (L9393, Sigma Aldrich, St. Louis, USA) for 1h in a humidified chamber. After washing three times with PBS, sections were incubated with appropriate secondary antibodies (Alexa Fluor 350, 546 and 647, all from Invitrogen, Darmstadt, Germany), DAPI, and Bodipy 493/503 diluted in blocking buffer. Following three washing steps, sections were mounted in fluorescence mounting medium (Dako, Glostrup, Denmark) and imaged on an Olympus IX70 inverted microscope (Olympus, Hamburg, Germany) using Cell F imaging software. Images were processed and overlays created using ImageJ.

7.2.3 CARS EXPERIMENTAL PROCEDURES

For CARS experiments, 5 and 20 μm consecutive sections of the muscle tissue were used without further preparation. Broadband CARS measurements were performed on the tissues using the experimental setup described in Paragraph 3.2. The sections were initially visualized with standard brightfield imaging to allow for correct identification of the area of interest. CARS imaging was performed in two dimension by measuring adjacent tiles in the sample consecutively until the desired region of the sample was measured. Each individual tile has dimension of 20×20 μm^2 (corresponding to 81×81 pixels). Acquisition time per voxel was set to 200 ms in order to obtain good signal to noise ratio without compromising the integrity of the sample.

7.2.4 DATA ANALYSIS

Raw CARS spectra were analyzed with the program *Igor Pro*. Pre-treatment of the data with the MEM algorithm [202] retrieves the imaginary component of the third order susceptibility (see Paragraph 2.2), referred to as retrieved CARS

spectra in this thesis. Advanced image treatment made use of the software ImageJ.

Prior to Principal Component Analysis, CARS spectra were exported from the analysis software as text files. The data was converted to *Matlab/ChemomeTricks* data format using the in-house developed *CARS2Tricks* software. Individual CARS measurement tiles were stitched together using the in-house developed *StitchCARS* software. The *ChemomeTricks* software was then used to normalize the spectra and extract the principal components and associated scores maps.

7.3 Results and discussion

7.3.1 Brightfield and immunofluorescence imaging of the tissues

In order to investigate muscle tissues where the protein PLIN5 was selectively overexpressed, preliminary measurements were performed with brightfield and immunofluorescence microscopy to study the morphology of the system. Fig. 7.1 shows two brightfield images of corresponding areas in two consecutive sections with thickness of 5 (A) and 20 μm (B), cut from the same muscle tissue. As the measurements are performed on consecutive sections of the muscle which have different thickness, some differences in morphology can be noted in the images, although the corresponding cells are easily identified in the two panels. Also, owing to the difference in thickness of the tissues, higher contrast is obtained in the brightfield image of the 20 μm section.

As the sections are obtained as transversal cuts of the muscles, the cells, which are composed of myofibrils, appear as nearly round structures contoured by thick black features corresponding to the sarcolemmal borders. Through visual inspection of the images, the cells can be indicatively divided in two groups according to the different morphology. For the cells of the first group, *e.g.* the large cell in the center of the figures, the brightfield response appears featureless, indicating a large degree of homogeneity in the local composition. The cells in the second group show instead a large number of dark features, indicating the intracellular presence of biological components with different density. Preliminary experiments with immunostaining of the protein PLIN5 (data not shown) highlighted that this second group corresponds to the cells where the protein was efficiently overexpressed, and large lipid droplets were present in the cells as a result of the modification. The difference in the expression of PLIN5 in neighboring cells in a tissue globally treated with electroporation is related to two factors: (i) the electroporation process is not effective in all the cells in the tissue [155]; (ii) the protein PLIN5 was found to be more efficiently expressed in type I oxidative (slow) cells in the muscles, compared to type II (fast) cells.

Although brightfield microscopy is instructive for the investigation of the morphology of the sample and for tentative identification of the cells expressing PLIN5, it provides limited insights into the intracellular chemical structure of

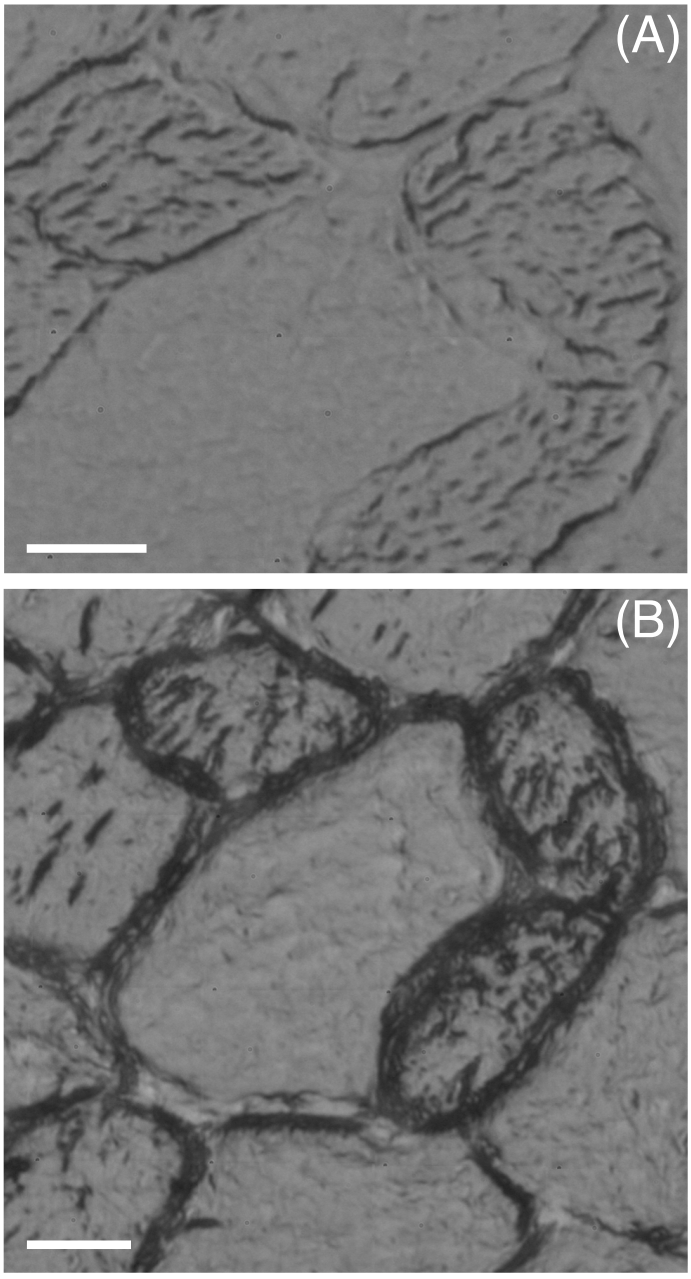

FIGURE 7.1. Brightfield images of the corresponding areas of two consecutive sections of muscle tissue of 5 (A) and 20 microns (B) thickness, respectively. The muscle was previously treated to selectively induce the overexpression of the protein PLIN5. Scale bar 20 microns

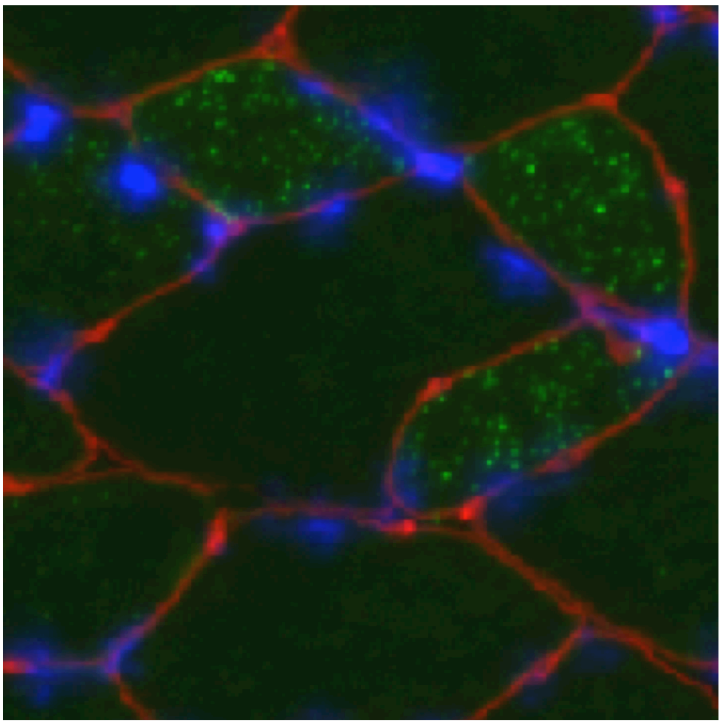

FIGURE 7.2. Immunofluorescence microscopy image of a 5 microns section of the muscle tissue. Three labels were used for the identification of different components: DAPI (blue), Bodipy (green), and laminin (red) bind to nuclei, lipid bodies, and sarcolemmal cell borders, respectively. The image shows the corresponding region of the tissue as the one presented in the brightfield images in Fig. 7.1.

the tissue. The immunofluorescence microscopy image of the corresponding area of the tissue is presented in Fig. 7.2. The measurement was performed on a 5 μm thick section of the tissue stained for three different components. DAPI (blue) was used to label cell nuclei, Bodipy (green) for lipid bodies, and laminin (red) for sarcolemmal borders. The edges of the cells are neatly identified by the red lines marking the cell membranes. Nuclei are visible as blue features in the proximity of the membrane. In muscle cells the nuclei present elongated shape oriented along the stretching direction of the muscle. Interestingly, the cells showing intracellular structures in Fig. 7.1, which are expected to overexpress the protein PLIN5, also feature the most interesting lipid distribution in the fluorescence image. Several round green features are present in each of these cells, pointing to the presence of intracellular lipid aggregates. The bodipy response in the cells not expected to show protein overexpression is instead reduced to a homogeneous low intensity background, and no distinctive features are visible.

7.3.2 HYPERSPECTRAL IMAGING OF THE MUSCLE

Hyperspectral CARS datasets were obtained in two dimensions in the disc in order to image regions of interest in the sections of the muscle tissue. At each position, the CARS spectrum was retrieved in the spectral region between -3200 and -900 cm^{-1}. The intrinsic resolution of the instrument with the employed experimental configuration was independently measured to be $\sim 1 \times 1 \times 2\ \mu m^3$. The CARS response measured at an arbitrary position in the tissue is presented in Fig. 7.4 (B) and Fig. 7.3 (B) for the 5 and 20 μm thick sections, respectively. These spectra were measured with 1 sec integration time.

As already discussed for the spectrum from the imaginal wing disc (cfr. Fig. 6.3), two regions of interest can be distinguished in the spectrum, the fingerprint and the C-H stretching region, separated by a silent region between -2700 and -1800 cm^{-1}. As already outlined in Paragraph 6.3.1, the fingerprint region between -1800 and -900 cm^{-1} presents several peaks assigned in literature to the vibrations of specific molecular bonds [144]: CH bending and deformation between -1290 and -1400 cm^{-1}, CH_2 scissoring and bending, CH_3 bending between -1400 and -1480 cm^{-1}, and C=C stretching at -1650 cm^{-1} are assigned to lipids. The phenylalanine peak at -1002 cm^{-1}, the amide III between -1200 and -1300 cm^{-1} and the amide I peak at -1650 cm^{-1} are instead assigned to proteins. Finally, the PO_2^- stretching peak between -1060 and -1095 cm^{-1} is assigned to nucleic acids. The C-H stretching region between -3150 and -2750 cm^{-1} contains instead overlapping vibrations arising from CH, CH_2, and CH_3 groups abundant in most biological compounds. We note here that, although most of these peaks are indistinctive of the class of molecules, vibrations specific to lipids are found in the lower wavenumbers spectral region below -2875 cm^{-1} [144], and peaks specific of amino acids have been assigned in the high wavenumbers region above -2930 cm^{-1} [102].

The spectra retrieved from the sections of different thickness were qualitatively similar, although the intensity of the collected signal was consistently lower for the thinner sections. This prevented the accurate determination of the spectrum in the fingerprint region for the 5 μm thick samples due to the small signal to noise ratio. Hence, for these samples, only the C-H stretching part of the spectrum was taken into account for the following analysis. As the axial resolution of the instrument is smaller than the thickness of the samples, the same response should be expected from both the 5 and 20 μm sections. We assume that the difference is caused by experimental factors. Specifically, the vertical position of the focus in the center of the tissue is determined with respect with the surface of the glass support, identified by the disappearance of the non-resonant response while moving the position of the focus. The accuracy of this procedure is also affected by the vertical resolution of the instrument, inducing a potential error in focusing the beams in the middle of the tissue. Also, CARS measurements are performed on the sections of the tissues kept at room temperature after letting the sample reach thermal equilibrium for one hour. As the tissue is not kept hydrated during this procedure, it is likely that, due to dehydration, the effective thickness of the sections is smaller than its

nominal value.

The large response obtained in the C-H stretching region of the retrieved CARS spectra can be used to obtain unspecific maps of the morphology of the tissue by integrating the response between -3020 and -2850 cm^{-1}. Fig. 7.3 (A) and Fig. 7.4 (A) show the CARS map of corresponding areas in the 20 and 5 μm sections of the muscle, respectively. In the image relative to the 20 μm sample, the individual cells are visible, their shape perfectly identical to the corresponding brightfield image (Fig. 7.1 (B)). The cells expected to present overexpression of PLIN5 (modified) and the ones unaffected by the electroporation procedure (unmodified) appear different also in terms of the features of the distribution of CH groups in the sample. The response of the unmodified group of cells is homogeneous, without any characteristic element. The response of the modified cells instead presents large spatial variations. Both high and low intensity features are visible inside the cells, with either round or elongated shape. The sarcolemmal edges appear as hypointense lines around the cells, also providing the contour to intercellular areas giving low CARS response. Inside the cell at the center of the image, two large dark features are present. We believe the sample was damaged at this location by laser illumination. Similar considerations hold for the description of the CARS map obtained from the 5 μm section. Here, some high intensity nearly-circular features are also visible in the unmodified cells, possibly related to the subdivision of the cell in myofibrils.

The CARS maps allow us to obtain the morphology of the sample in terms of local concentration of CH-rich molecules in the tissue. In order to find an actual correspondence with specific molecular classes, further analysis of the hyperspectral dataset is required.

7.3.3 PCA OF THE MUSCLE TISSUE CARS DATA

Hyperspectral CARS datasets measured in the sections of the muscle tissue were investigated with Principal Component Analysis in order to evaluate the chemical signatures contained in the vibrational spectra. We present separately the results obtained from the measurements performed on sections of the tissue with different thickness.

MUSCLE SECTION OF 20 μm THICKNESS. The first three positive and negative scores maps calculated by PCA of the 20 μm section of the tissue are presented in Fig. 7.5. The positive scores map corresponding to the first principal component (+1) shows a uniformly intense image of the tissue with dark areas present at the edges of the cells and, locally, inside the modified cells. These dark areas appear bright in the complementary negative map (-1) allowing us to better identify their position in the sample. Comparison with the C-H CARS map in Fig. 7.3 (A) shows that the -1 map highlights the position of the sample where the overall intensity of the measured CARS signal was lower. This normalizing character of the first component is sometime found as the outcome of PCA when large differences in the intensity of the response are present in the original data. In this case, the first component is proportional to the mean spectrum of

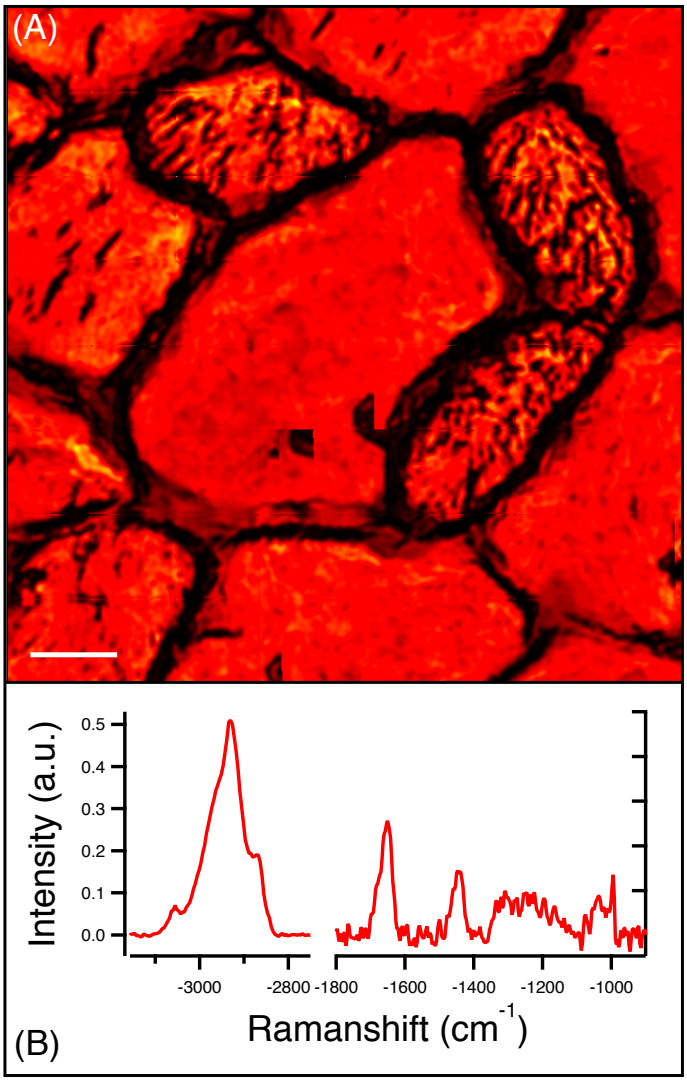

FIGURE 7.3. (A) CARS image of a region of 120 × 120 μm^2 of a 20 μm section of the muscle tissue. The intensity values in the image are obtained by integrating the CARS response between -3050 and -2850 cm^{-1} at each position in the sample. Scale bar: 20 microns. (B) Retrieved CARS spectrum at an arbitrary position within the muscle tissue. The C-H stretching region at high wavenumbers contains overlapping vibrations from the CH, CH_2, and CH_3 groups abundant both in lipids and proteins. The region at low wavenumbers (fingerprint region) contains a large number of peaks that have been assigned to specific vibrations of lipids, proteins and nucleic acids. The intermediate region of the spectrum is omitted due to the absence of vibrations specific to biological compounds.

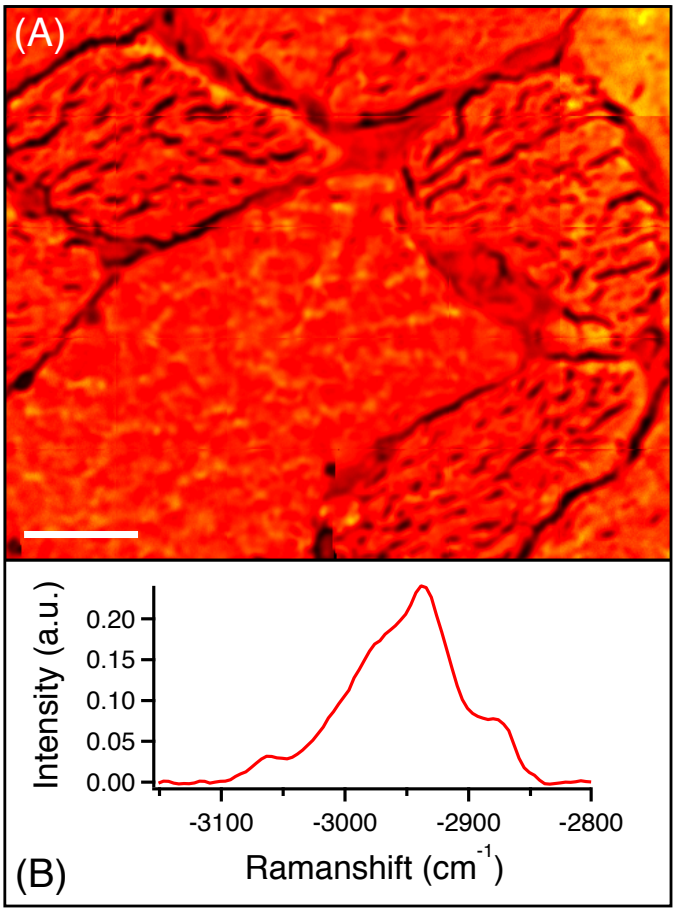

FIGURE 7.4. (A) CARS image of a region of 120×100 μm^2 of a 5 μm section of the muscle tissue. The intensity values in the image are obtained by integrating the CARS response between -3020 and -2850 cm^{-1} at each position in the sample. Scale bar: 20 microns. (B) C-H stretching region of the retrieved CARS spectrum at an arbitrary position in the sample.

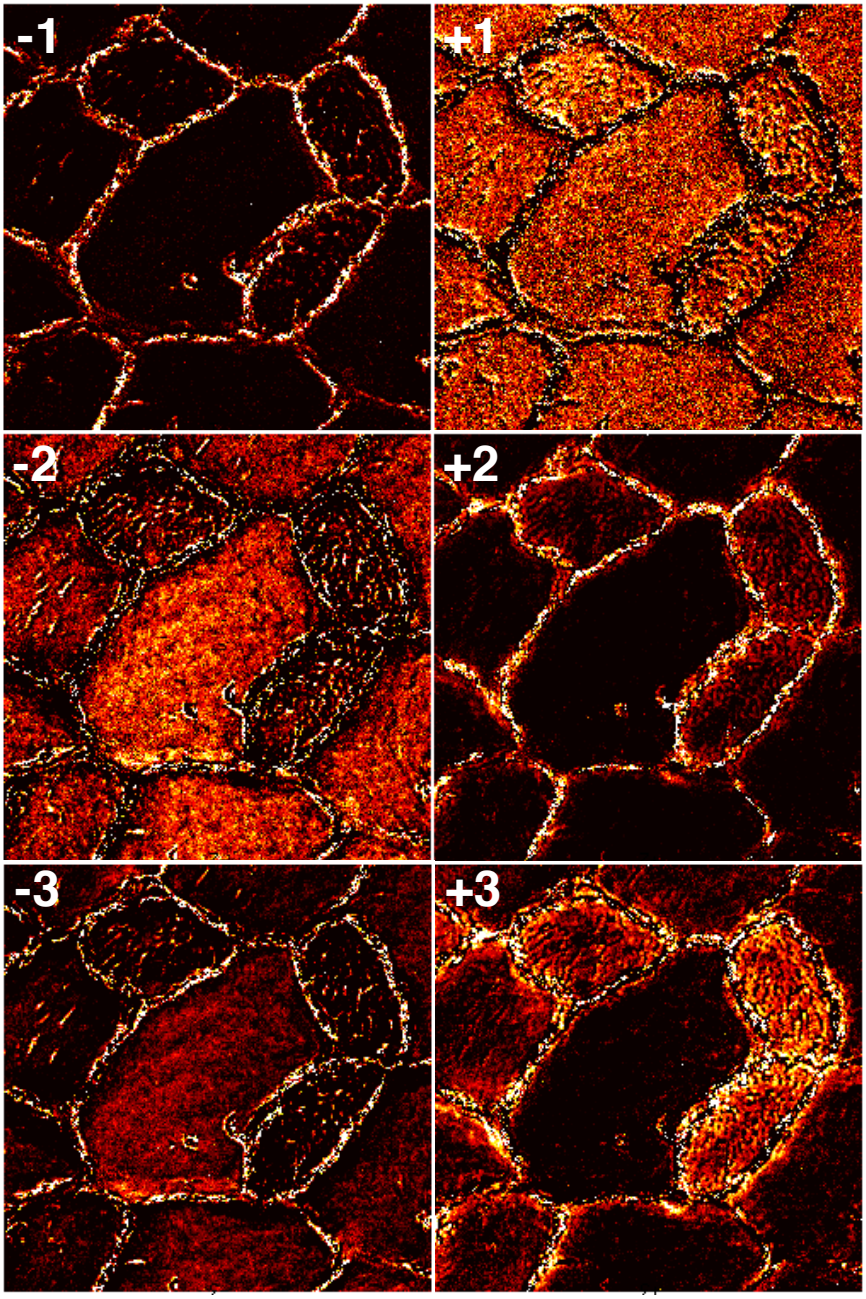

FIGURE 7.5. Positive and negative scores maps of the first three principal components calculated with PCA from the CARS hyperspectral dataset of the 20 μm thick section of the tissue.

the sample, and the second component effectively represents the larger variance due to differences in composition [54]. The scores maps corresponding to the second and third PCs qualitatively give the same results. The positive maps (+2 and +3) highlight again the spaces between adjacent cells, together with the intracellular region of the modified cells. Here, a collection of many individual round features is found. The scores values inside the unmodified cells are instead uniform and small in value. The negatives maps (-2 and -3) highlight instead homogeneously the region inside the unmodified cells, and elongated shapes of high intensity are found in the modified cells next to a low intensity background. The main difference in the maps of the second and the third PCs is the contrast in the images, found to be larger for the third component.

As the analytic form of the first three components (data not shown) provides insufficient indications to give a chemical interpretation of the scores maps, we can only provide a tentative interpretation based on the preliminary knowledge on muscles tissues in presence of local overexpression of the protein PLIN5 [13]. We suggest that the round features in the positive second and third scores maps represents the numerous lipid droplets present in the modified cells as a result of the overexpression of PLIN5. This is plausible as also the lipid-rich sarcolemmal edges of the cells are visible in the maps. Large lipid droplets are not known to be formed in the unmodified cells that then appear dark in the images. The negative maps are complementary and mutually exclusive with the positive scores maps. Hence, at this stage we can assume that the lipid-poor sarcoplasm is identified by negative scores values. However, the presence of high intensity features in the proximity of the cell membranes and inside the modified cells cannot be justified at this point simply by the absence of lipid aggregations. In order to find a preliminary explanation to these features, further analysis of the PCA results was required.

Hierarchical Cluster Analysis (HCA, see Paragraph 2.3) was performed on the hyperspectral dataset to cluster together the CARS spectral points with larger similarities. HCA found six spectral clusters in the data of the 20 μm section of the tissue. Scores maps were calculated for each of the clusters, representing the importance of the cluster at the different locations in the sample. Interestingly, these spectral clusters could be further associated together in two groups when the corresponding scores maps were found to be identical. The scores map representative of the first group is presented in Fig. 7.6 (A). The image resembles closely the positive scores map of the second and third PCs of Fig. 7.5. Round high intensity features are visible in the modified cells with higher definition compared to the PCA maps, and the sarcolemmal edges are again visible. A number of round features with lower intensity compared to the features found inside the modified cells are also present in the unmodified cells. In order to understand the chemical meaning of this map, we report the spectral intervals identified by the three spectral clusters belonging to this group: from -2896 to -2863 cm^{-1}, from -2863 to -2834 cm^{-1}, and finally from -1660 to -1613 and from -1491 to -1403 cm^{-1}. The spectral region identified by the first two clusters contains the CH_2 and CH_3 symmetric stretches, and the third region contains the CH_2 scissoring and bending, CH_3 bending, and C=C stretching

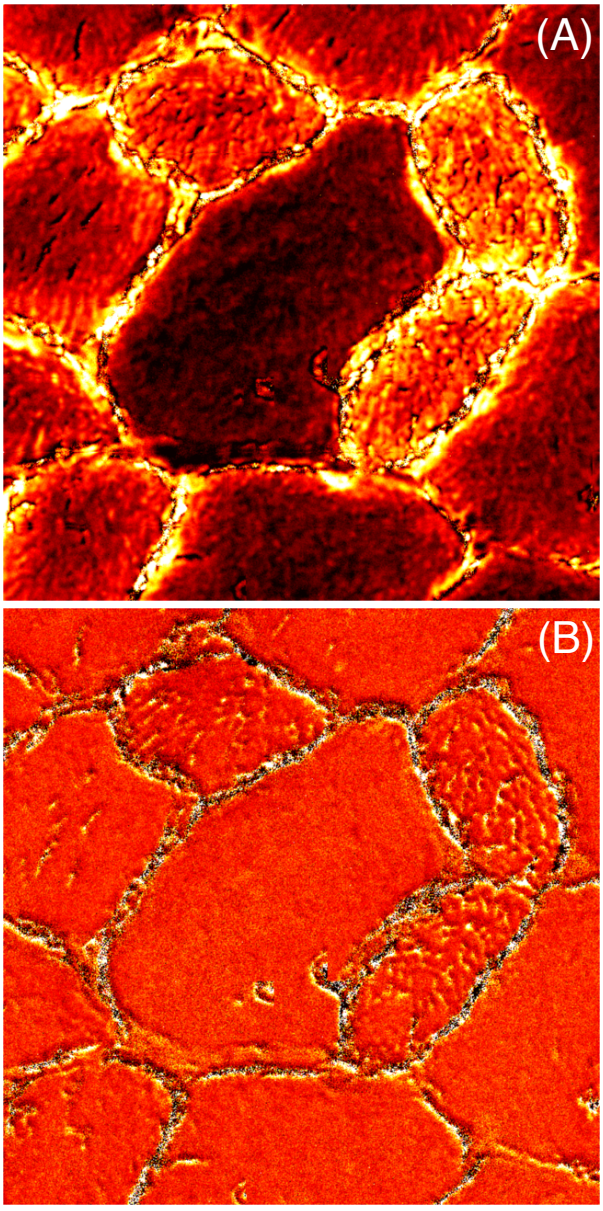

FIGURE 7.6. HCA scores maps calculated from the CARS hyperspectral dataset of the 20 μm thick section of the tissue. (A) Scores maps representing three spectral clusters: -2896 to -2863 cm^{-1}, -2863 to -2834 cm^{-1}, -1660 to -1613 and -1491 to -1403 cm^{-1}. (B) Scores maps representing three spectral clusters: -3042 to -3005 cm^{-1}, -1356 to -1136 cm^{-1}, and -1003 to -1000 cm^{-1}.

vibrations. Hence, all the bands found in the first group of clusters are assigned to lipids. We can then conclude that the scores map in panel (A) is likely to image the lipid aggregations in the tissue.

The scores map representative of the second group of spectral clusters is shown in Fig. 7.6 (B). Here, the response is uniform in the sarcoplasm of all cells, irrespective of their modified or unmodified status. Modified cells present additional intracellular features of high intensity with elongated shape. The spectral clusters of this group contain the phenylalanine peak at -1002 cm^{-1}, the amide III peak between -1200 and -1300 cm^{-1} and the part of the C-H spectrum assigned to proteins. Part of the spectral region identified by the clusters cannot be directly related to proteins, hence we cannot provide a conclusive description of the chemical composition of the areas of the tissues visualized in the image. Based on previous results on this tissue, it is known that large mitochondria are present in the cells overexpressing PLIN5 in the vicinity of LDs. The high intensity features in the figure could then represent the mitochondria. In order to confirm this hypothesis, immunofluorescence experiments providing the localization of mitochondria in the same tissue section used for the CARS experiments would be required. Unfortunately, at present we have obtained reliable immunostaining results only from separate sections of the tissue, preventing direct validation of the results.

MUSCLE SECTION OF 5 μm THICKNESS. The first three positive and negative scores maps calculated by PCA of the 5 μm section of the tissue are presented in Fig. 7.7, and the corresponding analytical form of the components is shown in Fig. 7.8. The first positive scores map (+1) highlights the sarcolemmal edges and distinct intracellular features inside the modified cells. Several of these high intensity elements present a round shape compatible with their identification with lipid droplets. The unmodified cells that appeared dark in the positive map show instead high response in the negative map, with nearly uniform scores values. Inside the modified cells, high intensity lines are instead present on a low intensity background. The corresponding fist PC in Fig. 7.8 (A) presents two positive peaks at -2855 and -2895 cm^{-1}, with an intermediate relative dip at -2871 cm^{-1}. The negative peaks are instead centered at -2946, -2984 and-3060 cm^{-1}. The positive peaks identify vibrations specific of lipids as discussed in Paragraph 7.3.2, supporting the interpretation of the +1 scores maps to visualize LDs in the modified cells. The negative peaks in the region of the C-H part of the spectrum have also been discussed previously in this thesis to be predominantly related to the presence of proteins.

The -2 and +3 scores maps show similar, featureless images of the cells that present low scores values. The +2 and -3 scores maps also look similar, with high intensity lines present inside the modified cells at the same locations as in the -1 map. However, here the unmodified cells are characterized by low signal and features in the intracellular areas appear bright. The bright elements in the vicinity of the sarcolemmal borders present some mislocalization between the +2 and -3 maps, their shape and localization in the -3 map being closely reminiscent of the cell nuclei (cfr. Fig. 7.2). Immunoistochemistry experiments

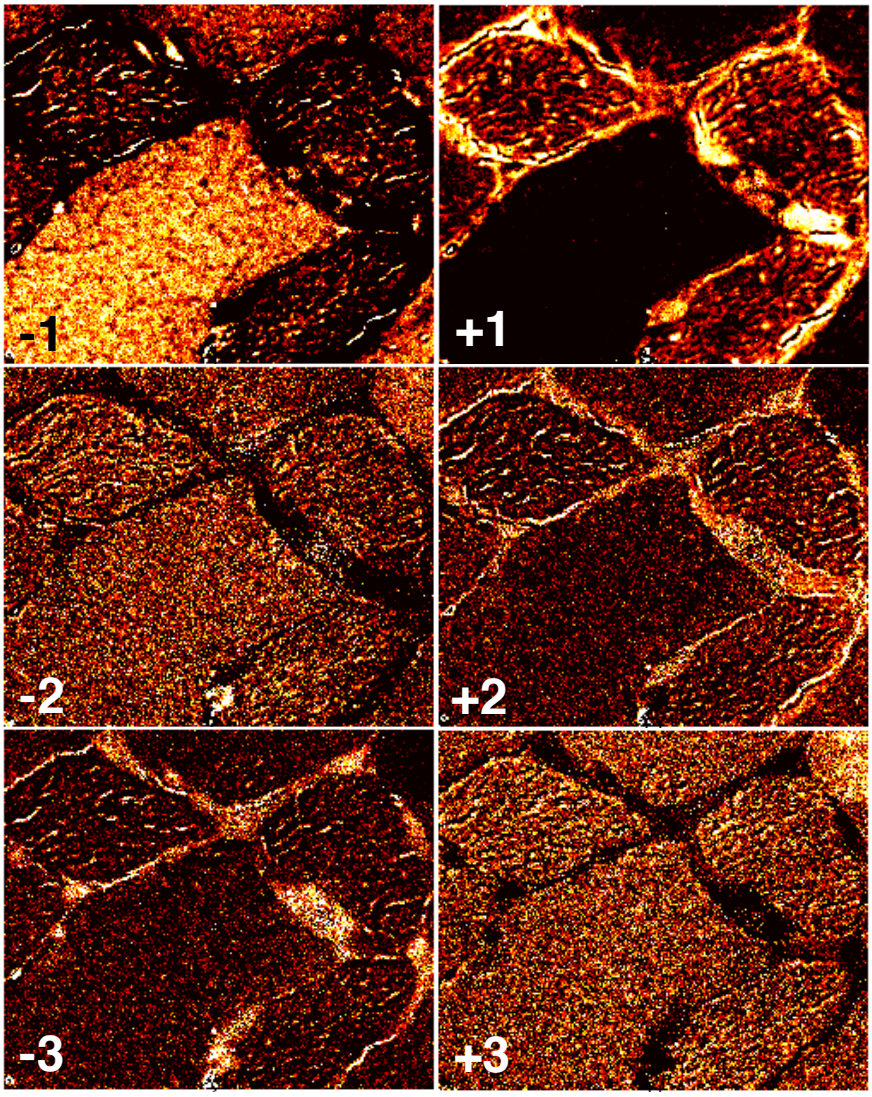

FIGURE 7.7. Positive and negative scores maps of the first three principal components calculated with PCA from the CARS hyperspectral dataset of the 5 μm thick section of the tissue.

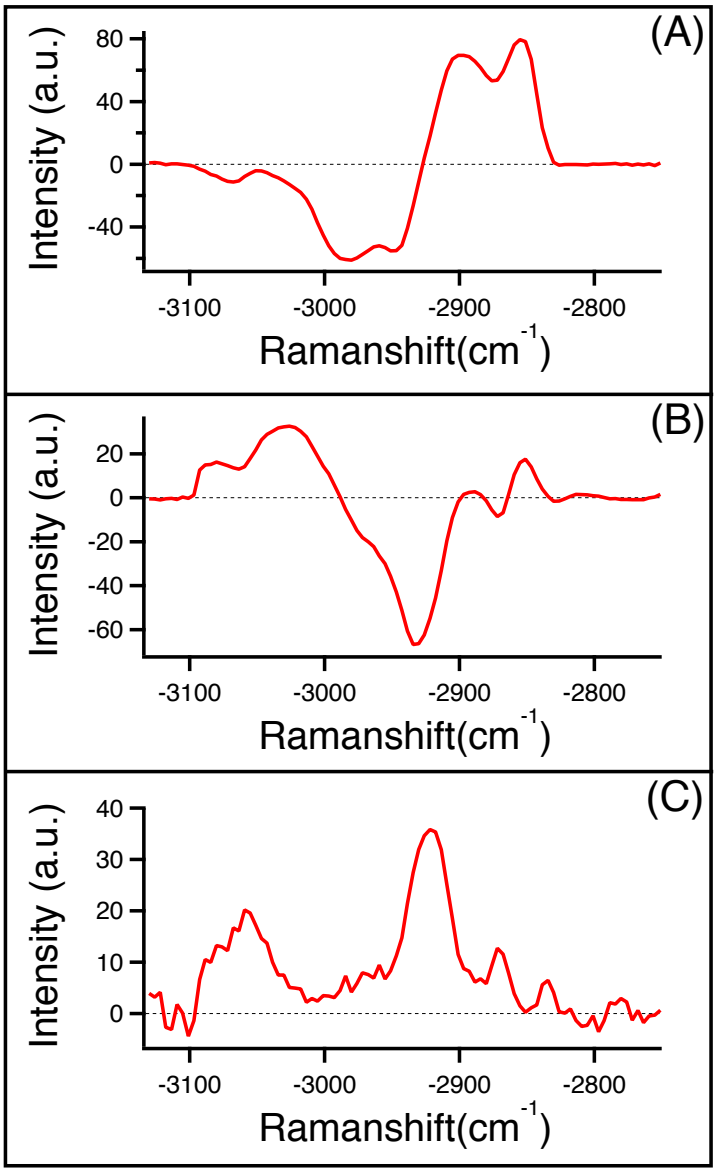

FIGURE 7.8. Spectra of first (A), second (B) and third (C) principal component calculated with PCA from the CARS hyperspectral dataset of the 5 μm thick section of the tissue.

on the same section of the tissue would also in this case be helpful to confirm this interpretation. The corresponding second and third PCs are presented in Fig. 7.8 (B) and (C), respectively. The second PC presents positive peaks at -2850, -2880, -3030, and -3080 cm^{-1}, and negative peaks at -2871, and -2930 cm^{-1} with a shoulder at -2971 cm^{-1}. The third component is more noisy than the other two, and contains only positive peaks centred at -2834, -2871, -2920, and -3050. The considerations discussed above on the lipid and protein origin of the peaks located in the low and high wavenumbers region of the C-H spectrum, respectively, were not sufficient to provide a meaningful explanation of the maps obtained by PCA for the second and third components. Further analysis of the PCA results was hence necessary also for better interpreting the CARS results from the 5 μm section of the tissue.

HSA was performed on the CARS data measured in the 5 μm thick section of the muscle tissue. The analysis found six spectral clusters, the first five of which ranging over the entire spectral region between -2846 to -2970 cm^{-1}. The scores maps calculated for the first five clusters are presented in Fig. 7.9. The scores maps of the first two clusters (A and B) contain the spectral region from -2846 to -2863 cm^{-1} and from -2880 to -2905 cm^{-1}. This region of the spectrum contains the CH vibrations specific of lipids. In the two maps the modified and unmodified cells can be distinguished based on the difference in intensity in the sarcoplasm. Perfectly defined round elements are present in the modified cells, indicating the presence of LDs. The sarcolemmal edges are also clearly visible in the figures. The score map of the third cluster is shown in panel (C). This cluster contains the vibrations from -2913 to -2917 cm^{-1}, intermediate between the portions of the spectrum specific to lipids and proteins. The last two scores maps (D and E) contain the spectral region from -2921 to -2942 cm^{-1} (D), and from -2946 to -2970 (E), respectively, indicating a dominant protein character of the resonances. The intensity in the unmodified cells is large and uniform. The intensity drops slightly in the sarcoplasm of the modified cells, where dark round features are also visible. These features colocalize with the high intensity elements found in the scores maps of the first two clusters (A and B) identifying the LDs.

The scores map of the last spectral cluster (-3013 to -3046 cm^{-1}) is shown in Fig. 7.10. The scores in the sarcoplasms of the modified and unmodified celles present similar values. Bright elongated elements are present in the modified cells, similar to the features found in the scores maps calculated by PCA and hypothesized to identify mitochondria. Similarly, also the features in the proximity of the sarcolemma visible in the -3 scores map are as well present in the last cluster map. It was previously discussed that these features might correspond to the nuclei of the cells. Although mitochondria and cell nuclei present very different chemical composition, we note that mitochondria also contain some DNA. Also in this case, validating experiments with immunohistochemistry are required to confirm this preliminary finding.

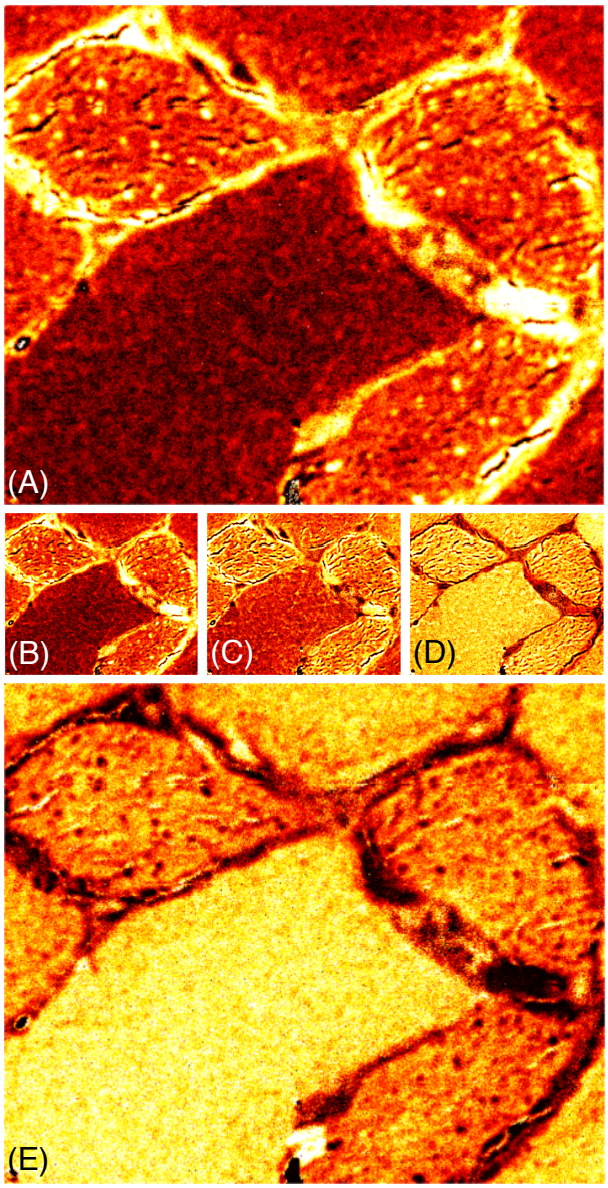

FIGURE 7.9. HCA scores maps calculated from the CARS hyperspectral dataset of the 20 $/mum$ thick section of the tissue. Scores maps representing the spectral cluster from -2846 to -2863 cm^{-1} (A), from -2880 to -2905 cm^{-1} (B), from -2913 to -2917 cm^{-1} (C), from -2921 to -2942 cm^{-1} (D), and from -2946 to -2970 (E).

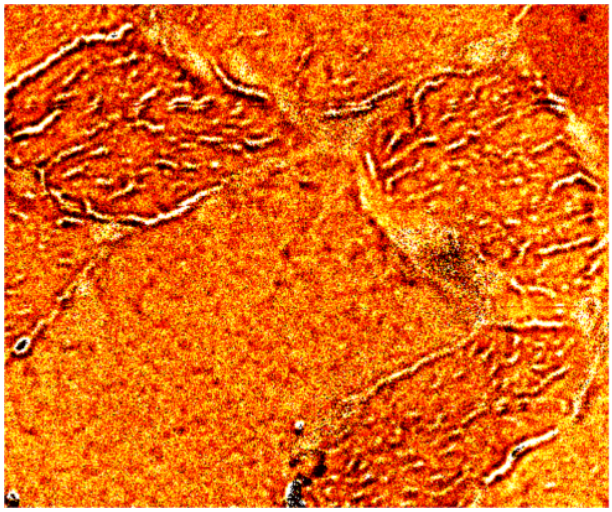

FIGURE 7.10. HCA scores map (CARS dataset of the 20 /*mum* thick section of the tissue) representing the spectral cluster from -3013 to -3046 cm^{-1}.

7.4 CONCLUSIONS

In this chapter we have presented the application of CARS spectro-microscopy to provide label free identification of biological components in muscle tissues with chemical specificity. We used CARS to study muscles were genetic modification induces locally the overexpression of the LD coating protein PLIN5. The overexpression of the protein is known to increase the storage of intra myocellular lipids.

We found that the interpretation of the CARS hyperspectral dataset using multivariate analysis methods (PCA and HCA) allowed the unambiguous identification of lipid droplets in sections of the muscle tissue with different thickness. These results could be used as a starting point for follow up studies where the vibrational signature can be employed to determine *e.g.* the degree of order and saturation of individual LDs. Also, preliminary results indicate that CARS might be able to visualize mitochondria in the tissue. This result, requiring validation with immunohistochemistry, is, to the best of our knowledge, the first example of label free visualization of mitochondria in tissues.

Bibliography

1. M.J. Adams. *Chemometrics in Analytical Spectroscopy*. Royal Society of Chemistry, Cambridge, 2004.

2. S. S. Agasti, A. Chompoosor, C.C. You, P. Ghosh, C.K. Kim, and V.M. Rotello. Photoregulated release of caged anticancer drugs from gold nanoparticles. *Journal of the American Chemical Society*, 131(16):5728, 2009.

3. C. Aguer, J. Mercier, C. Y. W. Man, L. Metz, S. Bordenave, K. Lambert, E. Jean, L. Lantier, L. Bounoua, J. F. Brun, E. R. de Mauverger, F. Andreelli, M. Foretz, and M. Kitzmann. Intramyocellular lipid accumulation is associated with permanent relocation ex vivo and in vitro of fatty acid translocase (fat)/cd36 in obese patients. *Diabetologia*, 53(6):1151–1163, 2010.

4. B. Alberts, D. Bray, J. Lewis, M. Raff, K. Roberts, and J. D. Watson. *Molecular Biology of the cell*. Garland publishing inc. New York, 1994.

5. A.S. Arbab and J.A. Frank. Cellular mri and its role in stem cell therapy. *Regenerative Medicine*, 3(2):199–215, 2008.

6. S. Aryal, J.J. Grailer, S. Pilla, D.A. Steeber, and S. Gong. Doxorubicin conjugated gold nanoparticles as water-soluble and ph-responsive anticancer drug nanocarriers. *Journal of Materials Chemistry*, 19(42):7879–7884, 2009.

7. G. Bergner, S. Chatzipapadopoulos, D. Akimov, B. Dietzek, D. Malsch, T. Henkel, S. Schluecker, and J. Popp. Quantitative cars microscopic detection of analytes and their isotopomers in a two-channel microfluidic chip. *Small*, 5(24):2816–2818, 2009.

8. M. R. Beversluis, A. Bouhelier, and L. Novotny. Continuum generation from single gold nanostructures through near-field mediated intraband transitions. *Physical Review B*, 68(11):115433, 2003.

9. N. Billinton and A. W. Knight. Seeing the wood through the trees: A review of techniques for distinguishing green fluorescent protein from endogenous autofluorescence. *Analytical Biochemistry*, 291(2):175–197, 2001.

10. N. Bloembergen. *Laser spectroscopy IV*. Springer, 1979.

11. N. I. Bohnen, M. Charron, J. Reyes, W. Rubinstein, S. C. Strom, D. Swanson, and R. Towbin. Use of indium-111-labeled hepatocytes to determine the biodistribution of transplanted hepatocytes through portal vein infusion. *Clinical Nuclear Medicine*, 25(6):447–450, 2000.

12. M. Bosma, S. Kersten, M. K. C. Hesselink, and P. Schrauwen. Re-evaluating lipotoxic triggers in skeletal muscle: Relating intramyocellular lipid metabolism to insulin sensitivity. *Progress In Lipid Research*, 51(1):36–49, 2012.

13. M. Bosma, R. Minnaard, L. M. Sparks, G. Schaart, M. Losen, M. H. de Baets, H. Duimel, S. Kersten, P. E. Bickel, P. Schrauwen, and M. K. C. Hesselink. The lipid droplet coat protein perilipin 5 also localizes to muscle mitochondria. *Histochemistry and Cell Biology*, 137(2):205–216, 2012.

14. R. W. Boyd. *Nonlinear Optics, third edition.* Elsevier, 2008.

15. C. Brackmann, A. Bengtsson, M.L. Alminger, U. Svanberg, and A. Enejder. Visualization of beta-carotene and starch granules in plant cells using cars and shg microscopy. *Journal of Raman Spectroscopy*, 42(4):586–592, 2011.

16. C. Brackmann, J.O. Dahlberg, N.E. Vrana, C. Lally, P. Gatenholm, and A. Enejder. Non-linear microscopy of smooth muscle cells in artificial extracellular matrices made of cellulose. *Journal of Biophotonics*, 5(5-6):404–414, 2012.

17. C. Brackmann, B. Gabrielsson, F. Svedberg, A. Holmang, A.S. Sandberg, and A. Enejder. Nonlinear microscopy of lipid storage and fibrosis in muscle and liver tissues of mice fed high-fat diets. *Journal of Biomedical Optics*, 15(6):066008, 2010.

18. C. Brandenberger, C. Muehlfeld, Z. Ali, A.G. Lenz, Otmar S., W.J. Parak, P. Gehr, and B. Rothen-Rutishauser. Quantitative evaluation of cellular uptake and trafficking of plain and polyethylene glycol-coated gold nanoparticles. *Small*, 6(15):1669–1678, 2010.

19. P. Brandtzaeg. The increasing power of immunohistochemistry and immunocytochemistry. *Journal of Immunological Methods*, 216(1-2):49–67, 1998.

20. R. Bro and S. De Jong. A fast non-negativity-constrained least squares algorithm. *J. Chemometrics*, 11(5):393–401, 1997.

21. W. J. Brook, F. J. DiazBenjumea, and S. M. Cohen. Organizing spatial pattern in limb development. *Annual Review of Cell and Developmental Biology*, 12:161–180, 1996.

22. S. D. Brown, P. Nativo, J.A. Smith, D. Stirling, P. R. Edwards, B. Venugopal, D. J. Flint, J. A. Plumb, D. Graham, and N. J. Wheate. Gold nanoparticles for the improved anticancer drug delivery of the active component of oxaliplatin. *Journal of the American Chemical Society*, 132(13):4678–4684, 2010.

23. J. W. M. Bulte. In vivo mri cell tracking: Clinical studies. *American Journal of Roentgenology*, 193(2):314–325, 2009.

24. M. R. Bunow and I. W. Levin. Comment on the carbon-hydrogen stretching region of vibrational raman spectra of phospholipids. *Biochimica et Biophysica Acta (BBA) - Lipids and Lipid Metabolism*, 487(2):388–394, 1977.

25. J. Burris and T. J. McIlrath. Theoretical-study relating the 2-photon absorption cross-section to the susceptibility controlling 4-wave mixing. *Journal of the Optical Society of America B-optical Physics*, 2(8):1313–1317, 1985.

26. J. X. Chen, A. Volkmer, L. D. Book, and X. S. Xie. Multiplex coherent anti-stokes raman scattering microspectroscopy and study of lipid vesicles. *Journal of Physical Chemistry B*, 106(34):8493–8498, 2002.

27. Y. H. Chen, C. Y. Tsai, P. Y. Huang, M. Y. Chang, P. C. Cheng, C. H. Chou, D. H. Chen, C. R. Wang, A. L. Shiau, and C. L. Wu. Methotrexate conjugated to gold nanoparticles inhibits tumor growth in a syngeneic lung tumor model. *Molecular Pharmaceutics*, 4(5):713–722, 2007.

28. J. X. Cheng, A. Volkmer, and X. S. Xie. Theoretical and experimental characterization of coherent anti-stokes raman scattering microscopy. *Journal of the Optical Society of America B-optical Physics*, 19(6):1363–1375, 2002.

29. J. X. Cheng and X. S. Xie. Coherent anti-stokes raman scattering microscopy: Instrumentation, theory, and applications. *Journal of Physical Chemistry B*, 108(3):827–840, 2004.

30. C.H. Chien, W.W. Chen, J.T. Wu, and T.C. Chang. Label-free imaging of drosophila in vivo by coherent anti-stokes raman scattering and two-photon excitation autofluorescence microscopy. *Journal of Biomedical Optics*, 16(1):016012, 2011.

31. B. D. Chithrani and W. C. W. Chan. Elucidating the mechanism of cellular uptake and removal of protein-coated gold nanoparticles of different sizes and shapes. *Nano Letters*, 7(6):1542–1550, 2007.

32. B. D. Chithrani, A. A. Ghazani, and W. C. W. Chan. Determining the size and shape dependence of gold nanoparticle uptake into mammalian cells. *Nano Letters*, 6(4):662–668, 2006.

33. D. B. Chithrani, M. Dunne, J. Stewart, C. Allen, and D. A. Jaffray. Cellular uptake and transport of gold nanoparticles incorporated in a liposomal carrier'. *Nanomedicine-nanotechnology Biology and Medicine*, 6(1):161–169, 2010.

34. L. Chiu, M. Ando, and H.O. Hamaguchi. Study of the 'raman spectroscopic signature of life' in mitochondria isolated from budding yeast. *Journal of Raman Spectroscopy*, 41(1):2–3, 2010.

35. P. D. Chowdary, W. A. Benalcazar, Z. Jiang, D. M. Marks, S. A. Boppart, and M. Gruebele. High speed nonlinear interferometric vibrational analysis of lipids by spectral decomposition. *Analytical Chemistry*, 82(9):3812–3818, 2010.

36. W.W. Coblentz. *Investigations of Infra-red Spectra*. Carnegie Institute of Washington, D.C., 1905.

37. S. D. Conner and S. L. Schmid. Regulated portals of entry into the cell. *Nature*, 422(6927):37–44, 2003.

38. E. E. Connor, J. Mwamuka, A. Gole, C. J. Murphy, and M. D. Wyatt. Gold nanoparticles are taken up by human cells but do not cause acute cytotoxicity. *Small*, 1(3):325–327, 2005.

39. J. P. Couso, M. Bate, and A. Martinez-Arias. A wingless-dependent polar coordinate system in drosophila imaginal disks. *Science*, 259(5094):484–489, 1993.

40. S. G. Crich, L. Biancone, V. Cantaluppi, D. D. G. Esposito, S. Russo, G. Camussi, and S. Aime. Improved route for the visualization of stem cells labeled with a gd-/eu-chelate as dual (mri and fluorescence) agent. *Magnetic Resonance In Medicine*, 51(5):938–944, 2004.

41. M. J. Crow, G. Grant, J.M. Provenzale, and A. Wax. Molecular imaging and quantitative measurement of epidermal growth factor receptor expression in live cancer cells using immunolabeled gold nanoparticles. *American Journal of Roentgenology*, 192(4):1021–1028, 2009.

42. H. F. Cui, S. K. Vashist, K. Al-Rubeaan, J. H. T. Luong, and F. S. Sheu. Interfacing carbon nanotubes with living mammalian cells and cytotoxicity issues. *Chemical Research In Toxicology*, 23(7):1131–1147, 2010.

43. M. Cui, B. R. Bachler, and J. P. Ogilvie. Comparing coherent and spontaneous raman scattering under biological imaging conditions. *Optics Letters*, 34(6):773–775, 2009.

44. A. C. Curry, M. Crow, and A. Wax. Molecular imaging of epidermal growth factor receptor in live cells with refractive index sensitivity using dark-field microspectroscopy and immunotargeted nanoparticles. *Journal of Biomedical Optics*, 13(1):014022, 2008.

45. C. Dahmann and K. Basler. Compartment boundaries - at the edge of development. *Trends In Genetics*, 15(8):320–326, 1999.

46. H. E. Daldrup-Link, M. Rudelius, S. Metz, G. Piontek, B. Pichler, M. Settles, U. Heinzmann, J. Schlegel, R. A. J. Oostendorp, and E. J. Rummeny. Cell tracking with gadophrin-2: a bifunctional contrast agent for mr imaging, optical imaging, and fluorescence microscopy. *European Journal of Nuclear Medicine and Molecular Imaging*, 31(9):1312–1321, 2004.

47. J. P. R. Day, K. F. Domke, G. Rago, H. Kano, H. O. Hamaguchi, E. M. Vartiainen, and M. Bonn. Quantitative coherent anti-stokes raman scattering (cars) microscopy. *Journal of Physical Chemistry B*, 115(24):7713–7725, 2011.

48. J. P. R. Day, G. Rago, K. F. Domke, K. P. Velikov, and M. Bonn. Label-free imaging of lipophilic bioactive molecules during lipid digestion by multiplex coherent anti-stokes raman scattering microspectroscopy. *Journal of the American Chemical Society*, 132(24):8433–8439, 2010.

49. I. J. M. de Vries, W. J. Lesterhuis, J. O. Barentsz, P. Verdijk, J. H. van Krieken, O. C. Boerman, W. J. G. Oyen, J. J. Bonenkamp, J. B. Boezeman, G. J. Adema, J. W. M. Bulte, T. W. J. Scheenen, C. J. A. Punt, A. Heerschap, and C. G. Figdor. Magnetic resonance tracking of dendritic cells in melanoma patients for monitoring of cellular therapy. *Nature Biotechnology*, 23(11):1407–1413, 2005.

50. A. deJuan, M. Maeder, T. Hancewicz, L. Duponchel, and R. Tauler. *Chemometric tools for image analysis in Infrared and Raman spectroscopic imaging*. Wiley-VCH, Weinheim Germany, 2009.

51. J. P. Despres and I. Lemieux. Abdominal obesity and metabolic syndrome. *Nature*, 444(7121):881–887, 2006.

52. A. Dhawan, R. R. Mitry, and R. D. Hughes. Hepatocyte transplantation for liver-based metabolic disorders. *Journal of Inherited Metabolic Disease*, 29(2-3):431–435, 2006.

53. A. Dhawan, J. Puppi, R. D. Hughes, and R. R. Mitry. Human hepatocyte transplantation: current experience and future challenges. *Nature Reviews Gastroenterology & Hepatology*, 7(5):288–298, 2010.

54. M. Diem, K. Papamarkakis, J. Schubert, B. Bird, M. J. Romeo, and M. Miljkovic. The infrared spectral signatures of disease: Extracting the distinguishing spectral features between normal and diseased states. *Applied Spectroscopy*, 63(11):307A–318A, 2009.

55. V. Dixit, J. Van den Bossche, D. M. Sherman, D. H. Thompson, and R. P. Andres. Synthesis and grafting of thioctic acid-peg-folate conjugates onto au nanoparticles for selective targeting of folate receptor-positive tumor cells. *Bioconjugate Chemistry*, 17(3):603–609, 2006.

56. S. J. Dodd, M. Williams, J. P. Suhan, D. S. Williams, A. P. Koretsky, and C. Ho. Detection of single mammalian cells by high-resolution magnetic resonance imaging. *Biophysical Journal*, 76(1):Int Soc Magnet Resonance Med, 1999.

57. P. Dominguez-Gimenez, N. H. Brown, and M. D. Martin-Bermudo. Integrin-ecm interactions regulate the changes in cell shape driving the morphogenesis of the drosophila wing epithelium. *Journal of Cell Science*, 120(6):1061–1071, 2007.

58. M. B. Dowling, L. Li, J. Park, G. Kumi, A. Nan, H. Ghandehari, J. T. Fourkas, and P. DeShong. Multiphoton-absorption-induced-luminescence (mail) imaging of tumor-targeted gold nanoparticles. *Bioconjugate Chemistry*, 21(11):1968–1977, 2010.

59. M. D. Duncan, J. Reintjes, and T. J. Manuccia. Scanning coherent anti-stokes raman microscope. *Optics Letters*, 7(8):350–352, 1982.

60. N. J. Durr, T. Larson, D. K. Smith, B. A. Korgel, K. Sokolov, and A. Ben-Yakar. Two-photon luminescence imaging of cancer cells using molecularly targeted gold nanorods. *Nano Letters*, 7(4):941–945, 2007.

61. M. Eghtedari, A. V. Liopo, J. A. Copland, A. A. Oraevslty, and M. Motamedi. Engineering of hetero-functional gold nanorods for the in vivo molecular targeting of breast cancer cells. *Nano Letters*, 9(1):287–291, 2009.

62. M. S. Ehrenberg, A. E. Friedman, J. N. Finkelstein, G. Oberdoerster, and J. L. McGrath. The influence of protein adsorption on nanoparticle association with cultured endothelial cells. *Biomaterials*, 30(4):603–610, 2009.

63. I. H. El-Sayed, X. Huang, and M. A. El-Sayed. Selective laser photothermal therapy of epithelial carcinoma using anti-egfr antibody conjugated gold nanoparticles. *Cancer Letters*, 239(1):129–135, 2006.

64. A. Enejder, C. Brackmann, and F. Svedberg. Coherent anti-stokes raman scattering microscopy of cellular lipid storage. *Ieee Journal of Selected Topics In Quantum Electronics*, 16(3):506–515, 2010.

65. S. Eustis and M. A. El-Sayed. Why gold nanoparticles are more precious than pretty gold: Noble metal surface plasmon resonance and its enhancement of the radiative and nonradiative properties of nanocrystals of different shapes. *Chemical Society Reviews*, 35(3):209–217, 2006.

66. C. L. Evans, E. O. Potma, M. Puoris'haag, D. Cote, C. P. Lin, and X. S. Xie. Chemical imaging of tissue in vivo with video-rate coherent anti-stokes raman scattering microscopy. *Proceedings of the National Academy of Sciences of the United States of America*, 102(46):16807–16812, 2005.

67. C. L. Evans, X. Xu, S. Kesari, X. S. Xie, S. T. C. Wong, and G. S. Young. Chemically-selective imaging of brain structures with cars microscopy. *Optics Express*, 15(19):12076–12087, 2007.

68. Jr. Farese, R. V. and T. C. Walther. Lipid droplets finally get a little r-e-s-p-e-c-t. *Cell*, 139(5):855–860, 2009.

69. R. A. Farrer, F. L. Butterfield, V. W. Chen, and J. T. Fourkas. Highly efficient multiphoton-absorption-induced luminescence from gold nanoparticles. *Nano Letters*, 5(6):1139–1142, 2005.

70. R. A. Fisher and S. C. Strom. Human hepatocyte transplantation: Worldwide results. *Transplantation*, 82(4):441–449, 2006.

71. E. Fitzpatrick, R. R. Mitry, and A. Dhawan. Human hepatocyte transplantation: state of the art. *Journal of Internal Medicine*, 266(4):339–357, 2009.

72. C. Fleming, N I Cummings, C. Anastopoulos, and B L Hu. The rotating-wave approximation: consistency and applicability from an open quantum system analysis. *Journal of Physics A: Mathematical and Theoretical*, 43(40):405304, 2010.

73. S. Fraser, R. Keynes, and A. Lumsden. Segmentation in the chick-embryo hindbrain is defined by cell lineage restrictions. *Nature*, 344(6265):431–435, 1990.

74. D. Fristom and J.W. Fristom. *The metamorphic development of adult epidermis. In The development of Drosophila melanogaster.* Cold Spring Harbor Laboratory Press, New York, 1993.

75. Y. Fu, H. Wang, R. Shi, and J. X. Cheng. Second harmonic and sum frequency generation imaging of fibrous astroglial filaments in ex vivo spinal tissues. *Biophysical Journal*, 92(9):3251–3259, 2007.

76. K. Fujita and N. I. Smith. Label-free molecular imaging of living cells. *Molecules and Cells*, 26(6):530–535, 2008.

77. A. Furtado and R. Henry. Measurement of green fluorescent protein concentration in single cells by image analysis. *Analytical Biochemistry*, 310(1):84–92, 2002.

78. D. Gachet, F. Billard, N. Sandeau, and H. Rigneault. Coherent anti-stokes raman scattering (cars) microscopy imaging at interfaces: evidence of interference effects. *Optics Express*, 15(16):10408–10420, 2007.

79. A. Garcia-Bellido, P. Ripoll, and G. Morata. Developmental compartmentalization of wing disk of drosophila. *Nature-new Biology*, 245(147):251–253, 1973.

80. Garcia-Bellido.A. Changes in selective affinity following transdetermination in imaginal disc cells of drosophila melanogaster. *Experimental Cell Research*, 44(2-3):382, 1966.

81. P. Ghosh, G. Han, M. De, C. K. Kim, and V. M. Rotello. Gold nanoparticles in delivery applications. *Advanced Drug Delivery Reviews*, 60(11):1307–1315, 2008.

82. P. Ghosh, X. Yang, R. Arvizo, Z. J. Zhu, S. S. Agasti, Z. Mo, and V. M. Rotello. Intracellular delivery of a membrane-impermeable enzyme in active form using functionalized gold nanoparticles. *Journal of the American Chemical Society*, 132(8):2642–2645, 2010.

83. S. K. Ghosh and T. Pal. Interparticle coupling effect on the surface plasmon resonance of gold nanoparticles: From theory to applications. *Chemical Reviews*, 107(11):4797–4862, 2007.

84. J. D. Gibson, B. P. Khanal, and E. R. Zubarev. Paclitaxel-functionalized gold nanoparticles. *Journal of the American Chemical Society*, 129(37):11653–11661, 2007.

85. D. A. Giljohann, D. S. Seferos, P. C. Patel, J. E. Millstone, N. L. Rosi, and C. A. Mirkin. Oligonucleotide loading determines cellular uptake of dna-modified gold nanoparticles. *Nano Letters*, 7(12):3818–3821, 2007.

86. D. A. Giljohann, D.t S. Seferos, W. L. Daniel, M. D. Massich, P. C. Patel, and C. A. Mirkin. Gold nanoparticles for biology and medicine. *Angewandte Chemie-international Edition*, 49(19):3280–3294, 2010.

87. B. H. Goodpaster, J. He, S. Watkins, and D. E. Kelley. Skeletal muscle lipid content and insulin resistance: Evidence for a paradox in endurance-trained athletes. *Journal of Clinical Endocrinology & Metabolism*, 86(12):5755–5761, 2001.

88. B. H. Goodpaster, R. Theriault, S. C. Watkins, and D. E. Kelley. Intramuscular lipid content is increased in obesity and decreased by weight loss. *Metabolism-clinical and Experimental*, 49(4):467–472, 2000.

89. J. Grimm, M. F. Kircher, and R. Weissleder. Cell tracking. principles and applications. *Radiologe*, 47(1):25–33, 2007.

90. S. Gupta. Hepatocyte transplantation. *Journal of Gastroenterology and Hepatology*, 17:S287–S293, 2002.

91. J. O. R. Gustafsson, M. K. Oehler, A. Ruszkiewicz, S. R. McColl, and P. Hoffmann. Maldi imaging mass spectrometry (maldi-ims)-application of spatial proteomics for ovarian cancer classification and diagnosis. *International Journal of Molecular Sciences*, 12(1):773–794, 2011.

92. H. T. Haigler, J. A. McKanna, and S. Cohen. Rapid stimulation of pinocytosis in human carcinoma-cells a-431 by epidermal growth-factor. *Journal of Cell Biology*, 83(1):82–90, 1979.

93. F. Hajizadeh and S. N. S. Reihani. Optimized optical trapping of gold nanoparticles. *Optics Express*, 18(2):551–559, 2010.

94. R. Hardman. A toxicologic review of quantum dots: Toxicity depends on physicochemical and environmental factors. *Environmental Health Perspectives*, 114(2):165–172, 2006.

95. T. Hashimoto, T. Yamada, and T. Yoko. Third-order nonlinear optical properties of sol-gel derived alpha-fe2o3, gamma-fe2o3, and fe3o4 thin films. *Journal of Applied Physics*, 80(6):3184–3190, 1996.

96. S. Haykin and S. Kesler. *Prediction-error filtering and maximum entropy spectral estimation*. Springer-Verlag, Berlin, 1983.

97. C. Heinrich, A. Hofer, A. Ritsch, C. Ciardi, S. Bernet, and M. Ritsch-Marte. Selective imaging of saturated and unsaturated lipids by wide-field cars-microscopy. *Optics Express*, 16(4):2699–2708, 2008.

98. T. Hellerer, C. Axaeng, C. Brackmann, P. Hillertz, M. Pilon, and A. Enejder. Monitoring of lipid storage in caenorhabditis elegans using coherent anti-stokes raman scattering (cars) microscopy. *Proceedings of the National Academy of Sciences of the United States of America*, 104(37):14658–14663, 2007.

99. T. D. Henning, O. Saborowski, D. Golovko, S. Boddington, J. S. Bauer, Y. Fu, R. Meier, H. Pietsch, B. Sennino, D. M. McDonald, and H. E. Daldrup-Link. Cell labeling with the positive mr contrast agent gadofluorine m. *European Radiology*, 17(5):1226–1234, 2007.

100. N. Himes, J. Y. Min, R. Lee, C. Brown, J. Shea, X. L. Huang, Y. F. Xiao, J. P. Morgan, D. Burstein, and P. Oettgen. In vivo mri of embryonic stem cells in a mouse model of myocardial infarction. *Magnetic Resonance In Medicine*, 52(5):1214–1219, 2004.

101. K. A. Hinds, J. M. Hill, E. M. Shapiro, M. O. Laukkanen, A. C. Silva, C. A. Combs, T. R. Varney, R. S. Balaban, A. P. Koretsky, and C. E. Dunbar. Highly efficient endosomal labeling of progenitor and stem cells with large magnetic particles allows magnetic resonance imaging of single cells. *Blood*, 102(3):867–872, 2003.

102. N. K. Howell, G. Arteaga, S. Nakai, and E. C. Y. Li-Chan. Raman spectral analysis in the c-h stretching region of proteins and amino acids for investigation of hydrophobic interactions. *Journal of Agricultural and Food Chemistry*, 47(3):924–933, 1999.

103. K. D. Irvine and C. Rauskolb. Boundaries in development: Formation and function. *Annual Review of Cell and Developmental Biology*, 17:189–214, 2001.

104. P. K. Jain, X. Huang, I. H. El-Sayed, and M. A. El-Sayed. Noble metals on the nanoscale: Optical and photothermal properties and some applications in imaging, sensing, biology, and medicine. *Accounts of Chemical Research*, 41(12):1578–1586, 2008.

105. I. M. Jazet, G. Schaart, A. Gastaldelli, E. Ferrannini, M. K. Hesselink, P. Schrauwen, J. A. Romijn, J. A. Maassen, H. Pijl, D. M. Ouwens, and A. E. Meinders. Loss of 50insulin-stimulated glucose disposal and skeletal muscle insulin signalling in obese insulin-treated type 2 diabetic patients. *Diabetologia*, 51(2):309–319, 2008.

106. I.T. Jolliffe. *Principal Component Analysis, 2nd ed.* Springer-Verlag, 2002.

107. M. Jurna, E. T. Garbacik, J. P. Korterik, J. L. Herek, C. Otto, and H. L. Offerhaus. Visualizing resonances in the complex plane with vibrational phase contrast coherent anti-stokes raman scattering. *Analytical Chemistry*, 82(18):7656–7659, 2010.

108. M. Jurna, J. P. Korterik, C. Otto, J. L. Herek, and H. L. Offerhaus. Background free cars imaging by phase sensitive heterodyne cars. *Optics Express*, 16(20):15863–15869, 2008.

109. T. Kaletta and M. O. Hengartner. Finding function in novel targets: C-elegans as a model organism. *Nature Reviews Drug Discovery*, 5(5):387–398, 2006.

110. Y. Kawashita, C. Guha, K. Yamanouchi, Y. Ito, Y. Kamohara, and T. Kanematsu. Liver repopulation: A new concept of hepatocyte transplantation. *Surgery Today*, 35(9):705–710, 2005.

111. T. Kempa, R. A. Farrer, M. Giersig, and J. T. Fourkas. Photochemical synthesis and multiphoton luminescence of monodisperse silver nanocrystals. *Plasmonics*, 1(1):45–51, 2006.

112. C. Kittel. *Introduction to Solid State Physics (4th ed.).* John Wiley and sons, 1971.

113. C. Kleusch, N. Hersch, B. Hoffmann, R. Merkel, and A. Csiszar. Fluorescent lipids: Functional parts of fusogenic liposomes and tools for cell membrane labeling and visualization. *Molecules*, 17(1):1055–1073, 2012.

114. S. Koenig, P. Krause, A. S. A. Hosseini, C. Dullin, M. Rave-Fraenk, S. Kimmina, A. L. Entwistle, R. M. Hermann, C. F. Hess, H. Becker, and H. Christiansen. Noninvasive imaging of liver repopulation following hepatocyte transplantation. *Cell Transplantation*, 18(1):69–78, 2009.

115. K. Krause, C. Schneider, K.H. Kuck, and K. Jaquet. Stem cell therapy in cardiovascular disorders. *Cardiovascular Therapeutics*, 28(5):e101–e110, 2010.

116. S. Kumar, J. Aaron, and K. Sokolov. Directional conjugation of antibodies to nanoparticles for synthesis of multiplexed optical contrast agents with both delivery and targeting moieties. *Nature Protocols*, 3(2):314–320, 2008.

117. P. A. Lawrence. Developmental biology - compartments in vertebrates. *Nature*, 344(6265):382–383, 1990.

118. P. A. Lawrence and G. Struhl. Morphogens, compartments, and pattern: Lessons from drosophila? *Cell*, 85(7):951–961, 1996.

119. T. T. Le, S. Yue, and J.X. Cheng. Shedding new light on lipid biology with coherent anti-stokes raman scattering microscopy. *Journal of Lipid Research*, 51(11):3091–3102, 2010.

120. D. E. Lee, S. Kehlenbrink, H. Lee, M. Hawkins, and J. S. Yudkin. Getting the message across: mechanisms of physiological cross talk by adipose tissue. *American Journal of Physiology-endocrinology and Metabolism*, 296(6):E1210–E1229, 2009.

121. W. M. Leevy, S. T. Gammon, J. R. Johnson, A. J. Lampkins, H. Jiang, M. Marquez, D. Piwnica-Worms, M. A. Suckow, and B. D. Smith. Non-invasive optical imaging of staphylococcus aureus bacterial infection in living mice using a bis-dipicolylamine-zinc(ii) affinity group conjugated to a near-infrared fluorophore. *Bioconjugate Chemistry*, 19(3):686–692, 2008.

122. R. Levy, N. T. K. Thanh, R. C. Doty, I. Hussain, R. J. Nichols, D. J. Schiffrin, M. Brust, and D. G. Fernig. Rational and combinatorial design of peptide capping ligands for gold nanoparticles. *Journal of the American Chemical Society*, 126(32):10076–10084, 2004.

123. L. Li, H. F. Wang, and J. X. Cheng. Quantitative coherent anti-stokes raman scattering imaging of lipid distribution in coexisting domains. *Biophysical Journal*, 89(5):3480–3490, 2005.

124. C.Y. Lin, V. Hovhannisyan, J.T. Wu, C.W. Lin, J.H. Chen, S.J. Lin, and C.Y. Dong. Label-free imaging of drosophila larva by multiphoton autofluorescence and second harmonic generation microscopy. *Journal of Biomedical Optics*, 13(5):050502, 2008.

125. C.Y. Lin, J.L. Suhalim, C.L. Nien, M.D. Miljkovic, M. Diem, J.V. Jester, and E.O. Potma. Picosecond spectral coherent anti-stokes raman scattering imaging with principal component analysis of meibomian glands. *Journal of Biomedical Optics*, 16(2):021104, 2011.

126. C.J. Liu, C.H. Wang, C.C. Chien, T.Y. Yang, S.T. Chen, W.H. Leng, C.F. Lee, K.H. Lee, Y. Hwu, Y.C. Lee, C.L. Cheng, C.S Yang, Y. J. Chen, J. H. Je, and G. Margaritondo. Enhanced x-ray irradiation-induced cancer cell damage by gold nanoparticles treated by a new synthesis method of polyethylene glycol modification. *Nanotechnology*, 19(29):295104, 2008.

127. W. Liu and J. A. Frank. Detection and quantification of magnetically labeled cells by cellular mri. *European Journal of Radiology*, 70(2):258–264, 2009.

128. Y. Liu, Young J. Lee, and M. T. Cicerone. Broadband cars spectral phase retrieval using a time-domain kramers-kronig transform. *Optics Letters*, 34(9):1363–1365, 2009.

129. J. Lodhia, G. Mandarano, N. J. Ferris, P. Eu, and S. F. Cowell. Development and use of iron oxide nanoparticles (part 1): Synthesis of iron oxide nanoparticles for mri. *Biomedical Imaging and Intervention Journal*, 6(2), 2010.

130. M. Maier, W. Kaiser, and J. A. Giordmaine. Backward stimulated raman scattering. *Phys. Rev.*, 177(2):580–599, 1969.

131. P. D. Maker and R. W. Terhune. Study of optical effects due to an induced polarization third order in the electric field strength. *Phys. Rev.*, 137(3A):A801–A818, 1965.

132. R. Malini, K. Venkatakrishna, J. Kurien, K. M. Pai, L. Rao, V. B. Kartha, and C. M. Krishna. Discrimination of normal, inflammatory, premalignant, and malignant oral tissue: A raman spectroscopy study. *Biopolymers*, 81(3):179–193, 2006.

133. D. Mandal, A. Maran, M. J. Yaszemski, M. E. Bolander, and G. Sarkar. Cellular uptake of gold nanoparticles directly cross-linked with carrier peptides by osteosarcoma cells. *Journal of Materials Science-materials In Medicine*, 20(1):347–350, 2009.

134. C. Matthaeus, B. Bird, M. Miljkovic, T. Chernenko, M. Romeo, and M. Diem. Infrared and raman microscopy in cell biology. *Biophysical Tools For Biologists, Vol 2: In Vivo Techniques*, 89:275–+, 2008.

135. Z. Medarova, P. Vallabhajosyula, A. Tena, N. Evgenov, P. Pantazopoulos, V. Tchipashvili, G. Weir, D. Sachs, and A. Moore. In vivo imaging of autologous islet grafts in the liver and under the kidney capsule in non-human primates. *Transplantation*, 87(11):1659–1666, 2009.

136. R. C. R. Meex, V. B. Schrauwen-Hinderling, E. Moonen-Kornips, G. Schaart, M. Mensink, E. Phielix, T. van de Weijer, J. P. Sels, P. Schrauwen, and M. K. C. Hesselink. Restoration of muscle mitochondrial function and metabolic flexibility in type 2 diabetes by exercise training is paralleled by increased myocellular fat storage and improved insulin sensitivity. *Diabetes*, 59(3):572–579, 2010.

137. J. Meyburg, A. M. Das, F. Hoerster, M. Lindner, H. Kriegbaum, G. Engelmann, J. Schmidt, M. Ott, A. Pettenazzo, T. Luecke, H. Bertram, G. F. Hoffmann, and A. Burlina. One liver for four children: First clinical series of liver cell transplantation for severe neonatal urea cycle defects. *Transplantation*, 87(5):636–641, 2009.

138. T. Meyerrose, S. Olson, S. Pontow, S. Kalomoiris, Y. Jung, G. Annett, G. Bauer, and J. A. Nolta. Mesenchymal stem cells for the sustained in vivo delivery of bioactive factors. *Advanced Drug Delivery Reviews*, 62(12):1167–1174, 2010.

139. M. Miljkovic, T. Chernenko, M.J. Romeo, B. Bird, C. Matthaeus, and M. Diem. Label-free imaging of human cells: algorithms for image reconstruction of raman hyperspectral datasets. *Analyst*, 135(8):2002–2013, 2010.

140. R. P. Millane. Phase retrieval in crystallography and optics. *Journal of the Optical Society of America A-optics Image Science and Vision*, 7(3):394–411, 1990.

141. M. Modo. Noninvasive imaging of transplanted cells. *Current Opinion In Organ Transplantation*, 13(6):654–658, 2008.

142. J. Moger, B. D. Johnston, and C. R. Tyler. Imaging metal oxide nanoparticles in biological structures with cars microscopy. *Optics Express*, 16(5):3408–3419, 2008.

143. M. H. Morgul, N. Raschzok, R. Schwartlander, F. W. Vondran, R. Michel, L. Stelter, J. Pinkernelle, A. Jordan, U. Teichgraber, and I. M. Sauer. Tracking of primary human hepatocytes with clinical mri: Initial results with tat-peptide modified superparamagnetic iron oxide particles. *International Journal of Artificial Organs*, 31(3):252–257, 2008.

144. Z. Movasaghi, S. Rehman, and I. U. Rehman. Raman spectroscopy of biological tissues. *Applied Spectroscopy Reviews*, 42(5):493–541, 2007.

145. M. Muller. *Introduction to confocal fluorescence microscopy*. Shaker Publishing, Maastricht, 2002.

146. M. Muller, J. M. Schins, and G. W. H. Wurpel. Shot-noise limited detection sensitivity in multiplex cars microscopy. *Multiphoton Microscopy In the Biomedical Sciences Iv*, 5323:SPIE; Bio–Rad Lab Inc; Carl Zeiss Inc; Chroma Technol Corp; CoherentEOLEOLInc; Nikon Inc; Omega Opt Inc; Spectra–Phys Inc, 2004.

147. H.S. Nalwa and S. Miyata. *Nonlinear optics of organic molecules and polymers*. CRC Press, Boca Raton, FL, 1997.

148. X. L. Nan, J. X. Cheng, and X. S. Xie. Vibrational imaging of lipid droplets in live fibroblast cells with coherent anti-stokes raman scattering microscopy. *Journal of Lipid Research*, 44(11):2202–2208, 2003.

149. X. L. Nan, E. O. Potma, and X. S. Xie. Nonperturbative chemical imaging of organelle transport in living cells with coherent anti-stokes raman scattering microscopy. *Biophysical Journal*, 91(2):728–735, 2006.

150. P. Nativo, I. A. Prior, and M. Brust. Uptake and intracellular fate of surface-modified gold nanoparticles. *Acs Nano*, 2(8):1639–1644, 2008.

151. B. L. Naylor, M. Picardo, R. Homan, and H. J. Pownall. Effects of fluorophore structure and hydrophobicity on the uptake and metabolism of fluorescent lipid analogs. *Chemistry and Physics of Lipids*, 58(1-2):111–119, 1991.

152. M. Okuno, H. Kano, P. Leproux, V. Couderc, J. P. R. Day, M. Bonn, and H.O. Hamaguchi. Quantitative cars molecular fingerprinting of single living cells with the use of the maximum entropy method. *Angewandte Chemie-international Edition*, 49(38):6773–6777, 2010.

153. World Health Organization. Obesity and overweight. Fact sheet N. 311, 2012.

154. G. F. Paciotti, L. Myer, D. Weinreich, D. Goia, N. Pavel, R. E. McLaughlin, and L. Tamarkin. Colloidal gold: A novel nanoparticle vector for tumor directed drug delivery. *Drug Delivery*, 11(3):169–183, 2004.

155. A. G. Pakhomov, D. Miklavcic, and M. S. Markov. *Advanced Electroporation Techniques in Biology and Medicine*. CRC Press, 2010.

156. S. H. Parekh, Y. J. Lee, K. A. Aamer, and M. T. Cicerone. Label-free cellular imaging by broadband coherent anti-stokes raman scattering microscopy. *Biophysical Journal*, 99(8):2695–2704, 2010.

157. P. C. Patel, D. A. Giljohann, D. S. Seferos, and C. A. Mirkin. Peptide antisense nanoparticles. *Proceedings of the National Academy of Sciences of the United States of America*, 105(45):17222–17226, 2008.

158. C. R. Patra, R. Bhattacharya, E. Wang, A. Katarya, J. S. Lau, S. Dutta, M. Muders, S. Wang, S. A. Buhrow, S. L. Safgren, M. J. Yaszemski, J. M. Reid, M. M. Ames, P. Mukherjee, and D. Mukbopadhyay. Targeted delivery of gemcitabine to pancreatic adenocarcinoma using cetuximab as a targeting agent. *Cancer Research*, 68(6):1970–1978, 2008.

159. C. Petibois. Imaging methods for elemental, chemical, molecular, and morphological analyses of single cells. *Analytical and Bioanalytical Chemistry*, 397:2051–2065, 2010.

160. J. Pinkernelle, U. Teichgraber, F. Neumann, L. Lehmkuhl, J. Ricke, R. Scholz, A. Jordan, and H. Bruhn. Imaging of single human carcinoma cells in vitro using a clinical whole-body magnetic resonance scanner at 3.0 t. *Magnetic Resonance In Medicine*, 53(5):1187–1192, 2005.

161. C. Pohling, T. Buckup, and M. Motzkus. Hyperspectral data processing for chemoselective multiplex coherent anti-stokes raman scattering microscopy of unknown samples. *Journal of Biomedical Optics*, 16(2):021105, 2011.

162. F. Port, M. Kuster, P. Herr, E. Furger, C. Baenziger, G. Hausmann, and K. Basler. Wingless secretion promotes and requires retromer-dependent cycling of wntless. *Nature Cell Biology*, 10(2):178–U48, 2008.

163. E. O. Potma, W. P. de Boeij, P. J. M. van Haastert, and D. A. Wiersma. Real-time visualization of intracellular hydrodynamics in single living cells. *Proceedings of the National Academy of Sciences of the United States of America*, 98(4):1577–1582, 2001.

164. E. O. Potma, C. L. Evans, and X. S. Xie. Heterodyne coherent anti-stokes raman scattering (cars) imaging. *Optics Letters*, 31(2):241–243, 2006.

165. E. O. Potma and X. S. Xie. Detection of single lipid bilayers with coherent anti-stokes raman scattering (cars) microscopy. *Journal of Raman Spectroscopy*, 34(9):642–650, 2003.

166. E.O. Potma. *"Tissue imaging with Coherent anti-Stokes Raman scattering microscopy" in Vibrational spectroscopic Imgaing for Biomedical Applications*. McGraw Hill, 2009.

167. S. Pujals, N. G. Bastus, E. Pereiro, C. Lopez-Iglesias, V. F. Punte, M. J. Kogan, and E. Giralt. Shuttling gold nanoparticles into tumoral cells with an amphipathic proline-rich peptide. *Chembiochem*, 10(6):1025–1031, 2009.

168. V.V. Pully and C. Otto. The intensity of the 1602 cm(-1) band in human cells is related to mitochondrial activity. *Journal of Raman Spectroscopy*, 40(5):473–475, 2009.

169. G. J. Puppels, F. F. M. Demul, C. Otto, J. Greve, M. Robertnicoud, D. J. Arndtjovin, and T. M. Jovin. Studying single living cells and chromosomes by confocal raman microspectroscopy. *Nature*, 347(6290):301–303, 1990.

170. J. Puppi and M. Modo. Use of magnetic resonance imaging contrast agents to detect transplanted liver cells. *Topics in Magnetic Resonance Imaging*, 20(2):113–120 10.1097/RMR.0b013e3181c0dfe4, 2009.

171. X. Qian, X.H. Peng, D. O. Ansari, Q. Yin-Goen, G. Z. Chen, D. M. Shin, L. Yang, A. N. Young, M. D. Wang, and S. Nie. In vivo tumor targeting and spectroscopic detection with surface-enhanced raman nanoparticle tags. *Nature Biotechnology*, 26(1):83–90, 2008.

172. A. Quaglia, S. C. Lehec, R. D. Hughes, R. R. Mitry, A. S. Knisely, S. Devereaux, J. Richards, M. Rela, N. D. Heaton, B. C. Portmann, and A. Dhawan. Liver after hepatocyte transplantation for liver-based metabolic disorders in children. *Cell Transplantation*, 17(12):1403–1414, 2008.

173. G. Rago, B. Bauer, F. Svedberg, L. Gunnarsson, M. B. Ericson, M. Bonn, and A. Enejder. Uptake of gold nanoparticles in healthy and tumor cells visualized by nonlinear optical microscopy. *Journal of Physical Chemistry B*, 115(17):5008–5016, 2011.

174. C. Raman and K. Krishnan. A new type of secondary radiation. *Nature*, 121:501, 1928.

175. N. Raschzok, M. H. Morgul, J. Pinkernelle, F. W. R. Vondran, N. Billecke, N. N. Kammer, G. Pless, M. K. Adonopoulou, C. Leist, L. Stelter, U. Teichgraber, R. Schwartlander, and I. M. Sauer. Imaging of primary human hepatocytes performed with micron-sized iron oxide particles and clinical magnetic resonance tomography. *Journal of Cellular and Molecular Medicine*, 12(4):1384–1394, 2008.

176. P.F. Renshaw, Owen C.S., Evans A.E., and Leigh H.S.J. Immunospecific nmr contrast agents. *Magnetic resonance imaging*, 4:351–358, 1986.

177. H. A. Rinia, M. Bonn, and M. Muller. Quantitative multiplex cars spectroscopy in congested spectral regions. *Journal of Physical Chemistry B*, 110(9):4472–4479, 2006.

178. H. A. Rinia, M. Bonn, M. Muller, and E. M. Vartiainen. Quantitative cars spectroscopy using the maximum entropy method: The main lipid phase transition. *Chemphyschem*, 8(2):279–287, 2007.

179. H. A. Rinia, K. N. J. Burger, M. Bonn, and M. Muller. Quantitative label-free imaging of lipid composition and packing of individual cellular lipid droplets using multiplex cars microscopy. *Biophysical Journal*, 95(10):4908–4914, 2008.

180. A. M. Schrand, J. J. Schlager, L. Dai, and S. M. Hussain. Preparation of cells for assessing ultrastructural localization of nanoparticles with transmission electron microscopy. *Nature Protocols*, 5(4):744–757, 2010.

181. S. Schwarz, F. Fernandes, L. Sanroman, M. Hodenius, C. Lang, U. Himmelreich, T. Schmitz-Rode, D. Schueler, M. Hoehn, M. Zenke, and T. Hieronymus. Synthetic and biogenic magnetite nanoparticles for tracking of stem cells and dendritic cells. *Journal of Magnetism and Magnetic Materials*, 321(10):1533–1538, 2009.

182. T. Seppanen-Laakso, I. Laakso, and R. Hiltunen. Analysis of fatty acids by gas chromatography, and its relevance to research on health and nutrition. *Analytica Chimica Acta*, 465(1-2):PII S0003–2670(20)00397–5, 2002.

183. B. Sepulveda, P. C. Angelome, L. M. Lechuga, and L. M. Liz-Marzan. Lspr-based nanobiosensors. *Nano Today*, 4(3):244–251, 2009.

184. C.E. Shannon. A mathematical theory of communication. *Bell System Technical Journal*, 27(3):379–423, 1948.

185. E. M. Shapiro, K. Sharer, S. Skrtic, and A. P. Koretsky. In vivo detection of single cells by mri. *Magnetic Resonance In Medicine*, 55(2):242–249, 2006.

186. E. M. Shapiro, S. Skrtic, and A. P. Koretsky. Sizing it up: Cellular mri using micron-sized iron oxide particles. *Magnetic Resonance In Medicine*, 53(2):329–338, 2005.

187. E. M. Shapiro, S. Skrtic, K. Sharer, J. M. Hill, C. E. Dunbar, and A. P. Koretsky. Mri detection of single particles for cellular imaging. *Proceedings of the National Academy of Sciences of the United States of America*, 101(30):10901–10906, 2004.

188. V. Shcheslavskiy, G. I. Petrov, S. Saltiel, A. Boyko, V. Y. Petrussevich, Y. M. Petrussevich, G. P. Petrova, and V. V. Yakovlev. Nonlinear optical spectroscopy of collagen transformation. *Multiphoton Microscopy In the Biomedical Sciences Iv*, 5323:SPIE; Bio–Rad Lab Inc; Carl Zeiss Inc; Chroma Technol Corp; CoherentEOLEOLInc; Nikon Inc; Omega Opt Inc; Spectra–Phys Inc, 2004.

189. R. Shukla, V. Bansal, M. Chaudhary, A. Basu, R. R. Bhonde, and M. Sastry. Biocompatibility of gold nanoparticles and their endocytotic fate inside the cellular compartment: A microscopic overview. *Langmuir*, 21(23):10644–10654, 2005.

190. M. N. Slipchenko, T. T. Le, H. Chen, and J..H Cheng. Compound raman microscopy for high-speed vibrational imaging and spectral. *Microscopy and Microanalysis*, 15:70–71, 2009.

191. M. Srinivas, P. A. Morel, L. A. Ernst, D. H. Laidlaw, and E. T. Ahrens. Fluorine-19 mri for visualization and quantification of cell migration in a diabetes model. *Magnetic Resonance In Medicine*, 58(4):725–734, 2007.

192. J. Sung, B.C. Chen, and S.H. Lim. Fast three-dimensional chemical imaging by interferometric multiplex coherent anti-stokes raman scattering microscopy. *J. Raman Spectrosc.*, 42(2):130–136, 2011.

193. W. Supatto, D. Debarre, B. Moulia, E. Brouzes, J. L. Martin, E. Farge, and E. Beaurepaire. In vivo modulation of morphogenetic movements in drosophila embryos with femtosecond laser pulses. *Proceedings of the National Academy of Sciences of the United States of America*, 102(4):1047–1052, 2005.

194. M. Suzuki, Y. Shinohara, Y. Ohsaki, and T. Fujimoto. Lipid droplets: size matters. *Journal of Electron Microscopy*, 60:S101–S116, 2011.

195. J.A. Swanson and C. Watts. Macropinocytosis. *Trends In Cell Biology*, 5(11):424–428, 1995.

196. B. Valerur. *Molecular fluorescence: principles and applications*. Wiley-VCH, Weinheim Germany, 2001.

197. G. van Meer, D. R. Voelker, and G. W. Feigenson. Membrane lipids: where they are and how they behave. *Nature Reviews Molecular Cell Biology*, 9(2):112–124, 2008.

198. E. W. VanStryland, M. A. Woodall, H. VanHerzeele, and M. J. Soileau. Energy band-gap dependence of 2-photon absorption. *Optics Letters*, 10(10):490–492, 1985.

199. O. P. Varnavski, M. B. Mohamed, M. A. El-Sayed, and T. Goodson. Relative enhancement of ultrafast emission in gold nanorods. *Journal of Physical Chemistry B*, 107(14):3101–3104, 2003.

200. E. M. Vartiainen. Phase retrieval approach for coherent anti-stokes-raman scattering spectrum analysis. *Journal of the Optical Society of America B-optical Physics*, 9(8):1209–1214, 1992.

201. E. M. Vartiainen, K. E. Peiponen, and T. Asakura. Phase retrieval in optical spectroscopy: Resolving optical constants from power spectra. *Applied Spectroscopy*, 50(10):1283–1289, 1996.

202. E. M. Vartiainen, H. A. Rinia, M. Muller, and M. Bonn. Direct extraction of raman line-shapes from congested cars spectra. *Optics Express*, 14(8):3622–3630, 2006.

203. A. Verma and F. Stellacci. Effect of surface properties on nanoparticle-cell interactions. *Small*, 6(1):12–21, 2010.

204. A. Volkmer, L. D. Book, and X. S. Xie. Time-resolved coherent anti-stokes raman scattering microscopy: Imaging based on raman free induction decay. *Applied Physics Letters*, 80(9):1505–1507, 2002.

205. A. Volkmer, J. X. Cheng, and X. S. Xie. Vibrational imaging with high sensitivity via epidetected coherent anti-stokes raman scattering microscopy. *Physical Review Letters*, 87(2):023901, 2001.

206. B. von Vacano, L. Meyer, and M. Motzkus. Rapid polymer blend imaging with quantitative broadband multiplex cars microscopy. *Journal of Raman Spectroscopy*, 38(7):916–926, 2007.

207. Y. Wang, C.Y. Lin, A. Nikolaenko, V. Raghunathan, and E. O. Potma. Four-wave mixing microscopy of nanostructures. *Adv. Opt. Photon.*, 3(1):1–52, 2011.

208. A. Wax and K. Sokolov. Molecular imaging and darkfield microspectroscopy of live cells using gold plasmonic nanoparticles. *Laser & Photonics Reviews*, 3(1-2):146–158, 2009.

209. J. P. Wilcoxon, J. E. Martin, F. Parsapour, B. Wiedenman, and D. F. Kelley. Photoluminescence from nanosize gold clusters. *Journal of Chemical Physics*, 108(21):9137–9143, 1998.

210. N. E. Wolins, B. K. Quaynor, J. R. Skinner, A. Tzekov, M. A. Croce, M. C. Gropler, V. Varma, A. Yao-Borengasser, N. Rasouli, P. A. Kern, B. N. Finck, and P. E. Bickel. Oxpat/pat-1 is a ppar-induced lipid droplet protein that promotes fatty acid utilization. *Diabetes*, 55(12):3418–3428, 2006.

211. W. P. Wuelfing, S. M. Gross, D. T. Miles, and R. W. Murray. Nanometer gold clusters protected by surface-bound monolayers of thiolated poly(ethylene glycol) polymer electrolyte. *Journal of the American Chemical Society*, 120(48):12696–12697, 1998.

212. D. Yelin and Y. Silberberg. Laser scanning third-harmonic-generation microscopy in biology. *Optics Express*, 5(8):169–175, 1999.

213. Y. Zhang, J. Yu, D. J. S. Birch, and Y. Chen. Gold nanorods for fluorescence lifetime imaging in biology. *Journal of Biomedical Optics*, 15(2):020504, 2010.

214. Y. G. Zheng, G. Holtom, and S. Colson. Multichannel multiphoton imaging of metal oxides nanoparticles in biological system. *Multiphoton Microscopy In the Biomedical Sciences Iv*, 5323:SPIE; Bio–Rad Lab Inc; Carl Zeiss Inc; Chroma Technol Corp; CoherentEOLEOLInc; Nikon Inc; Omega Opt Inc; Spectra–Phys Inc, 2004.

215. M. Zimmerley, R. A. McClure, B. Choi, and E.O. Potma. Following dimethyl sulfoxide skin optical clearing dynamics with quantitative nonlinear multimodal microscopy. *Applied Optics*, 48(10):Opt Soc Amer, 2009.

216. A. Zumbusch, G. R. Holtom, and X. S. Xie. Three-dimensional vibrational imaging by coherent anti-stokes raman scattering. *Physical Review Letters*, 82(20):4142–4145, 1999.

Summary

In this thesis we present a series of studies employing non-linear vibrational microscopy, in the form of Coherent anti-Stokes Raman Scattering (CARS) spectro-microscopy. The underlying motivation of this thesis was to explore the limits and demonstrate the technical feasibility of CARS imaging in a variety of biological systems. We begin with examples using CARS in conventional morphological microscopy and end with multivariate spectral analysis, thereby showing the additional information afforded in vibrational imaging that is unattainable with any other technique.

Microscopy is arguably the most invaluable tool in life science research, as it can provide insights into the local organization of biological systems, as well as the underlying biochemical interactions. Also, microscopy can be used to investigate the interaction of biological matter with inorganic particles, widely used in medical therapies both as labeling agents and as target-specific shuttles for drugs. The most prevalent imaging modality offering molecular specificity is fluorescence microscopy, which unlike CARS relies on electronic excitation rather than vibrational excitation to provide the contrast in the recorded images. Because of the necessity of electronic states, fluorescence often requires exogenous molecules attached to macromolecular species of interest. In contrast to fluorescence, CARS uses the inherent vibrational modes of molecules as contrast agent to access the local chemical composition of a biological sample. As vibrations are intrinsic to all molecules, exogenous labels are not required for CARS measurements. This inherent contrast is the crucial difference with fluorescence microscopy, and the main advantage when compared to it.

In CARS experiments, three photons interact with the sample, resulting in the emission of a fourth photon - the anti-Stokes photon. The CARS signal is resonantly enhanced when the frequency of a molecular vibration is matched by the frequency difference of two of the incoming photons. Due to the non-linear nature of the process, the response of the sample is collected from the tiny ($\sim 1\ \mu m^3$) region in the focal volume only, where the probability of a four-photon event is higher. This provides the technique with intrinsic sub-diffractive resolution and axial-sectioning capabilities. Higher resolution and larger response due to the resonant interaction are the main advantages of CARS spectro-microscopy compared to traditional vibrational techniques such as infrared or spontaneous Raman microscopy.

CARS microscopy is often used in the single line implementation (single frequency CARS), to provide a picture of the spatial distribution of an individual compound, or more accurately of an individual chemical group, in the sample. The other implementation is multiplex CARS, where a vibrational spectrum at

each location in the sample is obtained (hyperspectral CARS imaging). Hyperspectral imaging provides richer information as it contains the full vibrational fingerprint of the sample, though it comes at the price of longer acquisition times. Both experimental approaches have been used in this thesis, and are described in **chapter 3**.

The work presented in this thesis covers a number of selected biomedical topics, demonstrating the successful applicability of CARS spectro-microscopy. **Chapters 4** and **5** detail the study of inorganic particle uptake in living cells, which is of interest in medical therapeutics and diagnostics. In **chapter 4** we report on the visualization of Magnetic Resonance Imaging (MRI) contrast agents in living cells. Micrometer-sized iron oxide particles (MPIOs) are used as labels for cellular tracking by clinical MRI after cell transplantation. Our single frequency CARS experiments, employing a combination of resonant and non-resonant CARS responses, allowed us to determine the localization of MPIOs in living hepatoma cells. Specifically, we were able to visualize the morphology of individual cells by collecting the resonant response from the stretching vibrations of the CH bonds. Subsequently, we could localize MPIOs taken up by the cells with a second CARS measurements probing an off-resonant region of the spectrum, i.e. where biological molecules have no vibrations. MPIOs, which present a larger density of electrons compared to biological components, were clearly visible in both measurements, whereas the cells were visible in the resonant measurement only. Hence, an overlay of the two measurements provided the exact localization of individual MPIOs in the cells, which complements the MRI meso-scale localization. Using the intrinsic axial resolution of the technique, the position of the particles inside the cells could be determined in three dimensions. This is a particularly useful result as brightfield microscopy, commonly used to visually inspect the internalization process, is not able to distinguish along the axial direction the particles that have been internalized from those sitting outside the cell membrane. Our results suggest the possibility that MPIOs also penetrate cell nuclei.

In **chapter 5**, results on the uptake of gold nanoparticles (AuNPs) in healthy and tumor cells are reported. AuNPs are used for cell-targeted drug delivery e.g. for cancer treatment, although the mechanism of internalization of these particles in living cells is still under debate. We used the resonant CARS response of lipids to obtain cellular images, and multi-photon induced luminescence (MIL) to localize the AuNPs in three dimensions. The two approaches could be implemented on the same experimental setup as they share the excitation source, yet derive contrast from fundamentally different physical processes. Our results show that particles were internalized into the cells over a 10 hours incubation window. We found that healthy and tumor cells differentially respond to exposure to PEG-coated AuNPs. Limited internalization of the particles was found in tumor cells, with little increase over time. Isolated AuNPs were found localized primarily at the cell membrane or in endosomes in the perinucleic region of the cells. In contrast, healthy keratinocytes presented a large uptake of the particles with a dramatic increase of the number of internalized particles with time. These results, which were independently confirmed with Transmission Electron

Microscopy, indicate that the uptake mechanism of AuNPs is highly dependent on the cell line used, and possibly on the composition of the incubation medium.

The final two studies presented in this thesis focus on the identification of functional components in tissues based on the differences in their vibrational signature. In **chapter 6** we report on the visualization of cellular compartments in the developing wing disc of Drosophila melanogaster. The compartments that play a role in tissues development had previously been identified by fluorescent staining, but little information was available on the chemical differences between the compartments. In our experiments we were able to visualize the cell compartments by determining the differences in the local chemical composition in a label-free manner. We employed hyperspectral CARS imaging to measure a vibrational spectrum at each position in the disc. This dataset was first used to provide morphology maps of the entire disc in three dimensions based on the distribution of CH bonds. In order to deconvolute the differences in the vibrational spectra, Principal Component Analysis (PCA) of the hyperspectral CARS was employed. This analysis uses co-variance matrices to determine the spectral features with largest spatial variance and reduce the dimensionality of the dataset. We found that the maps obtained for the first and second principal components could distinguish the anterior/posterior and the hinge/notum compartmentalizations in the wing disc, respectively. The analytic form of the second component also showed that the hinge and the notum compartments differ in their chemical composition due to the predominant presence of lipids and proteins respectively, as indicated by the dispersive lineshape of the component in the CH stretching region. These results show that hyperspectral CARS imaging provides valuable chemical information to complement fluorescence in the determination of cell compartments, and serves as a basis for investigating the origin of these changes during development.

In **chapter 7** we present a study where we use hyperspectral CARS imaging to visualize lipid droplets and other biological components in thin sections of muscle tissues, and simultaneously investigate their chemical composition. The protein PLIN5, known to increase the production of intra-myocellular lipids, was selectively overexpressed in the investigated tissues. First, CARS maps were obtained, showing the local concentration of CH rich molecules in the tissue. Hierarchical Cluster Analysis (HCA), an alternative multivariate analysis to PCA, allowed identification of the spectral features bearing larger correlation at different locations in the tissue. The maps obtained by HCA provide clear identification of the lipid droplets present in the cells overexpressing PLIN5 as confirmed by fluorescence measurements of anti-PLIN5 staining. These lipid droplets were matched with lipid rich regions in a map of the spectral region from -2845 to -2905 cm^{-1}. We could also distinguish the protein-rich regions of the samples, corresponding to the vibrations between -2913 and -2970 cm^{-1}. Finally, features were found in the HCA maps compatible with the morphology of nuclei and mitochondria in muscle cells. These results demonstrate the utility of CARS for the research of complex tissue.

Samenvatting

In dit proefschrift presenteren we een reeks onderzoeken waarbij niet-lineaire vibrationele microscopie, in de vorm van Coherent anti-Stokes Raman Scattering (CARS) spectro-microscopie wordt gebruikt. De onderliggende motivatie van dit proefschrift was om de grenzen te verkennen en de technische haalbaarheid aan te tonen van beeldvorming met CARS in een verscheidenheid van biologische systemen. We beginnen met voorbeelden met behulp van CARS in conventionele morfologische microscopie en eindigen met multivariabele spectrale analyse, waarbij we aantonen dat in vibrationele beeldvorming informatie aan het licht komt die onbereikbaar is met andere technieken.

Microscopie is wellicht de meest onmisbare techniek binnen de biologische wetenschappen, omdat het inzicht geeft in de lokale organisatie van biologische systemen, evenals in de onderliggende biochemische interacties. Ook kan microscopie gebruikt worden om de interactie van biologisch materiaal met anorganische deeltjes te onderzoeken, een veelvoorkomende praktijk in medische behandelingen zoals labelen en als doelwitspecifieke shuttles voor medicijnen. De meest voorkomende beeldvormingstechniek met moleculaire specificiteit is fluorescentiemicroscopie, die in tegenstelling tot CARS gebaseerd is op elektronische in plaats van vibrationele excitatie om het contrast te leveren. Vanwege de noodzaak van elektronische transities vereist fluorescentie vaak de toevoeging van exogene moleculen aan de bestudeerde macromoleculaire systemen. CARS gebruikt echter inherente trillingen van moleculen als contrastmiddel om naar de lokale chemische samenstelling van een biologisch systeem te kijken. Omdat trillingen intrinsiek zijn aan alle moleculen zijn exogene labels niet vereist voor CARS metingen. Dit inherente contrast is het grote verschil met fluorescentiemicroscopie, en het belangrijkste voordeel van microscopie gebaseerd op CARS.

In CARS-experimenten is er interactie van drie fotonen met het bestudeerde systeem, met de emissie van een vierde foton - het anti-Stokes foton ten gevolg. Het CARS signaal wordt resonant versterkt wanneer de frequentie van een moleculaire vibratie gelijk is aan het frequentieverschil van twee binnenkomende fotonen. Vanwege de niet-lineariteit van dit proces is de respons van het systeem alln afkomstig uit het kleine focusgebied ($\sim 1\ \mu m^3$) in het medium, waar de kans op een vier foton-event hoger is. Dit verschaft de techniek intrinsieke sub-diffractieve resolutie en de mogelijkheid tot axiale secties. Hogere resolutie en grotere respons vanwege de resonante interactie zijn de belangrijkste voordelen van CARS spectro-microscopie in vergelijking met traditionele vibrationele technieken zoals infrarood of spontane Raman microscopie.

CARS microscopie wordt vaak toegepast in de single line uitvoering (CARS

van een enkele frequentie), om zo een beeld te krijgen van de ruimtelijke verdeling van een individuele verbinding, of beter gezegd van een individuele chemische groep in het systeem. De andere uitvoering is multiplex CARS, waar een vibrationeel spectrum op elke locatie in het monster wordt verkregen (hyperspectrale CARS beeldvorming). Hyperspectrale beeldvorming levert rijkere informatie op, omdat het de volledige vibrationele vingerafdruk van het monster bevat, maar kost ook aanzienlijk meer meettijd. Beide experimentele benaderingen zijn gebruikt in dit proefschrift en worden beschreven in **hoofdstuk 3**.

Het werk beschreven in dit proefschrift heeft betrekking op een aantal geselecteerde biomedische onderwerpen, waarbij de succesvolle toepassing van CARS spectro-microscopie naar voren komt. **Hoofdstukken 4** en **5** gaan in detail in op de studie van opname van anorganische deeltjes in levende cellen, wat relevant is in de medische therapeutica en diagnostica. In **hoofdstuk 4** behandelen we de visualisatie van Magnetic Resonance Imaging (MRI)-contrastmiddelen in levende cellen. Micrometer-grote ijzeroxidedeeltjes (MPIOs) worden gebruikt als labels voor cellulaire waarnemingen met MRI na celtransplantatie. Onze single line CARS experimenten, met een combinatie van resonante en niet-resonante CARS reacties, liet ons toe om de lokalisatie van MPIOs in levende hepatoma-cellen te bepalen. We konden de morfologie van individuele cellen visualiseren door de resonante respons van de CH-strek bindingen te detecteren. Vervolgens konden we de door de cellen opgenomen MPIOs lokaliseren met een tweede CARS meting, afgestemd op een niet-resonante golflengte, dat wil zeggen een spectraal gebied waar biologische moleculen geen vibraties kennen. MPIOs, die een grotere dichtheid van elektronen hebben ten opzichte van biologische materie, waren duidelijk zichtbaar in beide metingen, terwijl de cellen enkel zichtbaar waren in de resonante meting. Combinatie van de twee metingen leverde de exacte lokalisatie op van individuele MPIOs in de cellen, hetgeen de lokalisatie door middel van MRI (op mesoscopische schaal) goed aanvult. Gebruik makend de intrinsieke axiale resolutie van de techniek kan de positie van de deeltjes in de cellen worden bepaald in drie dimensies. Dit is een bijzonder nuttig resultaat, aangezien met standaard (brightfield) microscopie, de techniek die normaliter gebruikt wordt om het internalisatieproces te visualiseren, de genternaliseerde deeltjes niet langs de axiale richting van de deeltjes buiten het celmembraan te veronderscheiden zijn. Onze resultaten suggereren de mogelijkheid dat MPIOs ook tot in celkernen doordringen.

In **hoofdstuk 5** worden de resultaten over de opname van gouden nanodeeltjes (AuNPs) door gezonde cellen en tumorcellen beschreven. AuNPs worden gebruikt voor celgerichte toediening van medicijnen voor bijvoorbeeld de behandeling van kanker, hoewel het mechanisme van internalisatie van deze deeltjes in levende cellen nog ter discussie staat. We gebruikten de resonante CARS respons van lipiden om cellulaire opnamen te verkrijgen, en multi-foton genduceerde luminescentie (MIL) om de AuNPs in drie dimensies te lokaliseren. De twee benaderingen kunnen worden uitgevoerd met dezelfde experimentele opstelling omdat ze gebruik maken van dezelfde excitatiebron, maar ze ontlenen hun contrast van fundamenteel verschillende fysische processen. Onze resultaten

tonen aan dat deeltjes gedurende 10 uur worden genternaliseerd in de cellen. We vonden dat gezonde cellen en tumorcellen verschillend reageren op blootstelling aan PEG gecoate AuNPs. Beperkte internalisatie van de deeltjes werd gevonden in tumorcellen, met weinig toename gedurende de tijdsduur van de meting. Gesoleerde AuNPs werden voornamelijk gevonden op het celmembraan of in endosomen in het perinucleische gebied van de cellen. Gezonde keratinocyten echter lieten een grote opname van de deeltjes zien met een dramatische stijging van het aantal genternaliseerde deeltjes als functie van tijd. Uit deze resultaten, die onafhankelijk werden bevestigd met Transmission Electron Microscopy, blijkt dat het opnamemechanisme van AuNPs sterk afhankelijk is van de gebruikte cellijn, en eventueel van de samenstelling van het incubatiemedium.

De laatste twee studies gepresenteerd in dit proefschrift richten zich op de identificatie van functionele componenten in weefsels op basis van de verschillen in hun vibrationele spectrum. In **hoofdstuk 6** brengen we verslag uit van de visualisatie van cellulaire compartimenten in de ontwikkeling van de vleugelschijf van Drosophila melanogaster. De compartimenten die een rol spelen in de ontwikkeling van weefsels zijn eerder gedentificeerd door fluorescent labelen, maar weinig informatie was beschikbaar over de chemische verschillen tussen deze compartimenten. In onze experimenten konden we de celcompartimenten visualiseren door de verschillen in de lokale chemische samenstelling op een labelvrije manier te bepalen. We gebruikten hyperspectrale CARS beeldvorming om een vibrationeel spectrum te meten op elke positie van de schijf. Deze dataset werd eerst gebruikt om morfologische kaarten van de schijf te vormen in drie dimensies op basis van de verdeling van CH bindingen. Ter deconvolutie van de verschillen in de vibratiespectra werd Principal Component Analysis (PCA) van de hyperspectrale CARS toegepast. Deze analyse gebruikt covariantie-matrices om de spectrale kenmerken met de grootste ruimtelijke variatie bepalen en de dimensionaliteit van de dataset te verminderen. We vonden dat de data verkregen voor de eerste en tweede hoofdcomponenten respectievelijk voorkant/achterkant en het scharnier/notum compartiment in de vleugelschrijf konden onderscheiden. De analytische vorm van de tweede component liet ook zien dat de scharnier- en notum-compartimenten verschillen in hun chemische samenstelling door de overheersende aanwezigheid van respectievelijk lipiden en eiwitten, zoals blijkt uit het dispersieve spectrum van de component in de vibrationele CH regio. Deze resultaten tonen aan dat hyperspectrale CARS beeldvorming waardevolle chemische informatie biedt ter aanvulling van fluorescentie in het bepalen van celcompartimenten, en als basis dient voor het onderzoeken van de oorsprong van deze veranderingen tijdens de ontwikkeling.

In **hoofdstuk 7** presenteren we een studie waarin we gebruik maken van hyperspectrale CARS beeldvorming om lipidedruppels en andere biologische componenten te visualiseren in dunne secties van spierweefsel, en tegelijkertijd hun chemische samenstelling onderzoeken. Het eiwit PLIN5, waarvan we weten dat het de productie van intra-myocellulaire lipiden verhoogt, werd selectief tot overexpressie gebracht in de onderzochte weefsels. Eerst werden CARS overzichten verkregen, die de lokale concentratie van CH-rijke moleculen in het weefsel weergaven. Hirarchische Clusteranalyse (HCA), als multivariabele anal-

yse een alternatief voor PCA, stelde ons in staat de spectrale kenmerken met grote correlatie op verschillende plaatsen in het weefsel te identificeren. De overzichten verkregen door HCA leveren een duidelijke identificatie op van de lipidedruppels in de cellen met overexpressie van PLIN5, hetgeen bevestigd wordt door fluorescentiemetingen met anti-PLIN5 kleuring. Deze lipidedruppels kwamen overeen met lipiderijke regios op een overzicht van het spectrale gebied van -2845 tot -2905 cm^{-1}. Ook konden we de eiwitrijke regios veronderscheiden, met vibraties tussen -2913 en -2970 cm^{-1}. Ten slotte werden in de HCA overzichten kenmerken gevonden die overeen kwamen met de morfologie van celkernen en mitochondria in spiercellen. Deze resultaten tonen het nut van CARS in het onderzoeken van complexe weefsels.

Dankwoord

What matters the most is not what awaits you at the finish line, it is what you feel while you are running...

It has been a long and exciting journey, and none of it would have been possible without the precious contribution of the people around me. I looked back after writing the last word of this thesis and realized the acknowledgements might have easily become the larger chapter in this book if I were to thank every person who had been with me along the way. Hence, this will be a short and regrettably incomplete list of those who shared with me the victories and failures of this experience.

I would like to start by saying thanks to my supervisor Herr Direktor Prof Dr Idontknowwhichothertitleimforgetting Mischa Bonn for guiding me through the jungle of my PhD, and keeping his door always open (after knocking that is) for all of my weird scientific and personal questions. I am aware I was not the easiest student to supervise, but you did an excellent job and the things I learnt from you go way beyond the scientific experience. Also, I would like to say thanks to Michiel for being my first CARS teacher and handing the baton on to me. These years would not have been the same without the brilliant CARS groupies. Thanks to you the long hours in the dark - sarcasm free - CARS lab were a whole different experience. Kat, we have been through so many things together that I can hardly think of you as just a colleague. It was a privilege to meet you and to work with you and I am superproud of having earned the padrino title. James, I really appreciate your patience in always helping me out and entertaining me with cricket in the lab, and I sincerely thank you for being there when I felt I had had too much. Thanks to Nils for your zen attitude, for teaching me the little I know about biology (and about painting a house) but especially for listening to my endless complains. Thanks as well to Alex and Megan. Guys, you were legen... waitforit... dary members of the team. Thanks to my student Maarten. I still wonder if I managed to teach you anything useful, but I definitely learnt a lot from supervising you. My special thanks go to Ruben for sharing the office with me and always giving me a nice hug first thing upon arriving at work, and Avi for his very special crash course on PhD life and, actually, just for being so Avi. My PhD would not have been the same without my informal supervisors Kramer and Enrique. K, thank you so much for our endless conversations about practically everything, the advices, the huge piles of articles you kept suggesting I should read and I never did, and your magic trick for disappearing. Enrique, you have been a great friend and a critical scientific advisor, but especially the best company when it came to drinking 'just one beer' and talking life philosophy. I really

enjoyed sharing my days with the BaBo people, Joep, Ronnie, Ellen, Johannes, Susumo, Gennady, Mimmo, Klaas, Lukasz, Cho, Soren, Yves, Stephan, Sietse, Steven, Maaike, Maria, Zhen, and Huib. Thanks to the Mass Spec group for our project together. Ron, Florian, and especially Gert. Most of the mess I made in these years would not have been half as much fun without the tech support people solving it for me. Thanks to the ICT people, Carl, Richard, and Wiebe, for dealing with my Mac madness. Priceless has been the help of Marc Jan and Hinco. Guys, I really cannot find the words to thank you for saving my whatsthewordinenglish all these times. You are beyond doubt the closest to MacGyver I will ever get to see. I would like to thank Bergin for being more than family to me during this PhD and for the light in his eyes when he tells stories, and some very special AMOLFers, Marina, Ymkje, Wing Kiu, Wiet, Jose, Georg, Lara, Ana, Marjon, Ivana, and Jochen. Finally I would like to thank the AMOLF design department, secretaries and administration for making my life a lot simpler in a number of occasions. Guys, needless to say it was a pleasure and a honor sharing this experience with you...

Part of this PhD was performed at Chalmers University in the Enejder group. It was a wonderful time, which I shared with fantastic people. Thanks to Annika who always treated me as a member of the family, to Christian and Fredrik who taught me a great deal of things and were always available to help, to Malin, Jan Olof, and Lena for the fruktstunder, and to Valeria for being a great officemate. Also, I would like to thank my new colleagues at the MPI in Mainz where I have been working in the last months, Francesco, Andrea, Kamila, Erik, Hans Jorg, Zoltan, Dimitri, Maria, Kalina, Bernard, Tobias, Joe and Victor. Special thanks to the new CARS folks, Sapun and Will for bringing fresh energies in the game, for tearing my setups apart, and for the group meetings not too early in the morning.

Many people outside the academic walls also played an important role in shaping my life in the last years. I would like to thank my Amsterdam salsa crew (Flora, Lello, Susanne, Moa, Eugen, Paulina, Lenny, Marteen, Mouw, and James) and all my other salsa friends scattered around the globe with whom I shared many adventures dancing the nights away. A big thanks to my salsa show team, the eStilo family, for the performances and the hard trainings, Ning, Moranni, Linda, Ron, Juni, Derrick, Tatiana, Emmelien, Dwight, Daphne, Sandra, and especially Sergio who has been my salsa guru from day one. Words are not enough for thanking Jurg for opening the Pandora's box of my mind, and Huib, Somesh and Luca for picking up the thread of the task. For the inspiring conversations and the beautiful moments lived together, I would like to thank Scion, Ramon, Davide B, Kim, Anne, Kit, Marijn, Fanny, Cecile, Eddie, Trilly, Bea, Simo and Martina. Each and every one of you has a special place in my heart.

None of this, and I seriously mean none of this would have been possible without five very special people. I thank Roxy for always looking after me and (mostly) keeping me out of trouble. Thanks to Gianni for our bromantic and philosophic meetings. Thanks to my rational mirror, mio fratello mancato Ciccio, for being by my side on the ad maiora route. Really really thanks to my

two brothers, il Papi Daniele e Laura, for the priceless triangular communication and the (sort of) unconditional support. I cannot use words to say that Amsterdam would not have been the same without you. But maybe I can use numbers...

Dirijo un agradecimiento especial a Sandra. Yat, sin tu inspiracion no existiria esta poesia...

Per concludere, desidero ringraziare i miei genitori e mia sorella Giusy. A voi che mi avete dato la possibilitá di arrivare fino a qui, che con pazienza mi avete accompagnato lungo il cammino e sul cui consiglio posso sempre contare, va tutta la mia gratitudine. Vi voglio tantissimo bene, e questo giorno é tutto per voi.

I would like to dedicate this thesis to Francesco and zia Nina, whom are still greatly missed.